Max-Planck-Institut für Quantenoptik

Magnetized Cylindrical Implosions Driven by Heavy Ion Beams

Andreas J. Kemp

Vollständiger Abdruck der von der Fakultät für Physik der Technischen Universität München zur Erlangung des akademischen Grades eines

Doktors der Naturwissenschaften

genehmigten Dissertation.

Vorsitzender: Univ.-Prof. Dr. P. Kienle

Prüfer der Dissertation:

1. apl.Prof. Dr. J. Meyer-ter-Vehn
2. Univ.-Prof. Dr. M. Kleber

Die Dissertation wurde am 02.04.2001 bei der Technischen Universität München eingereicht und durch die Fakultät für Physik am 21.05.2001 angenommen.

Contents

1 Introduction 1

2 Ignition Conditions (I) Power Balance 5
- 2.1 Energy Deposition by Alpha Particles 5
- 2.2 Thermal Power Balance in the Fuel Volume 9
- 2.3 Ignition Criteria for the MTF Mode 12
- 2.4 Alternative Ignition Curve Parameters 14
- 2.5 Reduction of the Drive Power 16

3 Ignition Conditions (II) Hydrodynamic Approach 19
- 3.1 Fuel-Tamper Initial Configuration 19
- 3.2 Ignition Scaling with Fuel Mass 22
- 3.3 Fuel Parameter Window for Ignition 26

4 Magnetized Implosions with Heavy Ion Beams 29
- 4.1 Set-Up for Implosion Experiments 29
- 4.2 Energy Loss Mechanisms in Quasi-Adiabatic Implosions 36
- 4.3 Self-Sustained Magnetized Implosions 39
- 4.4 Magnetic Boundary Layer and Energy Scaling 45
- 4.5 Hydrodynamic Stability of the Pusher 48

5 Magnetized Fusion Targets 51
- 5.1 Ignition Threshold 52
- 5.2 Ignition and Burn 57
- 5.3 Scaling Properties 59

6 Self-Similar Description of Imploding Hollow Shells 63
- 6.1 Self-Similar Solution of the Equations of Gas Dynamics 65
- 6.2 Analytical Calculation of the Shell Compression 72

A Description of the Magneto-Hydrodynamics Code DEIRA 81
- A.1 Basic Equations 82
- A.2 Boundary Conditions 87
- A.3 Kinetic Coefficients and Radiation Energy Transport 87

Bibliography 89

Chapter 1

Introduction

The development of heavy ion accelerators towards greater beam intensities [1–3] offers new possibilities for the physics of high energy density in matter. The present work deals with cylindrical implosions driven by heavy ion beams. The intention is to study the generation of high energy density in matter for fundamental research, e.g. equations of state and transport properties of dense plasmas, and to explore the potential for inertial confinement fusion. This work is related to future research at the Gesellschaft für Schwerionenforschung (GSI), Darmstadt.

When beams of energetic heavy ions ($E_i = 10 - 1000\,\mathrm{MeV/u}$) are focused on solid matter, they naturally deposit their energy in cylindrical volumes. Implosions of hollow shells, which help to enhance the final energy density by means of cylindrical convergence, have been studied sporadically for a long time [4–7]. The particular point of the present work is to add an axial magnetic field (see Fig. 1.1), strong enough to suppress heat losses in radial direction during implosion and central stagnation. Such magnetic fields are consistent with the cylindrical target geometry. They may compensate for the inherently lower compression in cylindrical implosions, as compared to the spherical ones [8].

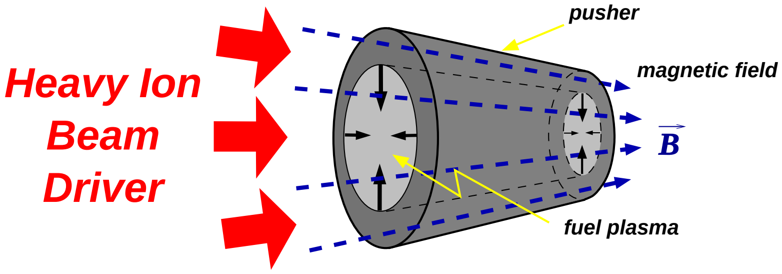

Figure 1.1 Schematic view of a magnetized cylindrical target. The target consists of a metallic tube filled with fuel plasma at low density. An axial magnetic field (B) is applied externally. The driving ion beam heats the outer part of the hollow cylinder; it expands radially and drives the inner part of the tube (pusher) towards the axis, as indicated by arrows. A typical size of the targets is approximately $1 - 3\,\mathrm{mm}$ in radius and $10 - 30\,\mathrm{mm}$ in length.

Magnetized Targets For Heavy Ion Fusion

Heavy ion beams are attractive drivers for inertial confinement fusion (ICF) because of the high efficiency, the repetition rate and the reliability of accelerators. So far, targets for heavy ion fusion (HIF), which is ICF with heavy ion beam drivers, have been studied almost exclusively in spherical geometry. In order to achieve spherically symmetric implosions, the fuel capsules are placed in so-called hohlraum cavities; as the cavities are heated by driver ion beams, thermal x-rays are generated which drive the pellet implosions. In this indirect-drive scenario [9], much energy is lost in the cavity. In contrast, the present work is devoted to cylindrical implosions, which can be driven directly by a single ion beam incident with high symmetry relative to the target axis. Another significant advantage of the cylindrical target geometry is that axial magnetic fields can be applied in order to reduce heat losses. This is the scheme of magnetized target fusion (MTF) driven by heavy ion beams. The present thesis is the first systematic study of this approach. Similar fusion schemes have been investigated earlier, but they use high explosives [4] or lasers [5] to drive the implosions.

The purpose of such implosions is the same in spherical and cylindrical geometry, namely to concentrate energy in a small amount of fuel in order to reach thermonuclear fusion conditions. The ignition threshold of non-magnetized fuel can be given as a criterion on fuel temperature T_0 and density-radius product ρR. For deuterium-tritium (DT) fuel, one needs $T_0 \gtrsim 5-10\,\mathrm{keV}$ and $\rho R \gtrsim 0.2-0.3\,\mathrm{g/cm^2}$ for ignition [9]. In the presence of a magnetic field, however, the ignition condition on ρR relaxes substantially due to the heat insulation. When the magnetic field is strong enough to confine also the trajectories of alpha particles from nuclear reactions (then alpha particles can escape only along the field lines), the ignition criterion on the ρR product is strongly reduced [8], see Chapter 2. This relaxation of the ignition threshold is a distinct property of magnetized ICF. It allows to significantly reduce the driver power required for MTF [8], while pulse energies remain comparable to those required for non-magnetized ICF [10], see Chapter 5.

Due to the lower fuel densities at peak compression, the characteristic fuel burn times in cylindrical targets are much longer than those in the spherical ones. Therefore, mass confinement is necessary for ignition and relies on heavy tampers. It is found in the present work that the ignition condition for the fuel ρR in magnetized cylindrical targets depends strongly on the tamper, in particular on its material properties at the time of stagnation [11], see Chapter 3. Energy, on the other hand, is confined by the magnetic field. For that reason, magnetized target fusion (MTF) is an intermediate approach to nuclear fusion between inertial confinement and magnetic confinement [12].

Hot-Spot Ignition

Hot-spot ignition is a method to achieve high energy gain in ICF targets by igniting the fuel from a small spark, similar to the use of a match. Sustained burn then relies on the propagation of a burn wave into a fuel reservoir. In cylindrical configurations, the burn wave has to propagate along the target axis. Results of corresponding 2D simulations have been published by Avrorin *et al.* [13] and are reproduced in Fig. 1.2. The present work, on the other hand, is based on 1D simulations, which cannot treat the axial burn wave; but they are sufficient to describe the dynamics of hot-spot formation. The present work is therefore restricted to a study of ignition conditions, where the hot spot is viewed

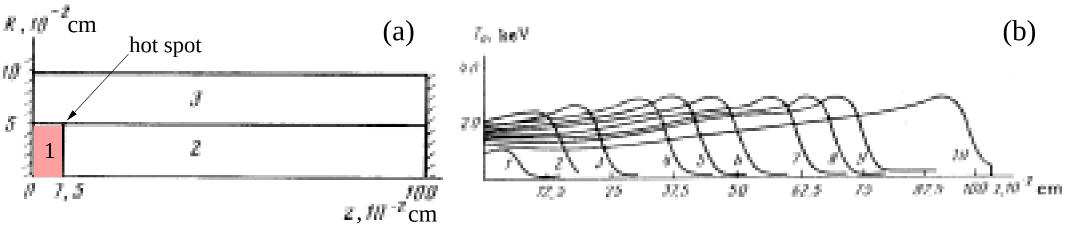

Figure 1.2 Numerical results for hot-spot ignition in cylindrical geometry, taken from Ref. [13]. (a) Initial configuration for a detonation wave running along a DT fuel column. Region (1) is the hot spot at $\rho_0 = 10$, $T_0 = 10$, where the fuel ignites. Regions (2) with $\rho_0 = 10$, $T_0 = 0$, and (3) with $\rho_0 = 30$, $T_0 = 0$ correspond to the cold fuel into which the wave propagates (units are g/cm^3 for density ρ and keV for temperature T). (b) Temperature profiles on the cylinder axis for times $t = 0.051 \ldots 3.06\,ns$.

as an axially uniform sector of an extended cylindrical configuration.

The cylindrical implosions considered in this work are relatively slow and it is a major problem to reach ignition temperatures, due to the absence of strong shock heating. Therefore, it is necessary to start from high initial fuel temperatures (50 eV or more) which could be brought into the fuel from outside the target, e.g. by an axially incident laser pulse. This is essentially the scheme of injected entropy, as suggested recently by Caruso *et al.* [14].

Magnetized Implosion Experiments

Intense beams of heavy ions, planned for the near future at heavy ion accelerator laboratories like GSI, Darmstadt [1], may achieve magnetized implosion experiments at pulse energies below 100 kJ and specific heating powers of 1 TW/g. Magnetization effects would manifest themselves in enhanced peak temperatures and corresponding neutron yields from D_2 fusion reactions. To prevent the rapid diffusion of magnetic flux during the implosions, it is necessary to provide certain minimum values of initial fuel temperature and of the product $(UR)_0$ of implosion velocity and initial fuel radius [15]. Still, a major problem of magnetized implosions is the accumulation of fuel material in a 'boundary layer' near the pusher. This mechanism is responsible for lower peak temperatures of magnetized implosions, as compared to idealized implosions with uniform profiles. The boundary layer formation depends mainly on the driver pulse energy: the relative amount of fuel mass in the boundary layer is found to decrease with increasing pulse energy, see Chapter 4.

Stagnation Pressure Scaling

The last chapter of the present work deviates from the main line in that it deals with a fundamental aspect of implosions on the basis of a highly idealized model. It analyzes the stagnation pressure of converging flows by means of a similarity solution [16] of the ideal gas-dynamic equations.

While this model is directly related to the topic of the present work because it helps to understand general features of cylindrical implosions, the particular interest in the similarity solution was triggered by recent work of Herrmann *et al.* [17] devoted to a scaling of the ignition energy E_{ign} of spherical ICF capsules. As pointed out by Atzeni *et al.* [18], the similarity model provides a simple interpretation of Herrmann's results; it yields a relation between the stagnation pressure of imploding hollow shells and external parameters, such as drive pressure and properties of the imploding shell material. The merits of the present work consist in deriving this formula for the first time analytically and in general form [19].

Computer Simulations

The numerical results presented in Chapters 3–5 have been obtained by means of the one-dimensional (1D) three-temperature Lagrangean magneto-hydrodynamics (MHD) code DEIRA [15]. The code solves a 1D system of single-fluid dissipative MHD equations in cylindrical geometry with a purely axial magnetic field, derived from the Braginskii equations [20]. Effects of the magnetic field on the transport coefficients – including electron and ion heat conductivities, electrical conductivity, ion viscosity and alpha particle diffusion – are accounted for. The physical model on which the code is based will be described briefly in Appendix A.

Chapter 2

Ignition Conditions (I) Power Balance

The principal objective of introducing a magnetic field into ICF targets is to reduce the ignition threshold value of the fuel ρR product at stagnation. First of all, this is required by the cylindrical geometry itself, due to inherently lower volume compression of cylindrical implosions. Secondly, by lowering the fuel ρR at ignition, one can reduce the driver power [8], which is a particularly sensitive issue for heavy ion drivers.

This chapter investigates ignition conditions in stagnating uniform deuterium-tritium (DT) cylinders by means of a thermal power balance. The hot DT volume is assumed to be tamped by a cold wall of either dense fuel or by external tamper material. Although the tamper properties do not appear explicitly in the analysis below, its presence is tacitly assumed to provide a sink for the energy carried away by the heat conduction out of the hot DT. The most important contribution to the power balance at stagnation is the heating by fast alpha particles from fusion reactions. An approximate formula for the fraction of alpha particle energy which is re-deposited in the fuel volume is given in Sec. 2.1.

The main conclusion is that a significant reduction of the ρR ignition is possible only if the alpha particles become at least marginally magnetized, so that their Larmor radius is smaller than the DT cylinder radius. This implies an ignition threshold of $BR \gtrsim 6 \times 10^5$ G cm for the product of magnetic field B and fuel radius R at stagnation.

2.1 Energy Deposition by Alpha Particles

The energy deposition fraction f_α measures the energy which is deposited in a cylindrical DT plasma volume by thermonuclear alpha particles. The alpha particles originate from the thermonuclear reaction $\mathrm{D} + \mathrm{T} \longrightarrow \mathrm{He}^4(3.52\,\mathrm{MeV}) + \mathrm{n}(14.07\,\mathrm{MeV})$. Their kinetic energy E_α corresponds to an initial velocity $v_0 = (2E_\alpha/m_\alpha)^{1/2} = 1.3 \times 10^9$ cm/s. For simplicity, the volume in which these reactions occur is assumed to be a uniform cylinder of radius R, with an embedded uniform magnetic field $\boldsymbol{B}$ directed along the cylinder axis. The quantity f_α, with $0 \le f_\alpha < 1$, can be represented as a function of two dimensionless parameters; they are chosen as

$$\bar{R} = R/l_\alpha \quad \text{and} \quad b = R/r_{\alpha L}\ , \tag{2.1}$$

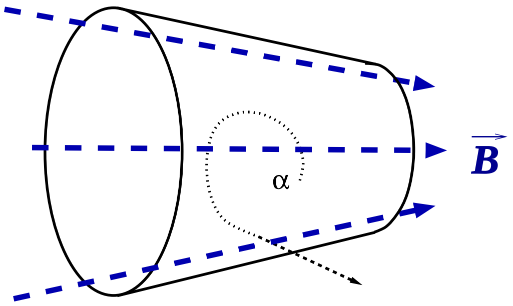

Figure 2.1 Schematic view of a magnetized, uniform fuel cylinder. The curved dotted line indicates the trajectory of an alpha particle after its birth in the fuel volume. The trajectory is bent by the magnetic field and may eventually leave the cylinder.

where l_α is the mean free path of the alpha particles given by Eq. (2.14) below. Their Larmor radius is $r_{\alpha\mathrm{L}} = v_0/\omega_\alpha$, where $\omega_\alpha = 2eB/m_\alpha c$ denotes the Larmor frequency of the alpha particles in the magnetic field B [20].

Following Basko *et al.* [8], the energy deposition fraction f_α can be calculated by integrating individual trajectories of alpha particles between the moment of their birth and the time when they leave the fuel volume: such a trajectory is depicted schematically in Fig. 2.1. Averaging over all possible birth positions and initial directions of the alpha particles yields numerical results for f_α as a function of cylinder radius R, fuel temperature T, and magnetic field B. This approach is equivalent to to solving the corresponding transport equation for the distribution function of alpha particles, as described for example in Ref. [21].

I. Asymptotical Behavior and Numerical Results

First of all, the special case of a non-magnetized plasma with $b = 0$ is considered. Here the absorbed energy fraction f_α is a function of one parameter $\bar{R} = R/l_\alpha$ only. While f_α can be calculated analytically for spherical fuel volumes [22], this is not possible in cylindrical geometry. Here only the asymptotical behavior in the limits of $\bar{R} \ll 1$ and $\bar{R} \gg 1$ can be established analytically [8] as

$$f_\alpha(\bar{R}, b = 0) = \begin{cases} \frac{8}{3}\bar{R} + O(\bar{R}^2), & \bar{R} \ll 1 \\ 1 - \frac{1}{6\bar{R}} + O\left(\frac{1}{\bar{R}^2}\right), & \bar{R} \gg 1\ . \end{cases} \tag{2.2}$$

Next, the qualitative dependence of f_α on the magnetic field B is examined in the limit $R \ll l_\alpha$, corresponding to $\bar{R} \ll 1$. In this case, all alpha particles born inside the DT cylinder can be roughly divided into two groups: those propagating nearly radially outwards, and those born in the narrow 'capture cone' with small pitch angles. The latter is defined as the angle between birth velocity of the alpha particle and the cylinder axis, i.e. $0 < \theta \lesssim \theta_c \ll 1$, or $0 < \pi - \theta \lesssim \theta_c \ll 1$. In the limit of a weak magnetic field, $r_{\alpha L} \gg R$, all the 'nearly radial' alphas escape the cylinder along almost straight trajectories, leaving only a small fraction $f_{\alpha s} \propto \bar{R}$ of their initial energy in the DT plasma. The alphas born within the capture cone deposit all their energy in the DT cylinder, so that their contribution to f_α is proportional to the solid angle occupied by the capture cone, i.e. proportional to θ_c^2. The width of the capture cone can be readily evaluated as

$$\theta_c \sim \begin{cases} \dfrac{R}{l_\alpha}, & R \ll l_\alpha \ll r_{\alpha L} \\ \dfrac{R}{r_{\alpha L}}, & R \ll r_{\alpha L} \ll l_\alpha \ . \end{cases} \tag{2.3}$$

Therefore, the asymptotical behavior for the total absorbed energy fraction in the limit of a weak magnetic field is given by

$$f_\alpha(\bar{R}, b) \sim \begin{cases} \dfrac{8}{3}\bar{R} + O(\bar{R}^2), & R \ll l_\alpha \ll r_{\alpha L}\,(b \ll \bar{R} \ll 1) \\ \dfrac{8}{3}\bar{R} + O(b^2), & R \ll r_{\alpha L} \ll l_\alpha\,(\bar{R} \ll b \ll 1) \\ 1 - O\left(\dfrac{1}{b}\right), & r_{\alpha L} \ll R \ll l_\alpha\,(\bar{R} \ll 1 \ll b)\ . \end{cases} \tag{2.4}$$

In the limit of a very strong magnetic field, $r_{\alpha L} \ll R$, only a small fraction of alphas born in a narrow surface layer of width $r_{\alpha L}$ escape the DT cylinder.

Figure 2.2 shows the dependence of $f_\alpha(\bar{R}, b)$ on b for three different values of $\bar{R}$, calculated numerically [8]. These results are in good agreement with the asymptotical formulae of Eq. (2.4). In particular, it is clearly seen that the transition from the 'optically thin' limit of $f_\alpha \approx 8\bar{R}/3 \ll 1$ in the non-magnetized case to a full absorption with $f_\alpha \approx 1$ in the limit of strong magnetization, where $b \gg 1$, does indeed proceed along the intermediate asymptote

$$f_\alpha \simeq 0.08\, b^2\ . \tag{2.5}$$

For practical applications, it is important to be aware of this intermediate asymptotical regime.

II. Approximate Formula

In order to have a simple expression for the alpha energy deposition fraction f_α, the Padé approximant

$$f_\alpha(x_\alpha) = \frac{x_\alpha + x_\alpha^2}{1 + 13x_\alpha/9 + x_\alpha^2} \tag{2.6a}$$

$$x_\alpha(\bar{R}, b) = \frac{8}{3}\left(\bar{R} + \frac{b^2}{\sqrt{9b^2 + 1000}}\right)\ , \tag{2.6b}$$

is used, where $\bar{R} \simeq 65.4\,\rho R T_{\mathrm{keV}}^{-3/2}$, and $b \simeq 3.7 \times 10^{-6}\, BR$ (assuming cgs-units). This expression has the following properties

- For the case of a non-magnetized plasma, when $b = 0$, the Padé formula conforms to both asymptotic limits in Eq. (2.2), and never deviates from the numerical results by more than 3.5 %; the maximum deviation of $1 - f_\alpha$ amounts to 10 %.

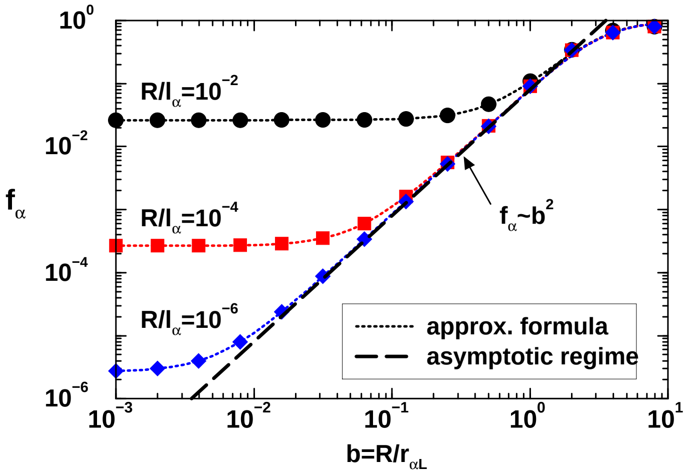

Figure 2.2 Energy fraction f_α deposited by the thermonuclear alpha particles in a uniform magnetized DT cylinder of radius R, plotted versus the fuel magnetization $b \propto BR$. Symbols correspond to numerical results [8] at three different values of the parameter $\bar{R}$, given in the figure. Dotted lines refer to the approximate formula (2.6) at corresponding values of b and R, for definitions see Eq. (2.1). The dashed straight line refers to the asymptotic behavior described in Eq. (2.5).

- The dependence on b in Eq. (2.6b) is chosen such as to describe both limits of $b \ll 1$ and $b \gg 1$ as given by Eq. (2.4), and to fit the numerical results shown in Fig. 2.2. It has two numerical constants under the square root. The free term 1000 fits the numerical results along the intermediate asymptote (2.5), while the coefficient 9 by b^2 is chosen on the basis of the diffusion approximation [8].

- The error of formula (2.6) is below 3 % whenever $f_\alpha < 0.05$, but may become as large as 50 % for the values of $f_\alpha = 0.1 - 0.5$. It is not attempted to improve the accuracy of Eq. (2.6) in the latter region, which corresponds to $R \simeq r_{\alpha L}$, because this would make little sense from the practical point of view due to the re-entry problem of the gyrating alpha particles.

- The results of the Padé expression (2.6) differ strongly from those obtained by simply reducing the alpha diffusion coefficient of non-magnetized plasmas [20] by a factor $[1 + (\omega_\alpha/\nu_\alpha)^2]^{-1}$, as for example assumed by Jones *et al.* [23]. The present treatment goes beyond this simplified approach.

A similar problem as the one described in this section has been treated earlier [21] for the case of a uniform sphere embedded in a uniform magnetic field. This situation is, however, qualitatively different from the one considered here. Since each field line of the uniform magnetic field pierces the spherical surface of the DT volume, the deposited alpha energy fraction $f_\alpha \propto \bar{R}$ remains significantly below 1 for $\bar{R} \ll 1$ even in the limit of an infinitely strong magnetic field. In the case described here, the field lines run parallel to the surface of the DT volume. For this reason, $f_\alpha(\bar{R}, b)$ approaches unity in a sufficiently strong magnetic field for arbitrarily small $\bar{R} \ll 1$.

2.2 Thermal Power Balance in the Fuel Volume

The thermal power balance in magnetized fuel volumes at stagnation is governed by three physical processes: energy deposition by alpha particles –analyzed in the previous section– acts to heat the fuel material; thermal conduction from the hot fuel into the cold tamper material, as well as radiative losses, act to cool the fuel material. If conduction and radiative losses from the fuel are too large, ignition never occurs. Only if the energy deposition by the thermonuclear alpha particles exceeds the losses, the fuel can be burnt effectively.

A simple analytic model [24] can help to illustrate these requirements in a qualitative manner. The net specific heating rate of the fuel at stagnation can be written

$$c_0 \frac{dT}{dt} = q_{\text{tn}} - q_{\text{br}} - q_{\text{hc}} \ , \tag{2.7}$$

where $c_0 = 1.16 \times 10^{15}\,\text{erg}\,\text{g}^{-1}\text{keV}^{-1}$ is the heat capacity of equimolar DT,

$$q_{\text{tn}} = 8.18 \times 10^{40}\, \rho \, \langle \sigma v \rangle_{\text{DT}} \, f_\alpha \ (\text{erg}\,\text{g}^{-1}\ \text{sec}^{-1}) \tag{2.8}$$

is the rate of thermonuclear heating by alpha particles, where $\langle \sigma v \rangle_{\text{DT}}$ is the fusion reaction rate averaged over a Maxwellian distribution. An approximate formula for $\langle \sigma v \rangle_{\text{DT}}$ is given in Appendix A. Further,

$$q_{\text{br}} = 3.11 \times 10^{23}\, \rho \, T_{\text{keV}}^{1/2} \ (\text{erg}\,\text{g}^{-1}\ \text{sec}^{-1}) \tag{2.9}$$

is the rate of bremsstrahlung cooling, and

$$q_{\text{hc}} = \frac{2(\kappa_e + \kappa_i)kT}{\rho R^2} \tag{2.10}$$

is the heat conduction energy loss. Heat balance Eq. (2.7) is written for cylindrical fuel volumes surrounded by either a cold metallic tamper or a cold dense fuel shell at the time of maximum compression. At this time, the power of PdV work against the hot fuel is zero. A remarkable property of the heat balance equation is that the ignition condition $dT/dt > 0$ can be expressed by a relationship between the parameters ρR and T only. Therefore, a two-parameter family of targets with different masses and temperatures can be described by a single ignition curve in the ρR, T plane. The graphical representation of these ignition boundaries is called Lindl-Widner (LW) diagram [25].

A key issue of the present analysis is to investigate how the ignition boundary in the ρR, T plane for uniform DT cylinders at stagnation is influenced by the presence of a strong magnetic field. With one more parameter B to characterize the fuel state, one expects a single ignition boundary in the ρR, T plane to become a one-parameter family of ignition curves. The topology of the ignition domain depends on the specific choice of the parameter which is kept constant along each ignition curve. Figures 2.3–2.5 below illustrate three different choices of the 'ignition curve parameter', leading to three different topologies of the LW diagrams.

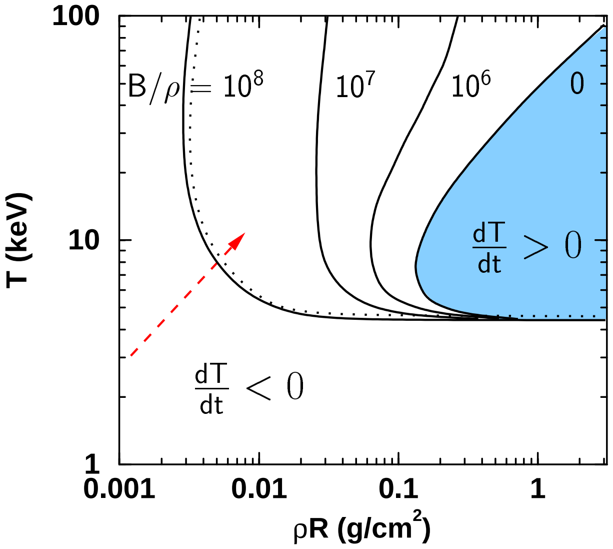

Figure 2.3 **Thermal balance of magnetized DT cylinders in the ρR, T plane. The solid curves are the ignition boundaries calculated from dT/dt = 0 in Eq. (2.7). They are shown for four fixed values of the parameter B/ρ, given near each curve in units of G cm^3/g. The corresponding ignition domain, where dT/dt $>$ 0, is indicated for B = 0. The dotted curve illustrates the effect of synchrotron radiation losses at fuel density $\rho = 1\,\mathrm{g/cm^3}$ and magnetic field B = 10^8 G. These values correspond roughly to the parameters of a magnetized ICF target at stagnation; note that implosion A in Chapter 5 operates at B/$\rho = 5 \times 10^7\,\mathrm{G\,cm^3/g}$, see Table 5.1. The dashed arrow indicates how the fuel state would advance towards the ignition boundary in the process of a quasi-adiabatic implosion.**

In Fig. 2.3, the ignition curve parameter is taken to be the ratio B/ρ. This is a natural choice in view of the functional form of the Braginskii formulas [20] for the electron and ion heat conduction coefficients in the presence of a magnetic field; these formulas depend on the ratio B/ρ and the temperature T. The parameter B/ρ is also most appropriate because it is a constant of motion for the interesting case of quasi-adiabatic implosions, cf. Chapter 4. Note that alternative ignition curve parameters can give physically interesting results as well. Two examples will be discussed in Sec. 2.4.

For a neutral plasma of hydrogen isotopes with particle density $n = n_e = n_i$ the Braginskii heat conduction coefficients assume the form

$$\kappa_e = \frac{nkT\tau_e}{m_e}\frac{11.92 + 4.664x_e^2}{3.770 + 14.8x_e^2 + x_e^4}, \quad x_e = \omega_{ce}\tau_e \ , \qquad (2.11)$$

$$\kappa_i = \frac{nkT\tau_i}{m_i}\frac{2.645 + 2x_i^2}{0.677 + 2.70x_i^2 + x_i^4}, \quad x_i = \omega_{ci}\tau_i \ , \qquad (2.12)$$

where $\omega_{ce} = eB/m_ec$, and $\omega_{ci} = eB/m_ic$ are, respectively, the electron and ion cyclotron frequencies in the magnetic field B, while

$$\tau_e = \frac{3\sqrt{m_e}(kT)^{3/2}}{4\sqrt{2\pi}e^4 n L_e} \ , \qquad \tau_i = \frac{3\sqrt{m_i}(kT)^{3/2}}{4\sqrt{\pi}e^4 n L_i} \tag{2.13}$$

are the electron and ion collision times [20]. For the corresponding Coulomb logarithms, fixed values $L_e = 7$ and $L_i = 9$ are used, roughly corresponding to a DT plasma with $\rho = 1\,\mathrm{g/cm^3}$ and $T = 10\,\mathrm{keV}$. Under the conditions of interest, the ion heat conduction is no less important than that by electrons; this is due to the fact that one has $\kappa_i \gg \kappa_e$ in the strongly magnetized case when $\omega_e\tau_e \gg 1$ and $\omega_i\tau_i \gg 1$.

The fraction f_α of the alpha particle energy deposited in the DT region is evaluated from Eq. (2.6). The required formula for the mean free path of alpha particles is

$$l_\alpha = \frac{3}{4\sqrt{2\pi}} \frac{m_\alpha v_0 (kT)^{3/2}}{Z_\alpha^2 e^4 n \sqrt{m_e} L_\alpha} = 0.107\, T_{\mathrm{keV}}^{3/2}/\rho L_\alpha \ \ (\mathrm{cm}) \ . \tag{2.14}$$

This expression accounts for the stopping by the free plasma electrons at temperatures $T > 1\,\mathrm{keV}$. The Coulomb logarithm L_α for the interaction of fast alpha particles with plasma electrons is fixed at $L_\alpha = 7$.

The physical meaning of the Lindl-Widner diagram shown in Fig. 2.3 is the following. For a target to ignite, the fuel parameters at stagnation must reach the domain $dT/dt > 0$. If the ignition domain is reached in the process of hydrodynamic implosion, the optimum ‘entry point’ corresponds approximately to the minimum of the triple product ρRT; this occurs at $T = 6$–$8\,\mathrm{keV}$, depending on the magnetic field. Note that, in this base version of the LW diagram for the magnetized fuel, no second ignition island at low ρR values appears, unlike suggested by Fig. 1 of Ref. [25]. Instead, the ‘standard’ ICF ignition region simply expands monotonically towards lower ρR as the parameter B/ρ is increased. Namely, one gets $(\rho R)_{\mathrm{ign}} \propto (B/\rho)^{-1}$ in the limit of a strong field. This scaling is explained in the next section. In the ideal case of a quasi-adiabatic implosion, the ratio B/ρ is conserved in the process of cylindrical implosions (cf. Chapter 4). Under this condition, the point representing the state of the imploding fuel in the ρR, T plane advances towards a stationary ignition boundary as indicated by the dashed arrow in Fig. 2.3.

In the LW diagrams of Figs 2.3 and 2.4 no account is taken of synchrotron radiation losses. It has been argued earlier [26] that they are not relevant for magnetized ICF targets. This is illustrated in Fig. 2.3 by a dotted curve: it is calculated for $\rho = 1\,\mathrm{g/cm^3}$ and $B = 10^8$ G, including the synchrotron loss term [26]

$$q_{\mathrm{sr}} = 1.50 \times 10^6\, T_{\mathrm{keV}} B^2 \left[1 + 4.9 \times 10^{-3}\, T_{\mathrm{keV}}\right] \ (\mathrm{erg\,g^{-1}\ sec^{-1}}) \tag{2.15}$$

in the heat balance Eq. (2.7). Note that the presence of q_{sr} in the heat balance equation violates the similarity law which reduces the solution of the equation $dT/dt = 0$ to a one-parameter family of curves in the ρR, T plane. This is due to the fact that, in contrast to the ratios q_{tn}/ρ, q_{br}/ρ, and q_{hc}/ρ, the ratio $q_{\mathrm{sr}}/\rho \propto TB^2/\rho$ cannot be expressed as a function of T, ρR, and B/ρ only.

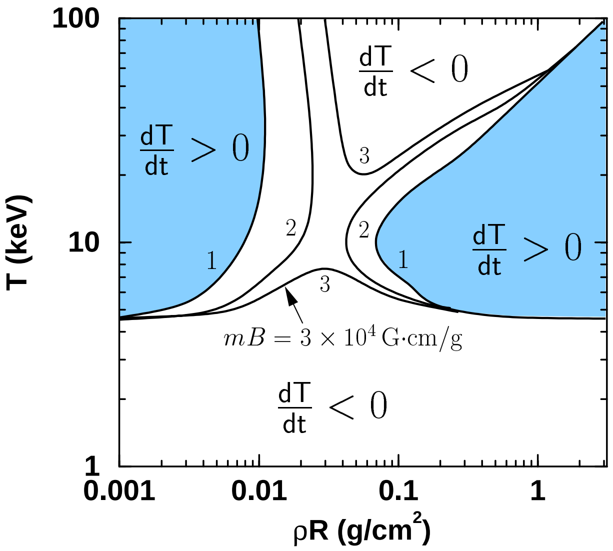

Figure 2.4 Alternative representation of the thermal balance of magnetized DT cylinders. Ignition boundaries in the ρR, T plane are calculated for three fixed values of the product mB $= \pi\rho$R^{2}B. Each curve is marked by the corresponding mB value in units of 10^4 G g/cm. The ignition domain for mB $=$ 10^4 G g/cm is shaded. Compare also Fig. 2.3.

2.3 Ignition Criteria for the MTF Mode

The well-known ICF ignition criterion for non-magnetized DT fuel is usually quoted as a lower bound on the fuel T and ρR values [9]. For DT cylinders, inferred from the $B = 0$ curve in Fig. 2.3, it reads

$$\begin{aligned} T &= 5\text{–}7\ \text{keV} \\ \rho R &\geq 0.2\ \text{g/cm}^2 \ . \end{aligned} \tag{2.16}$$

The MTF ignition mode aims at igniting the DT fuel at ρR values considerably lower than the ICF threshold of $0.2 - 0.3\,\text{g/cm}^2$. Hence, the constraint on the ρR product should be replaced by another condition. This condition is found by taking a closer look at the thermal balance of stagnating fuel.

First of all, a necessary condition for ignition is that the heating q_{tn} due to the deposition of thermonuclear alpha particles exceeds the bremsstrahlung losses q_{br}. Consider the ideal case of $f_\alpha = 1$ and no heat conduction losses, corresponding to a 'magnetically insulated' plasma. Here the balance between q_{br} and q_{tn} gives a minimum temperature of about 5 keV, independent of ρR. This limit can be seen in all LW diagrams, Figs 2.3-2.5. However, in the case of finite magnetic insulation, the power balance between q_{br} and q_{tn} implies

$$f_\alpha > 3.8 \times 10^{-18}\, \frac{T_{\text{keV}}^{1/2}}{\langle \sigma v \rangle_{\text{DT}}} \ , \tag{2.17}$$

according to Eqs (2.8) and (2.9). The function $T_{\mathrm{keV}}^{1/2}/\langle \sigma v \rangle_{\mathrm{DT}}$ has a minimum of $8.1 \times 10^{15}\,\mathrm{keV}^{1/2}\,\mathrm{sec}^{-3}$ at $T = 40\,\mathrm{keV}$. But the focus of this work lies on the temperature interval $T \approx 7$–$10\,\mathrm{keV}$, where the optimum 'entry' point into the ignition domain lies. Here, condition (2.17) yields

$$f_\alpha > 0.25\text{–}0.1 \; . \tag{2.18}$$

From Fig. 2.2 one can infer that for $R \ll l_\alpha$, inequality (2.18) implies a lower bound on the parameter

$$b \equiv \frac{R}{r_{\alpha L}} > 1.5\text{–}1.0 \; , \tag{2.19}$$

or, equivalently, a lower bound on the product BR. In other words, ignition in the MTF regime requires the thermonuclear alpha particles to be at least marginally magnetized, so that their Larmor radii $r_{\alpha L}$ be at least about equal to the hot fuel radius R.

Constraint (2.19) simplifies the evaluation of the role of heat conduction losses. For temperatures $T \gtrsim 6\,\mathrm{keV}$, inequality (2.19) implies that the magnetization parameter for the plasma ions [20]

$$\omega_{ci}\tau_i > \frac{0.015\ \mathrm{g/cm}^2}{\rho R} \tag{2.20}$$

exceeds unity for $\rho R \lesssim 0.01\,\mathrm{g/cm}^2$. As a consequence, the electron heat conduction can be neglected, because in the limit of strong magnetization the ratio of the two conductivities becomes

$$\lim_{x_i \to \infty} \frac{\kappa_e}{\kappa_i} = 2.33\,\frac{m_i \omega_i^2 \tau_i}{m_e \omega_e^2 \tau_e} = 2.33\sqrt{\frac{2m_e}{m_i}} \ll 1 \; ; \tag{2.21}$$

here the electrons and ions are assumed to have equal temperatures and Coulomb logarithms. Adding heat conduction cooling

$$q_{\mathrm{hc}} = \frac{2\kappa_i T}{\rho R^2} = 1.145 \times 10^{24}\,\frac{\rho T_{\mathrm{keV}}^{1/2}}{b^2}\ (\mathrm{erg\,g}^{-1}\,\mathrm{sec}^{-1}) \tag{2.22}$$

in the limit of $\omega_{ci}\tau_i \gg 1$, to the ignition condition $q_{\mathrm{tn}} > q_{\mathrm{br}} + q_{\mathrm{hc}}$, one obtains

$$f_\alpha > 3.8 \times 10^{-18}\,\frac{T_{\mathrm{keV}}^{1/2}}{\langle \sigma v \rangle_{\mathrm{DT}}}\left(1 + \frac{3.68}{b^2}\right) . \tag{2.23}$$

In the limit $R \ll l_\alpha$, where $f_\alpha(\bar{R}, b)$ becomes a function of only b in the relevant parameter range, the inequality (2.23) can be resolved to yield

$$b > 2.3\text{–}1.5 \tag{2.24}$$

for temperatures $T = 7$–$10\,\mathrm{keV}$. Finally, one arrives at the following ignition criteria for the magnetized cylindrical targets

$$\begin{aligned} T &= 7\text{–}10\ \mathrm{keV} \\ BR &\geq (6.5\text{–}4.5) \times 10^5\,\mathrm{G\,cm} \; . \end{aligned} \tag{2.25}$$

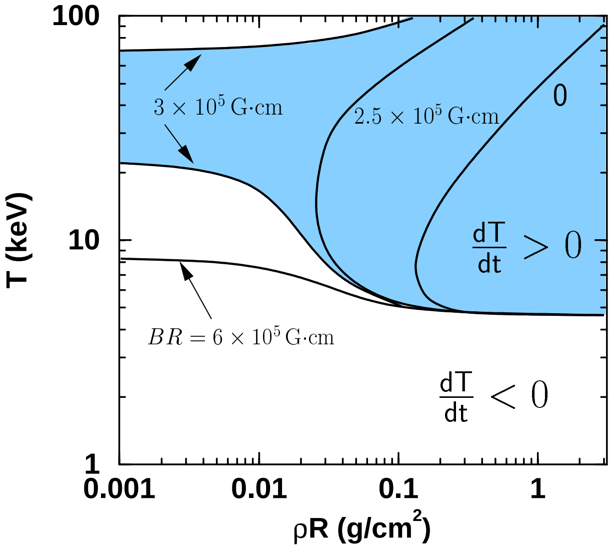

Figure 2.5 Another alternative representation of the thermal balance of magnetized DT cylinders. Along each ignition curve, the product BR is kept constant at a corresponding marked value. Compare also Figs 2.3 and 2.4.

They replace the ICF ignition criteria (2.16). Conditions (2.25) must be fulfilled in the magnetized DT fuel at the time of stagnation, if ignition is to occur at a ρR value significantly below the ICF threshold of 0.2–0.3 $\mathrm{g/cm^2}$. As one can infer from Fig. 2.2, the error introduced into the BR threshold by the inaccuracy of formula (2.6) for $f_\alpha \approx 0.1$–0.3 is below 20 %, which is comparable to the accuracy of the other assumptions made.

The lower bound on the BR product, as given by Eq. (2.25), is in perfect agreement with the numerical results for $B/\rho \gtrsim 10^8\,\mathrm{G\,cm^3/g}$ shown in Fig. 2.3. It explains also the scaling $(\rho R)_{\mathrm{ign}} \propto (B/\rho)^{-1}$ for the ignition threshold observed in Fig. 2.3. Note that inequality (2.23) implies that there is no regime with $q_{\mathrm{hc}} \gg q_{\mathrm{br}}$ for strongly magnetized targets, since bremsstrahlung is always at least comparable to, if not exceeding, heat conduction as cooling mechanism near the ignition threshold of magnetized targets.

2.4 Alternative Ignition Curve Parameters

Alternative ignition curve parameters can be obtained as arbitrary functions of the parameters B/ρ, ρR and T. For other parameters that cannot be expressed in this way, the LW diagrams fail to be universal in the sense that they become dependent of the fuel mass $m = \pi\rho R^2$ per unit length. Since the choice of an ignition curve parameter emphasizes different physical constraints or corresponds to different physical situations, it is revealing to consider $mB \propto (B/\rho)\,(\rho R)^2$ and $BR = (B/\rho)\,(\rho R)$ as two alternative parameters.

The first parameter examined here is the mB product. In the LW diagram shown in Fig. 2.4, each ignition boundary is calculated for a fixed value of mB. For small values of mB, there are two disconnected ignition regions with $dT/dt > 0$. One region is at large

ρR, corresponding to the ICF ignition mode at $\rho R \geq 0.1\,\mathrm{g/cm^2}$, another one is at small ρR. Note that the fuel burn in this regime is 'too slow' for the ICF ignition mode, see Chapter 3. For $mB \gtrsim 3 \times 10^4\,\mathrm{G\,g/cm}$, both regions merge and ignition becomes possible at any value of the fuel ρR, provided that a long enough confinement time is ensured. Such LW diagrams might be appropriate for situations when either the fuel mass m or the the magnetic field B are limited by external constraints. A typical situation is the case of magnetic fusion, where the maximum magnetic field is limited by technical constraints [12].

Now consider the product BR as ignition curve parameter. Figure 2.5 shows what the corresponding LW diagram looks like. Its topology is intermediate between the two cases of Figs 2.3 and 2.4. The ignition domain $dT/dt > 0$ is always single-connected, and for $BR < (BR)_* \approx 3 \times 10^5\,\mathrm{G\,cm}$, it looks similar to the ignition region in the first LW diagram (Fig. 2.3). If the BR parameter exceeds the threshold value $(BR)_*$, the $dT/dt > 0$ region extends to infinitely small ρR and ignition becomes possible at any ρR value (in the absence of other possible limiting effects such as inverse Compton scattering, or synchrotron radiation cooling). It is also seen that for a practically interesting case of ignition temperatures around 10 keV, the BR threshold is close to $6 \times 10^5\,\mathrm{G\,cm}$.

Figure 2.6 demonstrates the origin of the different topologies in the LW diagrams Figs 2.3–2.5 by plotting the alpha energy deposition fraction f_α versus ρR for fixed fuel temperature $T = 10\,\mathrm{keV}$, and for a characteristic value of each ignition curve parameter. One can see that the function $f_\alpha(\rho R)$ grows over the full range of ρR only for B/ρ =const,

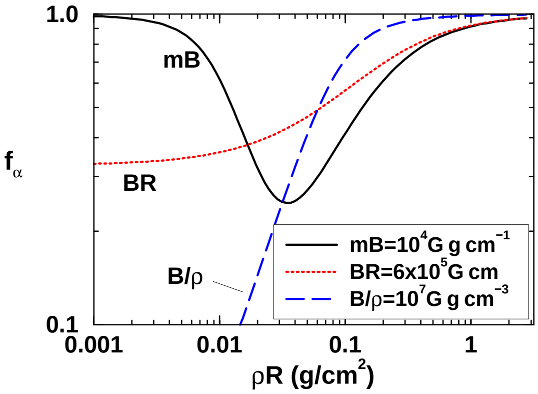

Figure 2.6 Energy deposition fraction f_α versus ρR, for three different ignition curve parameters. For these parameters, representative values of the corresponding LW diagrams are chosen. All curves are calculated for a temperature T = 10 keV. The ignition curve for B/ρ = const reflects the decreasing values of the alpha particle magnetization as ρR falls. The mB = const curve, on the other hand, reflects the two distinct regimes for significant alpha particle deposition in the fuel. These are (i) the regime of a magnetized plasma for low ρR values, and (ii) a regime at large ρR, where the plasma is 'optically thick' for the alpha particles. Note that for large values of mB the intermediate region, where $f_\alpha \ll 1$, becomes less pronounced. The third curve for BR = const refers to constant magnetization b of the alpha particles. Nevertheless, the deposition fraction f_α decreases with falling ρR, as the plasma becomes 'transparent' for alpha particles.

while it behaves differently for the BR and mB curves. Large deposition fractions f_α at small ρR, characteristic for the last two ignition curve parameters (as seen in Fig. 2.6), are reflected by the appearance of $dT/dt > 0$ regions in the corresponding LW diagrams (see Figs 2.4–2.5). The behavior of the function $f_\alpha(\rho R)$ for fixed mB or BR is connected with the two different energy deposition mechanisms for alpha particles in magnetized plasmas described by Eq. (2.6). These are (i) Coulomb collisions in the case of an 'optically thick' (with respect to alpha particles) plasma, i.e. $\bar{R} \leq 1$, and (ii) the magnetization of alpha particles in plasmas which are 'transparent' for alpha particles, i.e. $\bar{R} \ll 1 \ll b$. As Fig. 2.6 demonstrates, both effects can bring the deposition fraction of alpha particle energy f_α close to unity.

2.5 Reduction of the Drive Power

Previous authors [27, 28] have already emphasized that fuel magnetization could reduce the requirements on the peak drive power, which is a particularly sensitive issue for a heavy ion driver. This point will be illustrated by a scaling law derived in the framework of the following simple model.

Assume that a uniform cylindrical volume of DT plasma is imploded by a massive tamper of mass m_t per unit length. Setting the kinetic energy of the implosion equal to the internal energy of the fuel when the implosion comes to halt, one can write

$$E = \frac{1}{2} m_\mathrm{t} v_\mathrm{imp}^2 = \frac{3\pi}{2} p_\mathrm{m} R_\mathrm{m}^2 \ , \tag{2.26}$$

where v_imp is an average implosion velocity, and R_m and p_m are the fuel radius and pressure at maximum compression. Now the implosion time t_i, and the time of confinement t_c which is determined by the acceleration of the tamper by fuel pressure p_m, are related by

$$t_\mathrm{i} \simeq \frac{R_0}{v_\mathrm{imp}} = C_r \left(\frac{m_\mathrm{t}}{3\pi p_\mathrm{m}} \right)^{1/2} \simeq C_r t_\mathrm{c} \ . \tag{2.27}$$

Here, R_0 is the initial fuel radius, and $C_r = R_0/R_\mathrm{m}$ is the radial convergence ratio. The drive power W_dr per unit cylinder length is then given by

$$W_\mathrm{dr} \simeq \frac{E}{t_\mathrm{i}} = \frac{3\pi}{2} \frac{p_\mathrm{m} R_\mathrm{m}^2}{C_r t_\mathrm{c}} \ . \tag{2.28}$$

If the fusion energy yield is equal to the implosion energy i.e.

$$\frac{1}{4} n_e^2 \langle \sigma v \rangle_\mathrm{DT} E_\mathrm{DT} \, t_\mathrm{c} = 3 \, n_e \, T \ , \tag{2.29}$$

one can eliminate the confinement time t_c from Eq. (2.28). This gives the scaling

$$W_\mathrm{dr} \propto \frac{(\rho R)^2}{C_r} \langle \sigma v \rangle_\mathrm{DT} \ . \tag{2.30}$$

In Eq. (2.29), n_e is the electron density per unit length, and $E_\mathrm{DT} = 17.6\,\mathrm{MeV}$ is the DT reaction energy. The DT reaction rate $\langle \sigma v \rangle_\mathrm{DT}$ is a function of the temperature T only. It is always close to 10 keV near the ignition threshold, cf. Appendix A.

Equation (2.30) says that for a fixed ignition temperature T the drive power for cylindrical targets scales as the square of the fuel ρR needed to achieve ignition. Hence, by bringing down the ρR value at ignition, fuel magnetization allows to reduce the required driver power. Evidently, higher values of the radial convergence C_r would help to reduce W_{dr} as well. Note that the key assumptions behind scaling (2.30) are (i) the necessary confinement is provided by a massive tamper, and (ii) ignition occurs over the entire fuel volume, at 'breakeven', see Eq. (2.29).

Chapter 3

Ignition Conditions (II) Hydrodynamic Approach

The confinement of the fuel by means of heavy walls (tampers) at stagnation is a crucial point for magnetized cylindrical targets, as pointed out in the previous chapter. In the following, the influence of the tamper material on the performance of cylindrical implosions is investigated. The fuel plasma enclosed by the tamper is assumed to be magnetically insulated, which means that heat conduction losses as well as the diffusion of alpha particles are suppressed in radial direction. The main conclusion is that the minimum fuel ρR required for ignition depends sensitively on material properties (i.e. equation of state) of the tamper.

Below, the results of one-dimensional computer simulations of pre-assembled fuel–tamper configurations are presented. Numerical results have been calculated with the 1D hydrodynamics code DEIRA, described in Appendix A. Similar configurations, without magnetization, have been widely studied for spherical geometry [29]. Here, this matter is reconsidered for magnetically insulated cylindrical targets. Note that questions of symmetry and stability will not be considered in this chapter.

3.1 Fuel-Tamper Initial Configuration

Since ignition of ICF targets occurs approximately when the target implosion has come to a halt, one can, as a first step, investigate the basic properties of the ignition process by starting with pre-assembled fuel-tamper configurations at the time of stagnation. Such a configuration consists of hot deuterium-tritium (DT) fuel surrounded by a layer of dense tamper material to provide inertial confinement. It is assumed that the pressure is constant throughout the compressed core at the time of stagnation [30], and that the profiles of density and temperature are uniform in the fuel and the tamper layer. This simplifying assumption is consistent with one-dimensional simulations of cylindrical implosions.

I. Target Magnetization

The aim of this chapter is to explore the influence of a tamper on the ignition threshold of magnetized targets in the most favorable situation concerning the effect of the

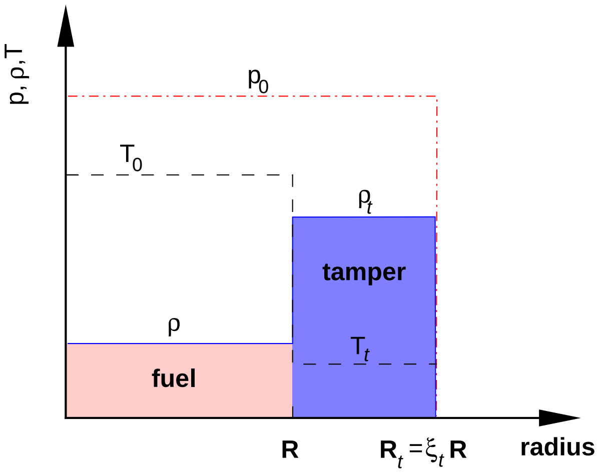

Figure 3.1 Radial profiles of pressure, density and temperature in the initial configuration, assuming a cylindrical geometry. The tamper thickness is characterized by the ratio ξ_t.

magnetic field. Therefore one can work in the limit of high magnetic fields, such that the electron and ion heat conduction as well as the diffusion of alpha particles along the radial direction are suppressed. This limit is adequate if the collision frequencies of the alpha particles and the electrons are small compared to the corresponding cyclotron frequencies. The energy relaxation time between the alpha particles and the electrons is not affected by the magnetic field [31, 32].

There is a wide range of fuel parameters where the effects of magnetic field pressure on the plasma dynamics can be neglected. In this situation, one can account for magnetic field effects simply in terms of modified coefficients for the heat conduction and the alpha particle diffusion, and perform purely hydrodynamic, rather than full MHD simulations. This simplification helps to bring out more clearly the important role of the tamper material.

II. Initial Configuration and Basic Parameters

Figure 3.1 shows a schematic picture of the initial configuration. It consists of a cylindrical volume of hot DT fuel, surrounded by a tamper shell of heavy metal at a high density ρ_t and a temperature T_t. The pressure p_0 is uniform throughout the fuel and the tamper. The tamper thickness is characterized by the ratio ξ_t of the outer tamper radius to the outer fuel boundary at stagnation. In order to account for different heating situations of the tamper during target implosion, the initial liner temperature T_t is varied in the range from 1 eV to 100 eV.

Throughout this chapter, the fuel is described in terms of its stagnation temperature T_0, the fuel confinement parameter ρR and the fuel mass per unit length $m = \pi \rho R^2$.

The initial fuel temperature has been chosen as $T_0 = 7\,\text{keV}$ above the DT ignition threshold value of $4 - 5\,\text{keV}$, set by the power balance between alpha particle heating and bremsstrahlung losses. Varying T_0 between 7 and $10\,\text{keV}$ does not change the final result significantly.

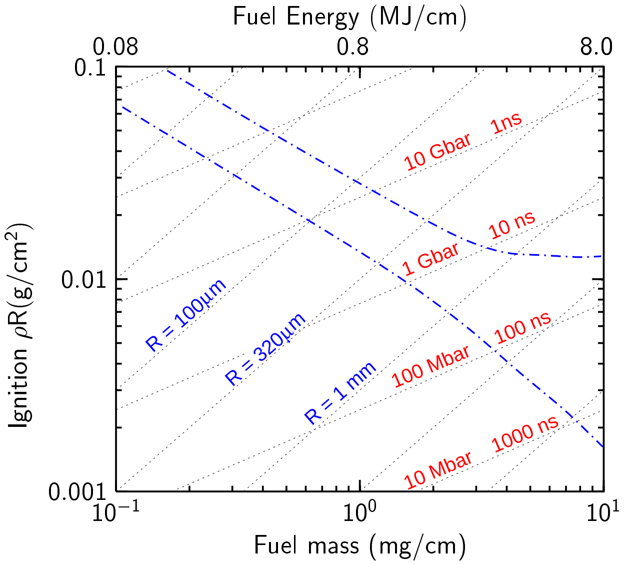

Figure 3.2 Initial pressure and fuel radius in terms of the principal fuel parameters. The dash-dotted lines refer to the two outer ignition curves of Fig. 3.6 below. The corresponding fuel energy at $T_0 = 7\,\mathrm{keV}$ is given on the upper axis. Additionally, the fusion time scale as defined in Eq. (3.1) is given. Note that the implosion time scale is typically by a factor 10 – 100 larger than the fusion time scale.

The choice of ρR and m as the basic parameters, instead of $\rho = \pi(\rho R)^2/m$ and $R = m/\pi\rho R$, is made for the following reasons. For inertially confined fuel, the amount of burnt fuel (the burn fraction) depends on two times, the fusion time

$$t_\mathrm{f} \propto 1/\rho\langle\sigma v\rangle_\mathrm{DT} \;, \tag{3.1}$$

where $\langle\sigma v\rangle_\mathrm{DT}$ is the rate coefficient of the DT fusion reactions, and the confinement time $t_\mathrm{c} \propto R/c_\mathrm{s}$, where c_s is the sound velocity of the confining mass. The burn fraction ϕ_b depends on the ratio of these times

$$t_\mathrm{c}/t_\mathrm{f} \propto \frac{\langle\sigma v\rangle_\mathrm{DT}}{c_\mathrm{s}}\rho R \;. \tag{3.2}$$

For bare fuel without any tamper, one has to take the sound velocity $c_\mathrm{s} \propto \sqrt{T_0}$ of the fuel itself, which depends only on the temperature T_0, just as $\langle\sigma v\rangle_\mathrm{DT}$ and is fixed by ignition physics. Therefore, the burn fraction depends only on ρR, and an approximate formula is $\phi_\mathrm{b} = \rho R/(H_\mathrm{B} + \rho R)$, where the burn parameter H_B depends on temperature; one finds $H_\mathrm{B} = 6.3\ \mathrm{g/cm^2}$ for $T_0 = 7\,\mathrm{keV}$ [33]. Concerning tamped cylindrical configurations, the essential difference is that the relevant sound velocity is that of the tamper, and corresponding burn fractions are discussed below. The fuel mass m, which is the other main parameter, determines the initial amount of thermal energy in the fuel $E = \epsilon_\mathrm{DT} m T_0$, with $\epsilon_\mathrm{DT} = 1.15 \times 10^8\,\mathrm{J\,g^{-1}\,keV}$.

In the following, results will be plotted as functions of ρR and m. For reference, Fig. 3.2 shows the relevant fusion times, see Eq. (3.1), pressures and fuel radii in the

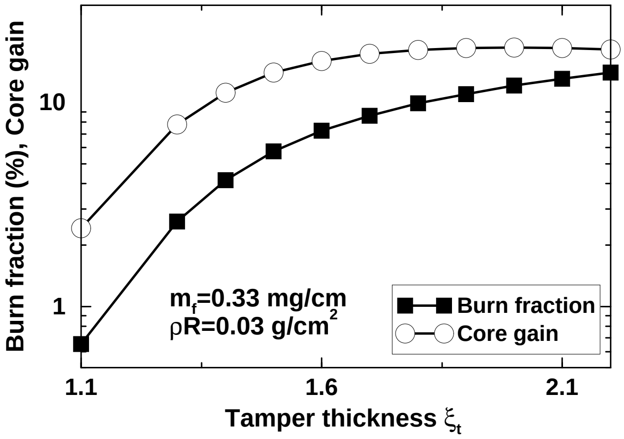

Figure 3.3 Fuel burn fraction and energy gain of magnetically insulated targets vs. tamper thickness ξ_t. In this and all the following figures in this section, each symbol represents the final result of a hydrodynamic simulation run.

ρR, m plane. The upper axis gives the initial energy of the compressed fuel. The dash-dotted lines in Fig. 3.2 refer to the outer ignition curves of Fig. 3.6. They will be discussed in Sec. 3.2 below.

3.2 Ignition Scaling with Fuel Mass

The simulations described below have been performed with the Lagrangean, one-dimensional hydrodynamics code DEIRA [34], described in Appendix A. In order to account for the magnetic insulation of the target in the sense discussed in Sec. 3.1, the diffusion coefficient for the fast alpha particles, see Eq. (A.18), and the coefficients for both ionic and electronic heat conduction, see Eq. (A.12)–(A.13), are set equal to zero in the code, while the finite 'heat capacity' of the alpha particles is retained.

I. Optimum Tamper Thickness

The dependence of burn fraction and energy gain on the tamper thickness ξ_t are shown in Fig. 3.3 for typical values of ρR and m. The energy gain is defined here as the ratio of the thermonuclear energy yield to the energy of the configuration at stagnation, including the tamper energy. For thin tampers, the energy gain increases rapidly with ξ_t; for large values of ξ_t, energy gain and burn fraction both saturate and the energy gain even falls slightly. The saturation of the energy gain for large tampers results from the high fraction of energy invested in the tamper. This energy fraction, given approximately by $(\xi_t^2 - 1)$, is the ratio of the tamper to the fuel volume at stagnation. Since the configuration is assumed to be isobaric initially, the ratios of energies and volumes of fuel and tamper are approximately equal.

As a working point near the optimum, $\xi_t = 1.7$ has been selected, corresponding to a tamper volume twice the fuel volume and a temperature of $T_t = 100$ eV. It will be shown

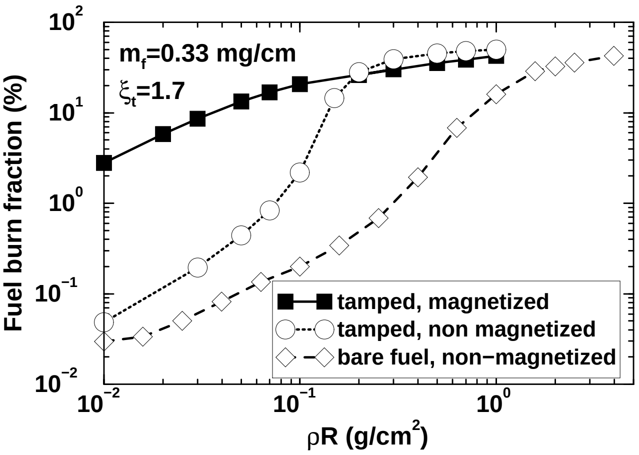

Figure 3.4 Fuel burn fraction vs. initial fuel ρR of targets with and without magnetic insulation. The empty circles represent results for the case of bare fuel without magnetic insulation.

later how the final results are affected by the choice of tamper thickness and temperature. In all simulation results presented here, gold has been used as tamper material, but any other heavy metal will give similar results.

II. Fuel Burn in Magnetically Insulated Targets

In Fig. 3.4, the burn fraction of fuel–tamper configurations with and without magnetic insulation is plotted as a function of fuel ρR. One observes a dramatic increase of the fuel burn fraction at low ρR for the magnetized case. Another distinct feature is the lack of a sharp ignition boundary. The burn fraction increases gradually with the fuel ρR, similar to the burn in magnetically confined fusion plasmas. The reason for this is the complete re-deposition of alpha particles in the fuel, even at low fuel ρR values.

In non-magnetized targets, however, there is an 'ignition cliff', a marked increase of the burn fraction when passing a certain ρR threshold as seen in Fig. 3.4. It results from the bootstrap heating by alpha particles when the fuel ρR exceeds the stopping range of approximately 0.3 g/cm^2. For smaller ρR and without magnetic field, most of the alpha particles leave the fuel.

Additionally, Fig. 3.4 shows the fuel burn fraction of bare fuel without tamper and magnetic insulation, corresponding to the situation discussed in Sec. 3.1. Without the additional confinement owing to the tamper, the ignition cliff moves to larger fuel ρR and becomes less sharp.

III. Ignition of Magnetically Insulated Targets

Figure 3.5 shows the peak fuel temperature reached in various target explosions as a function of the initial fuel ρR. While each point in the plot represents an individual history of a target evolution with given initial values of fuel mass m and ρR, the curves connect points with constant fuel mass. Targets are called 'ignited' if the peak fuel temperature during disintegration exceeds 21 keV, i.e. if the fuel temperature rises at least

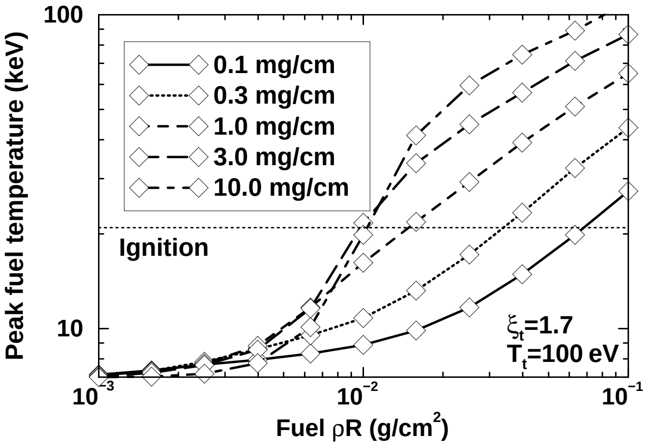

Figure 3.5 Peak fuel temperature during target disintegration vs. the initial fuel ρR, for targets with various fuel masses m. The ignition threshold at T = 21 keV, as defined in Sec. 3.2, is indicated by the dotted horizontal line.

to three times the initial value of $T_0 = 7\,\mathrm{keV}$. Such a definition is necessary here since there is no clear ignition 'cliff', as in the case of the non-magnetized targets; see Figs 3.4 and 3.5. The definition is consistent with the ignition threshold of non-magnetized targets. In Fig. 3.5 one observes that the ignition threshold moves systematically to lower fuel ρR values as the fuel mass increases.

The dependence of the ρR ignition threshold on the fuel mass is shown explicity in Fig. 3.6. Various curves are presented for different values of the tamper parameters in order to account for different implosion histories. The scalings of the ignition threshold ρR with the fuel mass $(\rho R)_{\mathrm{ign}} \propto m^{-\kappa}$ are indicated by dashed lines, where $\kappa \approx 0.65$ for small fuel mass (≤ 1 mg/cm) and approaches $\kappa \approx 1.0$ for larger m. It turns out that the position of the ignition threshold ρR for large fuel masses $m \geq 1.0$ mg/cm depends on the initial temperature T_{t} of the tamper material. For 'warm' tampers with $T_{\mathrm{t}} \approx 100$ eV, it remains above 0.01 g/cm^2. For cold tampers with $T_{\mathrm{t}} \ll 100$ eV however, it can drop significantly below this value. In this regime the fusion time scale, as given by Eq. (3.1) and shown in Fig. 3.2, is in the μs range. Also shown in Fig. 3.6 is the dependence on the tamper thickness ξ_{t}. The ignition ρR of targets with a thin ($\xi_{\mathrm{t}} = 1.4$) and those with a large ($\xi_{\mathrm{t}} = 1.7$) tamper differs by about a factor of two.

IV. Ignition Scaling with Fuel Mass

As will be shown in the following, the simulation results presented above can be understood in terms of equation of state (EOS) properties of the tamper. For the tamped configuration, the confinement time t_{c} is essentially the time of tamper disintegration. Therefore, the ignition scaling is found from Eq. (3.2) for a fixed ratio $t_{\mathrm{c}}/t_{\mathrm{f}}$ in the form

$$(\rho R)_{\mathrm{ign}} \propto c_{\mathrm{t}} \ , \tag{3.3}$$

where $c_{\mathrm{t}} \propto (dp/d\rho)_{\mathrm{t}}^{1/2}$ is now the sound velocity of the tamper, determined by its EOS. The pressure EOS for gold, which is the tamper material used in the simulations, is

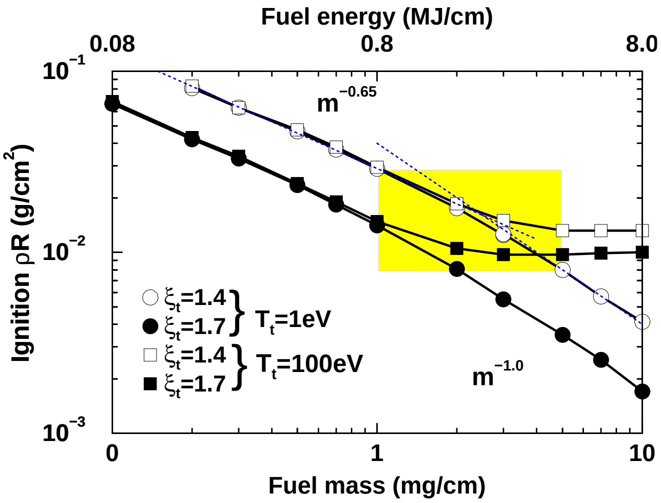

Figure 3.6 Ignition ρR vs. fuel mass for different choices of thickness $\xi_{\rm t}$ and initial temperature T$_{\rm t}$ of the tamper. The ignition scalings at low and high fuel masses are indicated by dotted lines, see Sec. 3.2 For the shaded area, see Sec. 3.3. The fuel energy corresponding to a fuel temperature of T$_0$ = 7 keV is given on the upper axis.

shown in Fig. 3.7 in the form of four isotherms. One can distinguish two regions: firstly, the 'degenerate' regime close to the $T = 0$ isotherm, where pressure can be approximated by $p \propto \rho_{\rm t}^{\gamma}$ with $2.3 \le \gamma \le 3.0$ in the relevant density and temperature regime; and secondly the thermal regime where $p \propto \rho_{\rm t} T_{\rm t}$.

In order to express $c_{\rm t}$ in terms of the fuel ρR and mass m, one can make use of the assumption that initially the pressure is equal in both fuel and tamper layer; one finds

$$\rho T_0 \propto p \equiv p_{\rm t} \propto \begin{cases} \rho_{\rm t}^{\gamma} & \text{(degenerate regime)} \\ \rho_{\rm t} T_{\rm t} & \text{(thermal regime)}\ . \end{cases} \tag{3.4}$$

for the initial configuration, where $p_{\rm t}, \rho_{\rm t}, T_{\rm t}$ refer to the tamper and p, ρ, T_0 to the fuel. For the degenerate regime, one obtains $c_{\rm t} \propto \rho_{\rm t}^{(\gamma-1)/2} \propto \rho^{(\gamma-1)/2\gamma}$, and from Eq. (3.3) together with $m \propto \rho\, R^2$

$$(\rho R)_{\rm ign} \propto m^{-\kappa}\ , \tag{3.5}$$

with $\kappa = (\gamma - 1)/2 = 0.65$ for $\gamma = 2.3$ and $\kappa = 1.0$ for $\gamma = 3.0$. Apparently, these values of κ explain the shapes of the ignition curves in Fig. 3.6 for cold tampers ($T_{\rm t} = 1$ eV). For higher temperatures ($T_{\rm t} = 100$ eV), the tamper is in the thermal regime with $c_{\rm t} \propto \sqrt{T_{\rm t}}$, and Eq. (3.3) therefore leads to

$$(\rho R)_{\rm ign} = \text{const}\ , \tag{3.6}$$

independent of fuel mass. This explains the lower bound of $(\rho R)_{\rm ign} \approx 0.01$ g/cm^2 seen in Fig.3.6 for $m \le 1$ mg/cm and $T_{\rm t} = 100$ eV.

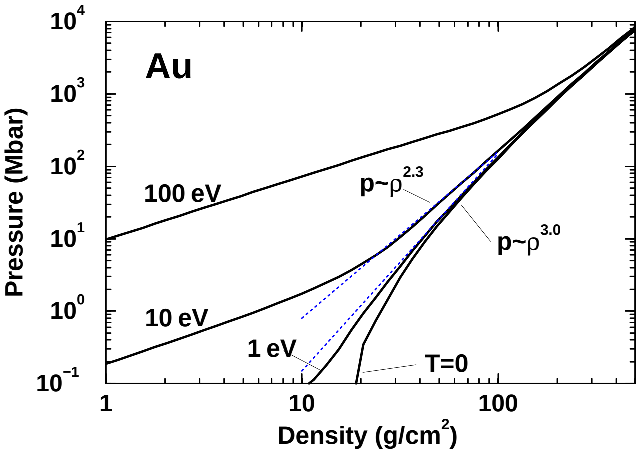

Figure 3.7 Gold pressure isotherms for T = (0, 1, 10, 100) eV, taken from the EOS table which has been used for the numerical simulations. The scalings responsible the ignition scalings of Fig. 3.6 are indicated by dotted lines.

For a more quantitative understanding of the dependence of the constant in Eq. (3.6) on ξ_t and T_t, one would have to analyze the tamper dynamics in more detail. At this place, it should be emphasized the central result that $(\rho R)_{\mathrm{ign}}$ of tamped fuel configurations has in principle no lower bound in the parameter region of interest for ICF ($m \leq 10$ mg/cm), at least not in a 1D treatment, provided that the tamper material can be kept at low entropy during the implosion.

Note also that the result (3.5) could be written alternatively in the form $\rho^{(\gamma+1)/2\gamma}R =$ const, which is the invariant for the degenerate regime. In this presentation, ignition of magnetized cylindrical targets with cold tampers scales with $\rho^{2/3}R$, setting $\gamma = 3$.

3.3 Fuel Parameter Window for Ignition

The investigation of the fuel–tamper dynamics after stagnation shows that the minimum ρR necessary for ignition and effective burn of the fuel depends significantly on the fuel mass, the tamper volume and tamper entropy. (a) For a fixed tamper entropy and fractional volume, ignition occurs only when a minimum fuel ρR is reached at stagnation. The value of the fuel ρR at ignition scales with the fuel mass m per unit length as $m^{-\kappa}$, where $0.65 \leq \kappa \leq 1.0$ depending on the fuel mass. (b) The $(\rho R)_{\min}$ saturation level decreases with decreasing tamper entropy, but this leads to higher fuel masses beyond the scope of ICF. (c) Larger tampers can also help to reduce the ignition ρR.

The results of this chapter can give a good guidance in the vast parameter space when designing cylindrical MTF targets. A possible window for MTF operation with heavy ion beams is indicated by the shaded area in Fig. 3.6. The boundaries have been selected such that the lowest possible $(\rho R)_{\mathrm{ign}}$ is obtained at fuel energies of a few MJ/cm, which may be available from future heavy ion drivers. The window corresponds to fuel radii up to 1 mm and pressures below 10 Gbar, as one may check from Fig. 3.2. A simple estimate of the target implosion time (in difference to the confinement time), necessary to reach the window, gives times of the order of 100 ns at a convergence ratio of $C_{\mathrm{r}} \simeq 10-20$. This is consistent with the pulse times of heavy ion beam drivers, cf. Chapter 5. Compared to non-magnetized ICF targets, magnetization of cylindrical DT targets allows to reduce the ignition ρR threshold at least by a factor of $10-30$, depending on the implosion history, i.e. the tamper volume and entropy. Since the driver power necessary for ignition in cylindrical ICF targets scales as $W_{\mathrm{dr}} \propto (\rho R)^2_{\mathrm{ign}}$, see Sec. 2.5, this leads to a significant reduction in the required driver power for heavy ion beam-driven magnetized cylindrical targets in the MTF ignition mode.

Chapter 4

Magnetized Implosions with Heavy Ion Beams

The heavy ion beams currently planned at GSI, Darmstadt [1] and ITEP, Moscow [3] are well suited for implosion experiments in cylindrical geometry. In such implosions, the initial pressure generated by direct beam heating will be enhanced significantly due to cylindrical convergence. When an additional magnetic field, strong enough to suppress heat conduction in radial direction, is introduced in the targets, keV temperatures and significant neutron yields are predicted here.

In order to suppress the radial diffusion of magnetic flux out of the fuel during implosion, the electrical conductivity sets (i) a lower limit for the $(UR)_0$ product of the implosion velocity U and the initial fuel radius R and, (ii) in combination with the heat conduction, a lower limit for the initial fuel temperature. Following Basko [15], these two constraints define the regime of self-sustained magnetized implosions (SSMI) which is described below. However, finite flux losses out of the fuel cause the fuel to accumulate at the fuel-pusher interface. The relative amount of fuel mass in this 'boundary layer' is determined by $(UR)_0$, which is related to the driver pulse energy deposited in the target.

The main conclusion from the results presented in this chapter is that magnetized implosions experiments can be carried out at beam energies below 100 kJ and pulse durations around 100 ns. Numerical results have been obtained by means of the 1D-MHD code DEIRA, cf. Appendix A.

4.1 Set-Up for Implosion Experiments

The main objective of the cylindrical implosions discussed here is to concentrate energy in a small amount of fuel mass in order to reach states of high energy density in matter [35]. Figure 4.1 presents a schematic view of the cylindrical target configuration for experiments with heavy ion beams. The target consists of metal tube (pusher, deposition, and tamper layer) filled with deuterium (D_2) gas at low density. The gas is referred to as the thermonuclear fuel. The boundary between fuel and metal tube is initially at radius $r = R_\mathrm{f}$ and the overall target radius is R_tot. Note that the target proportions shown in Fig. 4.1 are not to scale. The target proportions of three basic configurations considered in the following are given for reference in Table 4.1 below.

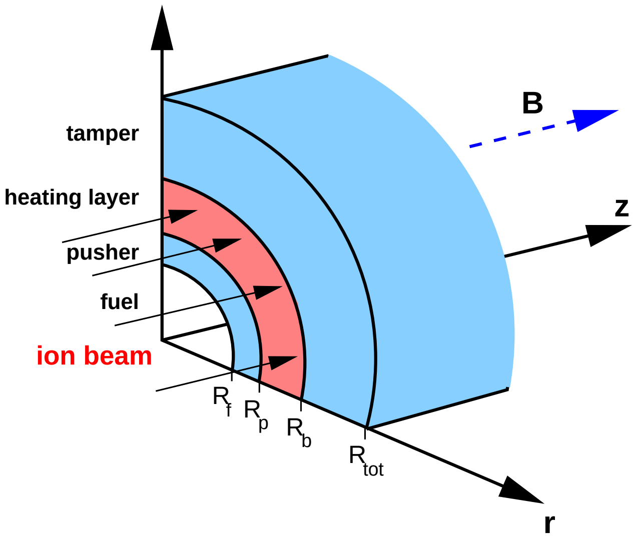

Figure 4.1 Schematic view of a cylindrical target for implosion experiments with heavy ion beams. The ion beam driving the implosion is indicated by arrows from the left. It heats the metallic tube (shaded) in the annular region $R_p < r < R_b$. The effect of the beam irradiation is a rapid expansion of the heated material in radial direction. This expansion drives the implosion. Note that the proportions shown in the figure are not to scale. The values used in the simulations are given in Table 4.1.

Energy has to be brought into the target from an external driver, namely the heavy ion beam. The conversion mechanisms in between the driver energy and the fuel at maximum compression are depicted in Fig. 4.2; implosion efficiencies are typically of the order 5 % [9]. The beam energy is deposited in the deposition layer of the target, and converted into heat energy. This causes the material to expand in the radial direction. As the pusher material is stopped by the fuel pressure, its kinetic energy is converted into thermal energy of the fuel. In order to convert a maximum amount of pusher energy into fuel heat energy, the pusher material should be as cold as possible to make it incompressible. For this reason, one has to introduce an additional layer of non-heated pusher material between fuel and deposition layer, the 'cold pusher' layer. This section will go through the three stages of Fig. 4.2, and explain more quantitatively why cold pushers are important for optimum peak pressure results in cylindrical implosions.

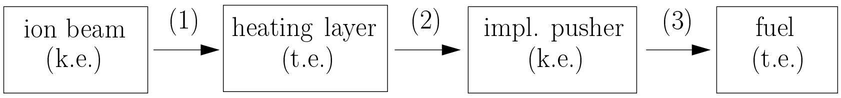

Figure 4.2 Diagram for the energy flow from ion beam to fuel. Each step in between is considered separately in the text: (1) energy deposition by the ion beam, (2) conversion from thermal energy (t.e.) of the deposition layer into kinetic energy (k.e.) of the pusher, (3) conversion to fuel heat.

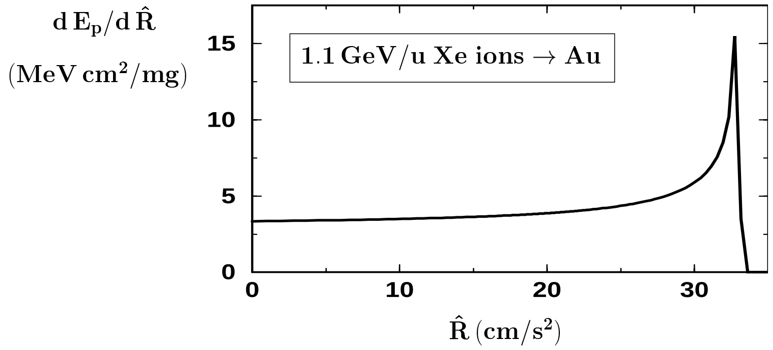

Figure 4.3 Stopping power of 1.1 GeV/u Xe ions in solid gold vs. range $\hat{R} \equiv \rho l$ along the beam direction; results are calculated from the DEIRA model (see Appendix A). The ion beam consists of $2 \times 10^{14}\,\mathrm{cm}^{-2}$ ions. Hydrodynamic motion is suppressed.

I. Energy Deposition by Heavy Ion Beams

When an intense beam of heavy ions impinges on a solid matter target, the ions gradually lose their energy as they run through the target material [35]. This energy is converted into heat energy in the target. The specific heating power P_i of an ion beam in matter can be calculated from the stopping power $dE_p/d\hat{R}$ via

$$P_\mathrm{i} = j_b\,\frac{dE_p}{d\hat{R}}\ , \tag{4.1}$$

where $d\hat{R} = \rho\,dl$ is the range increment, E_b is the ion particle energy, and j_b is the beam particle current density. Stopping powers and total ion ranges $\langle \rho l \rangle$ in matter depend in a non-trivial manner on the properties of the target material, as well as on the projectiles [35, 36]. These quantities have have been measured at GSI, Darmstadt for ion energies up to 10 MeV/nucleon, for a number of projectile/target combinations [37–39].

In order to obtain meaningful results from implosion experiments with cylindrical targets, it is important to have a uniform energy deposition throughout the deposition layer. If this is not the case, the implosion will become either non-symmetric or cone-like (or both). While the first problem is inherently two-dimensional and will not be treated here, the question of lateral uniformity is addressed in Fig. 4.3. It presents the stopping power of a beam of 2×10^{14} ions of $_{131}\mathrm{Xe}^{+54}$ at an initial energy of $E_p = 1.1\,\mathrm{GeV/u}$ in solid gold, versus the ion range $\hat{R}$ in gold at $\rho = 19.5\,\mathrm{g/cm}^3$. Assuming a focal spot radius $R_\mathrm{b} = 0.4\,\mathrm{mm}$, the parameters of the ion beam correspond to approximately 20 kJ of pulse energy. Results are calculated from the stopping power model implemented in the DEIRA code, cf. Appendix A. The conclusion from Fig. 4.3 is that the ion beam heating will be uniform to within 10 % along the first $50 - 60\,\%$ of the total ion range in gold, which corresponds to a cylinder length of about $1.0 - 1.5\,\mathrm{cm}$. In order to make sure that the energy deposition is uniform along the target axis, the cylindrical targets should be designed as 'sub-range' targets. This means that the region of strongly enhanced energy deposition, seen at large $\hat{R} \gtrsim 30\,\mathrm{g/cm}^2$ in Fig. 4.3, is outside the target. In general, the stopping power of materials with the nuclear charge Z scales $\propto Z^2$ [35]. This explains why gold is chosen as the target material for the numerical simulations presented below.

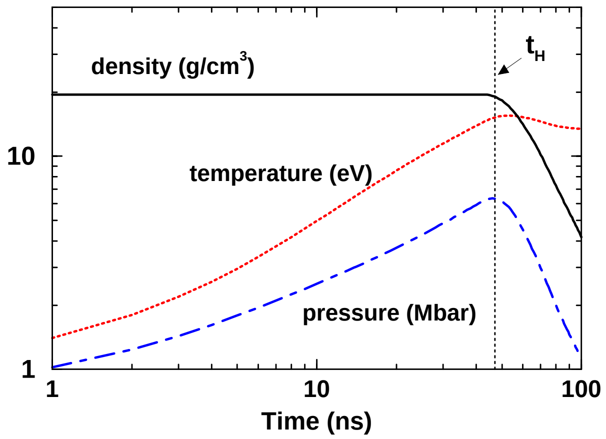

Figure 4.4 Temporal evolution of density, temperature and pressure on the axis of a solid cylindrical target, calculated by a 1D simulation. The sample is heated uniformly during 100 ns by an ion beam with specific deposition power $P_i = 2.5$ TW/g. At time $t_H \simeq 50$ ns, a rarefaction wave reaches the target axis. Therefore the density on the target axis drops, as well as temperature and pressure. Notice that the beam parameters of this case coincide with those for the solid target for $t_p = t_H$, cf. Fig. 4.5

II. Target Structure: Role of the Cold Pusher

Before examining the cylindrical implosions in more detail, a *solid* target is considered as an example. The target is assumed to be irradiated axially by a uniform ion beam on its full cross-section, i.e. $0 < r < R_{\mathrm{tot}}$. Figure 4.4 presents the temporal evolution of density, temperature and pressure on the axis. The initial target radius is equal to the focal spot radius R_{b} of the heavy ion beam, $R = R_{\mathrm{b}} = 0.4$ mm. The beam is characterized by a specific energy deposition power of $P_{\mathrm{i}} = 2.5$ TW/g, acting over a time of $t_{\mathrm{p}} = 100$ ns. As a result of the beam irradiation, the material temperature in the target rises at a constant rate until $t = t_{\mathrm{H}}$. At this time a limiting value of $10-15$ eV is reached. A rarefaction front from the outer target boundary reaches the axis, and the temperature rise is stopped by expansion cooling. Then, the ion beam continues heating the expanding material, while density and pressure on the axis drop rapidly. The rarefaction front travels approximately at the velocity of sound, given by

$$c_s \simeq \epsilon^{1/2} \simeq (P_{\mathrm{i}}\, t_{\mathrm{H}})^{1/2} \ . \tag{4.2}$$

Hence, the time $t_{\mathrm{H}} = R_{\mathrm{b}}/c_s$, at which the rarefaction front reaches the target axis, can be written as [35]

$$t_{\mathrm{H}} = \left(R_{\mathrm{b}}^2/P_{\mathrm{i}}\right)^{1/3} \ . \tag{4.3}$$

Here R_{b} is the radius of the uniformly heated cylinder, and P_{i} denotes the specific energy deposition power in the target. Numerical factors of order unity are omitted.

Formula (4.3) has important consequences with respect to the target design: if the total pulse duration t_{p} of the ion beam is much longer than the heating time t_{H}, the beam tail ($t > t_\mathrm{H}$) will impinge on hot, expanding material at low density. Energy density, i.e. pressure, will stop growing at $t \gtrsim t_\mathrm{H}$, as seen in Fig. 4.4. For the target design to be consistent with the ion beam pulse, one should therefore chose targets with $t_\mathrm{p} \simeq t_\mathrm{H}$. There are three simple irradiation schemes for cylindrical targets, each corresponding to a distinct implosion pattern

(a) *Solid targets.* They contain no fuel and are heated uniformly by the ion beams.

(b) *'Exploding liner' targets.* The targets consist of metal tubes filled with fuel gas, as seen in Fig. 4.1. Their cross-section is heated uniformly over the region

$$0 < r < R_\mathrm{b} \ , \tag{4.4}$$

while the tamper layer at $R_\mathrm{b} < r < R_\mathrm{tot}$ is not heated by the beam.

(c) *'Cold pusher' targets.* They are similar to case (b); but the inner part of the tube ('pusher') and the fuel are not heated by the ion beam, i.e. the beam covers all layers with

$$R_\mathrm{p} < r < R_\mathrm{b} \ . \tag{4.5}$$

The proportions of the three three target configurations described here are given in Table 4.1.

#		$\mathbf{R_f/R_b}$	$\mathbf{R_p/R_b}$	$\mathbf{R_{tot}/R_b}$
(a)	**solid target**	**-**	**0.0**	**1.5**
(b)	**exploding liner**	**0.7**	**-**	**1.5**
(c)	**cold pusher**	**0.55**	**0.6**	**1.5**

Table 4.1 Radial proportions of the cylindrical configurations discussed in Fig. 4.5. Given are the initial radius of the fuel-liner boundary $\mathbf{R_f}$, the inner beam radius $\mathbf{R_p}$, and the total target radius $\mathbf{R_{tot}}$, all with respect to the focal spot size $\mathbf{R_b}$ of the ion beam.

The 'hollow' ion beam profiles, essential for experiments with cold pusher targets, can be generated either by means of simple beam blockers, or by deflecting the beam in the transverse direction, e.g. by lense-like tools. The imaging of an initially full ion beam onto an annular beam profile of variable diameter has been demonstrated experimentally by Neuner *et al.* [40] at GSI, Darmstadt recently.

Figure 4.5 presents a comparison of different target configurations. The main intention is to demonstrate that the cold pusher targets (c) yield better fuel compression than the exploding liner configurations. Fig. 4.5 (i) gives the peak pressure values on the cylinder axis reached in cylindrical implosions. All implosions are driven by heavy ion beams with specific energy deposition $\epsilon = 100\,\mathrm{kJ/g}$. Their pulse duration t_p, and their specific deposition power P_i are varied simultaneously, so that $\epsilon = P_\mathrm{i}\, t_\mathrm{p}$ remains constant. Pressure is plotted versus specific deposition power P_i, as obtained from 1D computer simulations without magnetic field. The usual heat loss mechanisms, i.e. bremsstrahlung and heat conduction by electrons and ions are fully taken into account. For all cases shown in Fig. 4.5, the focal spot size is fixed at $R_\mathrm{b} = 0.4\,\mathrm{mm}$. The conclusion from Fig. 4.5 (i) is, firstly, that the peak pressures in the exploding liner targets are slightly larger than those in the solid target and, secondly, that peak pressures in cold pusher implosions are typically by one order of magnitude larger than the corresponding results from exploding liner implosions.

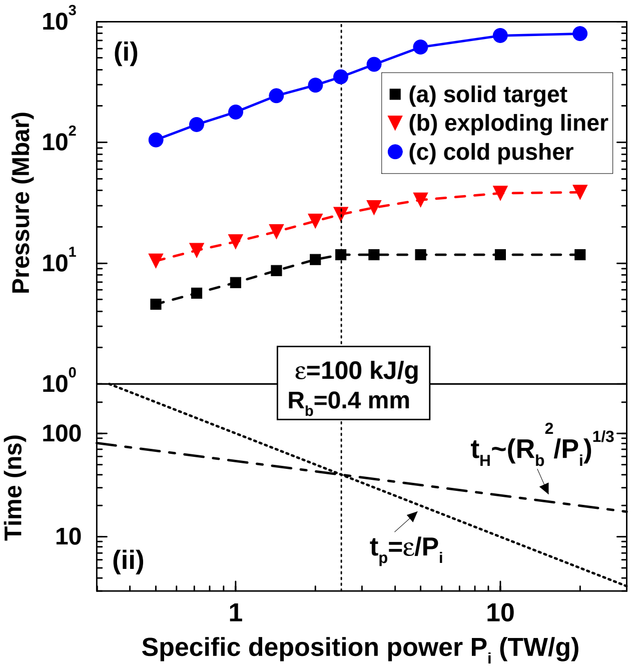

Figure 4.5 Comparison of the peak pressures reached in exploding liner and cold pusher targets with a solid target. Part (i) shows peak pressure results of the three distinct target configurations vs. the specific deposition power $\mathrm{P_i}$. Initial target proportions are given in Table 4.1. Part (ii) compares the pulse duration $\mathrm{t_p}$ of the ion beam with the heating time scale $\mathrm{t_H}$, see Eq. (4.3). For all results in this figure, the focal spot size of the beam is kept constant at $\mathrm{R_b} = 0.4\,\mathrm{mm}$; the pulse duration $\mathrm{t_p}$ and the specific deposition power P_i are varied simultaneously, so that the specific energy deposition $\epsilon = 100\,\mathrm{kJ/g}$ remains constant. The deposition power $\mathrm{P_i}$, which corresponds to equal values of $\mathrm{t_p}$ and $\mathrm{t_H}$, is marked by a dotted vertical line; this value has been chosen for the example shown in Fig. 4.4.

Figure 4.5 (ii) gives pulse duration t_p and heating time t_H, defined in Eq. (4.3), versus specific deposition power P_i. Due to their different scalings with P_i, the curves for t_p and t_H cross each other at $P_\mathrm{i} \simeq 2.5\,\mathrm{TW/g}$ and $t_\mathrm{H} \simeq t_\mathrm{p} \simeq 50\,\mathrm{ns}$. These parameters have been chosen for the example given in Fig. 4.4.

Notice in Fig. 4.5 (i) the saturation of peak pressure values for large values of driver power P_i. It can be explained as follows: in a solid target, beam deposition powers P_i beyond 2.5 TW/g will not yield larger peak pressures, since the heating time t_H becomes larger than the pulse duration t_p. For long pulses with $t_\mathrm{p} > t_\mathrm{H}$, shown in the left part of Fig. 4.5, the peak pressure values p_max in the target scale with P_i according to

$$p_\mathrm{max} \propto \rho\, \epsilon_\mathrm{max} \propto (P_\mathrm{i}\, t_\mathrm{H}) \propto P_\mathrm{i}^{2/3} \ , \tag{4.6}$$

assuming constant target material density ρ and radius R_b. For 'too short' beam pulses with $t_\mathrm{p} \leq t_\mathrm{H}$, corresponding to large values of P_i, the maximum pressure is simply related to the total amount of specific heat energy ϵ =const deposited in the target.

The enhanced peak pressure results in cold pusher implosions can be explained by the self-similar solution of the ideal gas-dynamic equations discussed in Chapter 6. The central result of the similarity analysis is that the peak pressure p_{s} of imploding hollow shells scales with the Mach number $M_0 \equiv v_{\mathrm{imp}}/c_s \propto T_s^{-1/2}$ of the imploding shell material as

$$p_{\mathrm{s}}/p_0 \propto M_0^{2(n+1)/(\gamma+1)} \; . \tag{4.7}$$

Here p_0 is the drive pressure of the implosion, and the scaling depends on shell geometry ($n = 2$ for cylindrical shells) and adiabatic exponent γ of the shell material. For $\gamma = 5/3$, one obtains $p_{\mathrm{s}} \propto T_s^{-9/8}$.

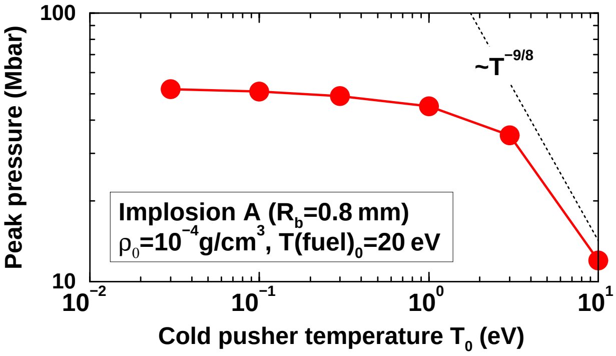

Figure 4.6 Dependence of the peak fuel pressure on the initial pusher temperature T_0. Results are shown for non-magnetized adiabatic implosions of target $\mathcal{A}$ (see Table 4.2 below), where all energy loss mechanisms are suppressed. The initial fuel density is $1 \times 10^{-4}\,\mathrm{g/cm^3}$, the initial fuel temperature is 20 eV, and the focal spot size of the heavy ion beam is $R_{\mathrm{b}} = 0.4$ mm in all cases. The peak pressure scaling $p_{\max} \propto T_0^{-9/8}$, given in Eq. (4.7), is indicated by a dotted line. The drop of the peak pressure values at $T_0 \approx 3$ eV comes from the EOS of the cold pusher material.

This is confirmed qualitatively by the results from hydrodynamic simulations presented in Fig. 4.6. The simulations correspond to non-magnetized implosions of target $\mathcal{A}$ described below (see Table 4.1), with fixed initial values of fuel density $\rho_0 = 10^{-4}\,\mathrm{g/cm^3}$ and fuel temperature 20 eV; only the initial temperature T_0 of the cold pusher is varied in a range from the usual value $T_0 = 0.03$ eV, up to a maximum value of 10 eV. The conclusion of Fig. 4.6 is that for small T_0, the compression is nearly independent of temperature, while it drops noticeably at about 3 eV. This behavior can be explained by means of EOS properties of the pusher material; cf. Chapter 3.

To reach optimum fuel compression, only cold pusher configurations will be considered in what follows. An immediate consequence of the fixed target proportions, given in Table 4.1 is that the radial layer structure of each target can be characterized by a single number, e.g. the spot radius R_{b} of the ion beam. The radial target proportions used here correspond to an initial aspect ratio $\mathrm{A_r}$ of the cold pusher

$$\mathrm{A_r} = \frac{R_{\mathrm{p}}}{(R_{\mathrm{p}} - R_{\mathrm{f}})} = 12 \; . \tag{4.8}$$

This value has been chosen for two reasons: firstly, the ratio of the cold pusher mass m_{p} to the deposition layer mass m_{h} is hereby fixed at a value of about

$$\frac{m_{\mathrm{p}}}{m_{\mathrm{h}}} \equiv \frac{R_{\mathrm{p}}^2 - R_{\mathrm{f}}^2}{R_{\mathrm{b}}^2 - R_{\mathrm{p}}^2} \simeq 0.1 \; , \tag{4.9}$$

close to the optimum payload–to–shell mass ratio of an ideal rocket [9]. It yields an optimum conversion efficiency between the kinetic energies of exhaust gas and payload.

The second reason for this choice of the pusher aspect ratio is hydrodynamic stability of the imploding pusher. In order to prevent the pusher from breaking up during the implosion, it should not be too thin. Stability will be briefly discussed in Sec. 4.5 below.

Expansion in axial direction is not accounted for in the present 1D simulations. This should be no problem for sufficiently long target cylinders; more detailed investigations in the future will have to use 2D simulations.

4.2 Energy Loss Mechanisms in Quasi-Adiabatic Implosions

Before discussing the magnetized implosions in detail, it is helpful to examine the behavior of the main fuel parameters in idealized 'quasi-adiabatic' implosions, in which the profiles of fuel temperature and density are assumed to be uniform in space during the implosion. Under this assumption, their scalings with the in-flight convergence ratio $C_r(t) = R_\mathrm{f}(t_0)/R_\mathrm{f}(t)$ are given by

$$\rho = \rho_0 \, {C_r}^2 \ , \ \rho R = (\rho R)_0 \, C_r \ , \ T = T_0 \, {C_r}^{4/3} \ . \tag{4.10}$$

In such idealized implosions, it is possible to reach keV temperatures in the fuel by starting from initial values of $T_0 \simeq 20 - 30\,\mathrm{eV}$, and assuming final convergence ratios of $C_r \simeq 20 - 30$. Final keV temperatures in D_2 fuel would correspond to a significant generation of thermonuclear fusion neutrons.

I. Bremsstrahlung and Heat Conduction

The major heat loss mechanisms out of the fuel are bremsstrahlung and thermal heat conduction. In a quasi-adiabatic implosion, one can determine the relative role of these two mechanisms by considering the typical time scales on which the plasma loses energy by the respective process; this time is compared to the implosion time $t_\mathrm{i} = R_\mathrm{f}/U$. Here R_f denotes the initial position of the fuel-pusher boundary and U is the averaged implosion velocity. The bremsstrahlung loss time t_br is calculated from the specific energy loss rate $q_\mathrm{br} = 4.8 \times 10^{23} \, \rho \, T_\mathrm{keV}^{1/2} \ \mathrm{erg\,g^{-1}\ sec^{-1}}$, given in Chapter 2, and from the fuel temperature T via

$$c_0 \frac{dT}{dt} \simeq c_0 \frac{T}{t_\mathrm{br}} \simeq q_\mathrm{br} \ , \tag{4.11}$$

where $c_0 = 1.5 \times 10^{15}\,\mathrm{erg\,g^{-1}\,keV^{-1}}$ is the heat capacity of deuterium plasma. Note that the above expression for q_br is pessimistic: it assumes that the gold pusher is optically thin for the radiation, which is not the case in general. In a D_2 plasma, the ratio of the bremsstrahlung cooling time scale t_br to the implosion time t_i assumes the form

$$\Gamma_\mathrm{br} \equiv \frac{t_\mathrm{br}}{t_\mathrm{i}} \simeq 4.0 \times 10^{-9} \frac{U T_\mathrm{keV}^{1/2}}{\rho R} \propto \frac{T_\mathrm{0,keV}^{1/2}}{(\rho R)_0} U {C_r}^{-1/3} \ , \tag{4.12}$$

where the last expression has been calculated by means of the scaling (4.10), and $C_r = C_r(t)$ refers to the time-dependent radial convergence of the pusher. Obviously, the dependence of Γ_ff on C_r is only weak. Hence, bremsstrahlung losses out of the fuel volume can be reduced by choosing appropriately low initial values of $(\rho R)_0$.

Analogously, the role of heat conduction losses from the fuel volume can be estimated from the specific energy loss rate $q_{\mathrm{hc}} \simeq \kappa kT/(\rho R^2)$. Here κ is the heat conduction coefficient [20]. The corresponding loss time t_{hc} is calculated from an equation similar to Eq. (4.11). The ratio of the loss time t_{hc} and the implosion time t_{i} coincides with the definition of the Peclét number

$$\mathrm{Pe} \equiv \frac{t_{\mathrm{hc}}}{t_{\mathrm{i}}} = \frac{\rho U R}{\kappa} \ . \tag{4.13}$$

In the case of a non-magnetized ideal plasma, Spitzer's formula [20] can be used for the heat conduction $\kappa \propto \ T^{5/2}$, and one obtains the scaling

$$\mathrm{Pe} \propto \frac{(\rho R)_0}{T_0^{5/2}} U {C_r}^{-7/3} \ . \tag{4.14}$$

This means that the Peclét number decreases rapidly as the implosion proceeds. As soon as it drops below unity, the fuel starts losing entropy. Note that the Peclét number scales directly with $(\rho R)_0$, while the analogous parameter Γ_{br} for the bremsstrahlung losses scales inversely proportional with $(\rho R)_0$. This means that, trying to maximize both Γ_{br} and the Peclét number simultaneously, one can find an optimum value for the initial fuel density radius product $(\rho R)_0$ for each cylindrical implosion.

II. Magnetic Field Diffusion and Heat Conduction

Now assume that, prior to the implosions, a magnetic field B is introduced into the cylindrical target. It is directed along the z-direction parallel to the target axis, or, in other words, transverse to the radial direction of heat losses. The key parameter entering the description of the plasma and including the effect of the magnetic field on the plasma electrons is the magnetization [20]

$$x_e \equiv \omega_e \tau_e = 3.18 \times 10^{-7} \bar{A} \frac{B}{\rho} \frac{T_{\mathrm{keV}}^{3/2}}{L_{ei}} \propto {C_r}^2 \ . \tag{4.15}$$

Here $\omega_e = eB/m_e c$ is the electron gyrofrequency, the electron-ion collision time is given by τ_e, cf. Eq. (2.13), $\bar{A} = 2$ is the atomic number of the D_2 fuel, and L_{ei} is the Coulomb logarithm [20]; it depends only weakly on the fuel parameters. The last relation in Eq. (4.15) gives the scaling of x_e with the radial convergence ratio C_r. If the Braginskii formula (2.11) is substituted for the transverse electron heat conduction coefficient $\kappa = \kappa_{e\perp}$ into Eq. (4.13), one obtains the following expression for the Peclét number

$$\mathrm{Pe} = 3.15 \times 10^{-5} U R \frac{\rho L_{ei}}{\bar{A} T_{\mathrm{keV}}^{5/2}} \frac{3.77 + 14.79 x_e^2 + x_e^4}{11.92 + 4.66 x_e^2} \ . \tag{4.16}$$

In a magnetized plasma, where $x_e \gg 1$, the electron heat conduction is suppressed by a factor of approximately x_e^{-2}, and the Peclét number increases correspondingly. This means that the heat insulation will improve as

$$\mathrm{Pe} \propto U {C_r}^{-1} {C_r}^{-10/3} {C_r}^4 = U {C_r}^{5/3} \ . \tag{4.17}$$

Regarding the role of heat conduction by ions and by electrons, note that the electronic heat conduction dominates in non-magnetized plasmas, i.e. $\kappa_e/\kappa_i \simeq \sqrt{m_i/m_e}$, while the ionic heat conduction dominates in magnetized plasmas; in strong magnetic fields, i.e. $x_e \gg x_i \gg 1$, the ion heat conduction will dominate by a factor $\kappa_i/\kappa_e \simeq \sqrt{m_i/m_e}$. However, in the present analysis of the loss mechanisms, only qualitative aspects of the heat conduction losses will be treated. For simplicity, the effects of ion heat conduction are neglected for the moment, and only electron heat conduction is considered. In the numerical simulations, both electron and ion heat conduction are fully accounted for.

A central mechanism in magnetized implosions is the radial diffusion of the magnetic field. Full conservation of the magnetic flux occurs only in the case of the so-called 'ideal' MHD with infinite electrical conductivity. In implosions with finite plasma conductivity, however, the magnetic fields tends to diffuse out of the plasma during the characteristic time t_{md}, which can be derived as follows. The evolution of the axial magnetic field B in cylinder geometry is described by the diffusion equation [41]

$$\frac{\partial B}{\partial t} + \frac{1}{r}\frac{\partial}{\partial r}(rUB) = \frac{1}{r}\frac{\partial}{\partial r}\left(\frac{c^2}{4\pi\sigma} r \frac{\partial B}{\partial r}\right) , \tag{4.18}$$

where U denotes the radial fluid velocity, and $\sigma \equiv \sigma_\perp$ is the transverse electrical conductivity of the plasma. In the static case ($U = 0$), one finds the diffusion time scale

$$t_{\mathrm{md}} = \frac{4\pi\sigma L^2}{c^2} . \tag{4.19}$$

Here L denotes a typical length scale of the plasma, e.g. the initial fuel radius R_{f}. For short times $t \ll t_{\mathrm{md}}$, the magnetic field can be considered to be 'frozen-in'. This means that the conductivity σ is large enough to neglect the right-hand side of the diffusion equation (4.18). An immediate consequence of this approximation is that the quantity B/ρ is conserved for each mass element in cylindrical implosions. In the opposite case of large times $t \gg t_{\mathrm{md}}$, one has a finite conductivity σ. The magnetic field diffuses out of the plasma. For typical plasma velocities U, one can distinguish both situations, the frozen-in and the diffusing field, by using the magnetic Reynolds number

$$\mathrm{Rm} = \frac{t_{\mathrm{md}}}{t_{\mathrm{i}}} = \frac{U t_{\mathrm{md}}}{R} = \frac{4\pi\sigma}{c^2} UR . \tag{4.20}$$

This means that for $\mathrm{Rm} \gg 1$, the magnetic field will be almost frozen into the plasma.

In order to confine the magnetic flux in the fuel volume, i.e. $\mathrm{Rm} \gg 1$, it is necessary to have high electrical conductivity either in the fuel plasma or in the pusher material (or both). Figure 4.7 presents the dependence of the electrical plasma conductivity for fuel and pusher versus temperature. While the fuel conductivity at large temperatures is almost density-independent, and follows the Spitzer formula [42], the pusher conductivity is given for two different densities of gold. At low temperatures, the pusher conductivity scales inversely with temperature. The electrical conductivity of a plasma is essentially independent of the magnetic field [20].

It turns out that the confinement of magnetic flux by the fuel itself, and by the pusher material are both important for the magnetized implosions. Their respective role in the

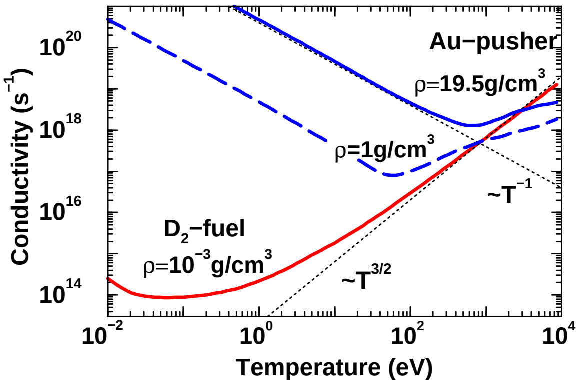

Figure 4.7 Electrical conductivity vs. temperature for D_2 gas at low density, and Au at two different densities given in the figure. Results are taken from the conductivity formula used in the numerical simulations, see Appendix A. The Spitzer limit for an ideal plasma $\sigma \propto T^{3/2}$ and the typical scaling $\sigma \propto T^{-1}$ of a metal conductor at low temperatures are indicated by dotted lines.

course of the implosion will be examined in the next section. For simplicity, however, the following analysis will mainly consider the fuel conductivity. The magnetic Reynolds number is then given by

$$\mathrm{Rm}_f = \frac{4\pi\sigma}{c^2} UR = 0.02\, UR\, T_{\mathrm{keV}}^{3/2}/L_{ei} \propto UC_r \ . \tag{4.21}$$

The last relation gives the scaling of Rm with the convergence ratio C_r in quasi-adiabatic implosions, cf. Eq. (4.10).

4.3 Self-Sustained Magnetized Implosions

Having introduced the key dimensionless parameters x_e, Pe, Rm_f, Rm_p for the description of heat- and magnetic diffusion in cylindrical implosions, these parameters will be used to derive initial conditions for well-magnetized implosions. The differences between characteristic magnetized implosions, and corresponding non-magnetized cases will be discussed quantitatively.

The scalings of the key dimensionless parameters with the radial convergence ratio C_r, discussed in the previous section, are given here for reference

$$x_e \propto {C_r}^2 \ , \ \mathrm{Pe} \propto U{C_r}^{5/3} \ , \ \mathrm{Rm} \propto UC_r \ . \tag{4.22}$$

Thermal insulation, characterized by Pe, as well as that of the magnetic field in the fuel plasma, characterized by Rm, improve during magnetized implosions. Once the values

$$x_e \gg 1 \ , \ \mathrm{Pe} \gg 1 \ , \ \mathrm{Rm} \gg 1 \tag{4.23}$$

are established, an initially magnetized implosion will remain so. On the other hand, if the implosion is not magnetized initially ($x_e \lesssim 1$), the scaling $\mathrm{Pe} \propto {C_r}^{-7/3}$ given in

Eq. (4.14) shows that the fuel entropy is lost rapidly. As a consequence, the magnetic Reynolds number of the fuel will drop and the magnetic flux will diffuse out as well. One can thus conclude that magnetized implosions are particularly sensitive to the choice of initial conditions.

I. Initial Conditions for Self-Sustained Magnetized Implosions

In order to have a well-magnetized implosion, it is not necessary to provide $x_e \gg 1$ from the very beginning: starting with a non-magnetized plasma $x_e \lesssim 1$ and a sufficiently large magnetic Reynolds number is also possible. In this situation the fuel will lose entropy until the magnetization $x_e \propto {C_r}^2$ is large enough that the fuel enters the scaling (4.22). If, however, the magnetic Reynolds number drops below unity before this happens, the implosion will continue to lose entropy and magnetic flux.

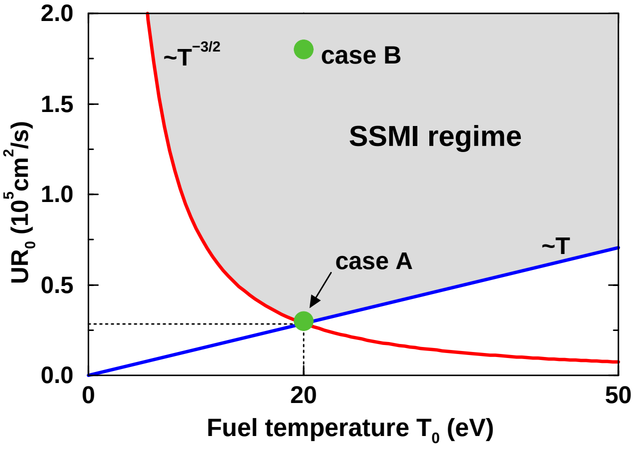

Figure 4.8 Initial conditions for self-sustained magnetized implosions, represented in a parametric plane spanned by the initial fuel temperature T_0 and the product of implosion velocity and initial fuel radius $(UR)_0$; the lines that mark the SSMI regime are defined in Eq. (4.26)–(4.27). While the limit $\propto T$ corresponds to heat conduction losses, the curve $\propto T^{-3/2}$ corresponds to the magnetic diffusion. The optimum values of T_0 and $(UR)_0$ for an initial magnetic $B_0 = 3 \times 10^5$ G are indicated by dotted lines. They correspond to $L_{ei} \simeq 7$, and $\mathrm{Pe}_0 = \mathrm{Rm}_0 \simeq 1$. The initial parameters of the targets $\mathcal{A}$ and target $\mathcal{B}$ are marked by dots; they are discussed in Table 4.2 below.

In view of the scaling $\mathrm{Pe} \propto U{C_r}^{-7/3}$ for the Peclét number in non-magnetized plasmas and $x_e \propto {C_r}^2$, one can combine the two initial conditions $x_e \gg 1$ and $\mathrm{Pe} \gg 1$ to

$$x_e \mathrm{Pe}_1 = 1.18 \times 10^{-11} \frac{U_0 R_0 B_0}{T_{0,\mathrm{keV}}} \geq \mathrm{Pe}_0 \;, \tag{4.24}$$

where Pe_1 denotes the Peclét number for $x_e = 1$, and $\mathrm{Pe}_1 \gtrsim 1$. The second requirement for a well-magnetized implosion is the constraint

$$\mathrm{Rm} = 0.02 \frac{T_{0,\mathrm{keV}}^{3/2}}{L_{ei}} U R_0 \geq \mathrm{Rm}_0 \tag{4.25}$$

on the Reynolds number (4.21), with $\mathrm{Rm}_0 \gtrsim 1$. These two relations are the initial conditions for the regime of self-sustained magnetized implosions (SSMI). They are illustrated by Fig. 4.8, which shows the borders of the SSMI regime as given in Eqs (4.24)-(4.25). The combination of both conditions gives an 'optimum' initial fuel temperature

$$T_0^{\mathrm{opt}} = 20\,\mathrm{eV} \left(\frac{B_0}{10^5\mathrm{G}} \right)^{2/5} , \tag{4.26}$$

and a minimum for $(UR)_0$

$$UR_0 \geq 1.8 \times 10^4 \frac{\mathrm{cm}^2}{\mathrm{s}} \left(\frac{10^5\mathrm{G}}{B_0} \right)^{3/5} \mathrm{Pe}_0^{3/5} \left(\mathrm{Rm}_0 L_{ei} \right)^{2/5} . \tag{4.27}$$

Note that the lower limit on $(UR)_0$ is independent of the initial fuel temperature T_0, density ρ_0 and the fuel volume radius R. The fuel density ρ_0 does not enter the initial conditions (4.26) for the magnetized implosions either. It affects only the role of the bremsstrahlung losses (4.12). Like the initial value of the magnetic field B_0 it has to be adjusted for each implosion in order to find an optimum value.

Deriving the initial conditions for the SSMI regime with regard to the magnetic Reynolds number Rm_p of the pusher, as mentioned at the end of the previous section, is less interesting from a physical point of view. When combining conditions (4.24) and (4.25), the T^{-1} dependences cancel out and one obtains no lower limit for the fuel temperature. This would apply only to magnetized implosions at low temperatures, where the pusher conductivity is always larger than that of the fuel.

II. Evolution of the Fuel Parameters

This section studies two particular magnetized implosions $\mathcal{A}$ and $\mathcal{B}$ in detail. Both implosions are driven by ion beams with the same specific deposition power $P_{\mathrm{i}} = 1\,\mathrm{TW/g}$ and 100 ns pulse duration. Initial parameters, and results of MHD simulations are given in Table 4.2. The main difference between cases $\mathcal{A}$ and $\mathcal{B}$ lies in the choice of the beam radius R_{b}, which is reflected in the $(UR)_0$ product. Since the implosion velocity $U \propto \epsilon = \sqrt{P_{\mathrm{i}} t_{\mathrm{H}}}$, one has $UR \propto P_{\mathrm{i}}^{1/3} R_{\mathrm{b}}^{4/3}$, as explained in Sec. 4.4. The corresponding $(UR)_0$ values of implosions $\mathcal{A}$ and $\mathcal{B}$ are represented in Fig. 4.8 above and in Table 4.2.

Further differences between implosions $\mathcal{A}$ and $\mathcal{B}$ are their respective initial values of fuel density ρ_0 and the magnetic field B_0. As already mentioned, ρ_0 is a free parameter for magnetized implosions; this is to say that it has to be adjusted for each individual implosion, in order to reach optimum neutron yields. For too small fuel densities, the

#	$\mathbf{R_b}$ mm	ρ_0 $\mathbf{g/cm^3}$	$\mathbf{B_0}$ T	$\mathbf{(UR)_0}$ $\mathbf{cm^2/s}$	$\mathbf{T_m}$ keV	$\mathbf{N_n}$ $\mathbf{cm^{-1}}$	$\mathbf{T_m(B=0)}$ keV	$\mathbf{N_n(B=0)}$ $\mathbf{cm^{-1}}$
$\mathcal{A}$	0.8	1×10^{-4}	30	2.4×10^4	0.3	10^4	0.2	10^3
$\mathcal{B}$	4.0	3×10^{-5}	10	1.7×10^5	1.1	10^9	0.4	2×10^6

Table 4.2 Parameters of magnetized implosions $\mathcal{A}$ and $\mathcal{B}$. Given are the focal spot radius R_b of the ion beam, initial fuel density ρ_0, initial magnetic field B_0, and the value of the $(UR)_0$ product. Corresponding target proportions can be derived from R_b and Table 4.1. Both implosions are driven by an ion beam with $P_i = 1\,\mathrm{TW/g}$, the initial fuel temperature is $T_0 = 20\,\mathrm{eV}$. Also given are the implosion results, i.e. peak temperature T_m and expected neutron yield N_n from D_2 thermonuclear reactions. Results of corresponding non-magnetized implosions are given as well.

yield drops because of a too little amount of fuel; for too large densities, the yield drops as a result of bremsstrahlung cooling. Similarly, the optimum value for the initial magnetic field B lies in between negligible magnetic insulation effects, and strong magnetic fields, hindering the fuel compression by means of the magnetic pressure p_m. Notice that $p_m = B^2/8\pi \propto \rho^2$ in quasi-adiabatic implosions with frozen-in magnetic field. This growth is faster that that of the thermal pressure $p \propto \rho^{5/3}$. Hence, the magnetic pressure typically dominates the fuel at large compression, as will be discussed below.

The choice of the focal spot radius $R_b = 0.8\,\mathrm{mm}$ in implosion $\mathcal{A}$ is guided by the parameters of the heavy ion beam envisioned at the TWAC accelerator [3]. Target $\mathcal{A}$ absorbs a total pulse energy of approximately 20 kJ. The five-times-larger target $\mathcal{B}$, on the other hand, corresponds to a well-magnetized implosion. It would absorb a total beam energy which is approximately 75 times larger than the pulse energy for target $\mathcal{A}$, following the pulse energy scaling derived in Sec. 4.4 below. Additionally, a third magnetized implosion with $R_b = 0.4\,\mathrm{mm}$ and $P_i = 1\,\mathrm{TW/g}$ has been considered. This case, however, is not discussed here, since peak temperature and neutron yield are essentially equal to the corresponding non-magnetized implosion. The reason for this negative result is that the $(UR)_0$ product lies significantly below the SSMI threshold. In other words, the magnetic Reynolds number of the implosion is too low, and the magnetic field diffuses rapidly out of the fuel volume, followed by the heat energy.

Qualitatively, the results of the comparison between implosions $\mathcal{A}$ and $\mathcal{B}$ are the following: (i) only if the SSMI conditions are fulfilled, the magnetized implosions yield larger peak temperatures than corresponding non-magnetized implosions. (ii) The enhancement of the peak fuel temperature, caused by the magnetic insulation, grows with the $(UR)_0$ product. These two statements will now be examined quantitatively in terms of the parameters introduced by the previous section.

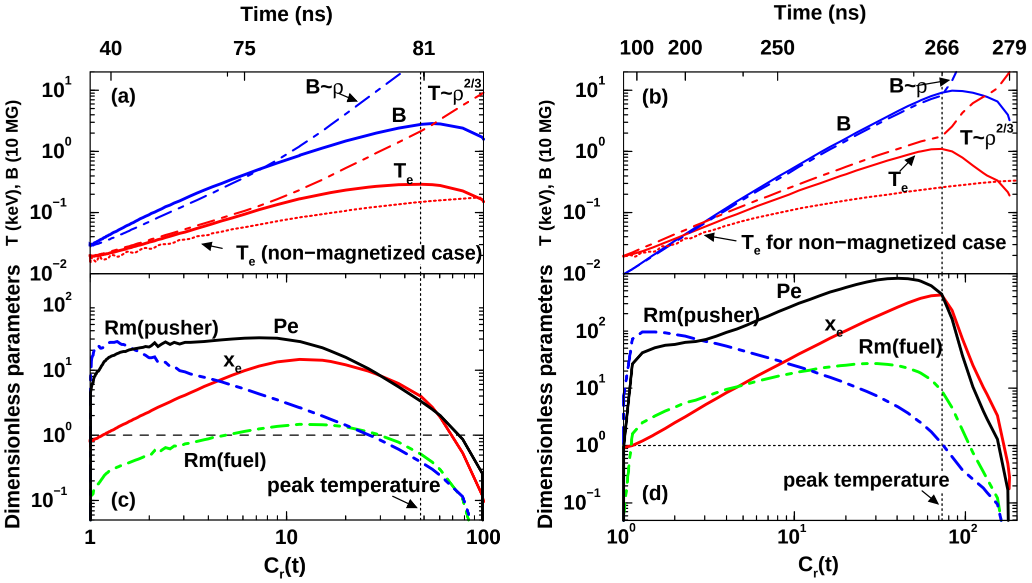

Figure 4.9 Evolution of fuel and pusher parameters in the magnetized implosions $\mathcal{A}$, with $\mathrm{R_b} = 0.8\,\mathrm{mm}$, and $\mathcal{B}$, with $\mathrm{R_b} = 4.0\,\mathrm{mm}$ vs. the radial convergence $\mathrm{R_f}(0)/\mathrm{R_f}(\mathrm{t})$; see Table 4.2 for details. The left (right) part of the figure refers to target $\mathcal{A}(\mathcal{B})$. Time is given explicitly on top of the diagrams. The upper parts (a) and (b) show the evolution of fuel temperature and the magnetic field on the axis (full curves), and their respective values in the limit of a quasi-adiabatic implosion with a fully frozen-in magnetic field, following the scalings (4.28), given also in the figure (dashed curves). The time at which the peak fuel temperature is reached is marked by vertical dotted lines. Also given is the evolution of the fuel temperature in the corresponding non-magnetized implosions (dotted curves). The lower parts (c) and (d) discuss the evolution of relevant dimensionless parameters of fuel and pusher in the magnetized implosions, cf. Sec. 4.3; these are the magnetization $\mathrm{x_e}$, the Peclét number Pe, the magnetic Reynolds number of the fuel $\mathrm{Rm_f}$, and the magnetic Reynolds number of the pusher $\mathrm{Rm_p}$. As soon as both Reynolds numbers have dropped below unity, the magnetic field rapidly diffuses out of the fuel. This limit is marked by dotted horizontal lines.

Figure 4.9 presents the evolution of the principal parameters in the implosions of the two targets $\mathcal{A}$ and $\mathcal{B}$ versus the radial convergence $C_r(t) \equiv R_\mathrm{f}(0)/R_\mathrm{f}(t)$. The corresponding time is given explicitly on top of the diagrams. First consider the upper parts (a) and (b) of Fig. 4.9: one can see that the fuel parameters evolve approximately as predicted by the scalings

$$B \propto \rho\ , \quad T \propto \rho^{2/3} \tag{4.28}$$

for the quasi-adiabatic limit, where $\rho \propto (C_r(t))^2$. Scalings (4.28) hold up to $C_r = 20-30$ in implosion $\mathcal{A}$, and even further in implosion $\mathcal{B}$. Deviations from the ideal scalings at low $C_r(t)$ are related with deviations from the uniform flow pattern; this phenomenon will be examined in the next section.

The lower parts (c) and (d) of Fig. 4.9 discuss the behavior of the dimensionless quantities, i.e. magnetization x_e, Peclét number Pe, magnetic Reynolds number of the

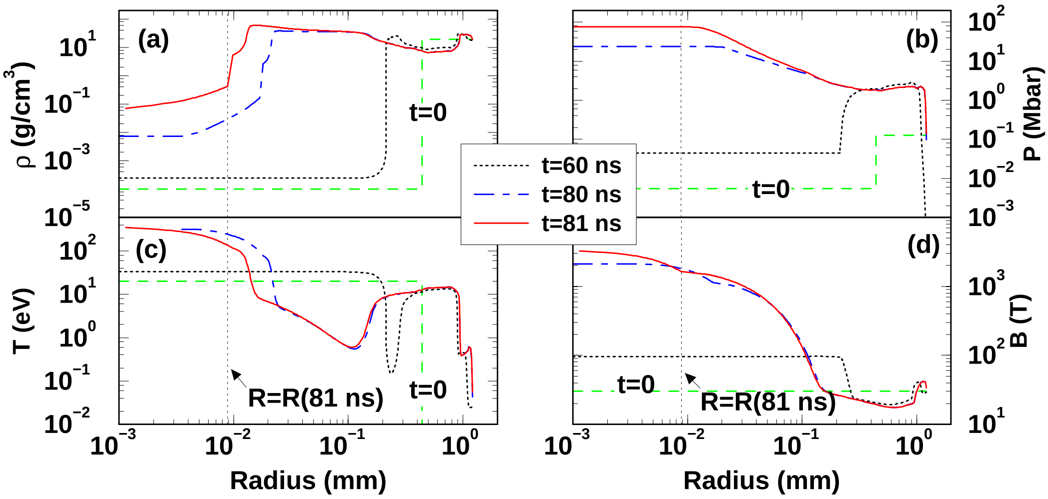

Figure 4.10 Radial profiles of density, temperature, pressure, and the magnetic field during the implosion of $\mathcal{A}$ for three different times; these are t = 60 ns when the pusher has traveled half the distance to the target axis, t = 80 ns when the convergence ratio $C_r = 24$ is reached, and t = 81 ns when the peak temperature is achieved in the fuel. The radial position of the fuel-pusher boundary at the peak fuel temperature is indicated by vertical dotted lines.

fuel $\mathrm{Rm_f}$, and magnetic Reynolds number of the pusher $\mathrm{Rm_p}$. One observes that, once the Reynolds number of the pusher falls below unity at $C_r = 30$ ($C_r = 70$) in implosion $\mathcal{A}(\mathcal{B})$, the fuel starts loosing magnetic flux and entropy, as observed in the subsequent decrease of x_e and Pe. This underlines the importance of the the magnetic field insulation. Parts (c) and (d) of Fig. 4.9 also demonstrate the different roles of fuel and pusher in confining the magnetic field, reflected by the two Reynolds numbers $\mathrm{Rm_f}$ and $\mathrm{Rm_p}$ of fuel and pusher, respectively.

In the well-magnetized implosion $\mathcal{B}$, presented in part (d) of Fig. 4.9, the time when the peak fuel temperature is reached coincides with the time when Rm_p, the magnetic Reynolds number of the pusher, drops below unity. This suggests that the pusher takes the main responsibility for the magnetic field confinement in the initial stage of the implosion, due the large electrical conductivity of the pusher material at low temperatures, cf. Fig. 4.7.

Next, consider the neutron yields from implosions $\mathcal{A}$ and $\mathcal{B}$, as given in Table 4.2. A comparison of the total neutron yields from the two magnetized cases with the results from corresponding non-magnetized cases shows that the enhancement of the neutron yield in target $\mathcal{A}$ due to the magnetic insulation is below a factor of 10. Simulations indicate that most of the neutrons from implosions $\mathcal{A}$ and $\mathcal{B}$ are generated at extremely large compression, i.e. $C_r > 100$; however, such compressions may be not achievable in real experiments. Neglecting in implosion $\mathcal{A}$ those neutrons generated at convergence ratios $C_r(t) > 30$, which is a more realistic value for implosion experiments, the neutron yield enhancement rises up to a ratio of 1000. This difference would yield a much better experimental signature of the magnetic field effect than the factor of 10 mentioned earlier.

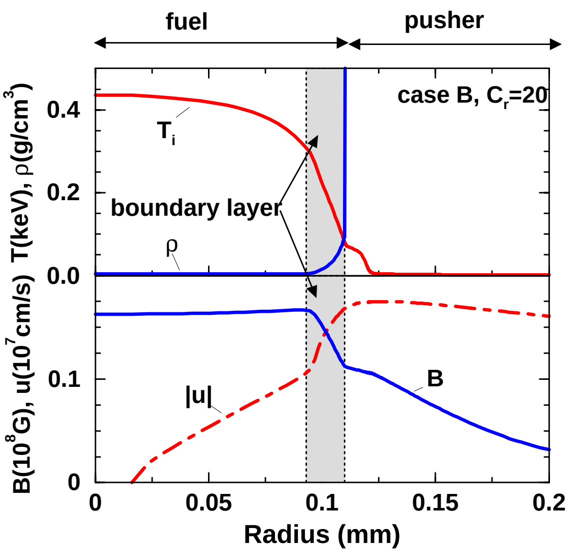

Figure 4.11 Radial profiles of density ρ, ion temperature T_i, magnetic field B, and the (negative) flow velocity U in the inner part of target $\mathcal{B}$ (cf. Table 4.2), at time t $=$ 260 ns, corresponding to $C_r = 20$. The region of strong density and magnetic field gradients is called boundary layer (marked by a grey band). Domains of fuel and pusher material are marked by arrows on top of the figure.

Implosion $\mathcal{A}$ is described in more detail in Fig. 4.10. Radial profiles of density, the total pressure (magnetic plus thermal pressure), ion temperature and the magnetic field are given for three times: for 80 ns corresponding to $R_f(0)/R_f(t) = 2$; for 80 ns, where $R_f(0)/R_f(t) = 24$; and at the time of peak temperature at 81 ns, where $R_f(0)/R_f(t) = 48$. The total pressure remains uniform in space, demonstrating that the implosion is subsonic, i.e. no shock waves are present in the fuel. Notice that the fuel becomes nonuniform already early in the implosion. This phenomenon is due to the generation of a magnetic boundary layer, which will be examined in the next section.

4.4 Magnetic Boundary Layer and Energy Scaling

Figure 4.11 shows radial profiles of density, ion temperature, the magnetic field and fluid velocity in the well-magnetized implosion $\mathcal{B}$ (cf. Table 4.2) at time $t = 260$ ns. At this time, the radial convergence ratio is $C_r = 20$. The most important feature of Fig. 4.11 is the 'magnetic boundary layer' of cold, dense plasma at the fuel-pusher interface, in which the plasma parameters have strong radial gradients. The corresponding region is marked by a vertical shaded band in the figure.

I. Evolution of the Boundary Layer

Figure 4.12 studies the evolution of the boundary layer in several magnetized implosions. The boundary layer is characterized by the following working definition: a mass element

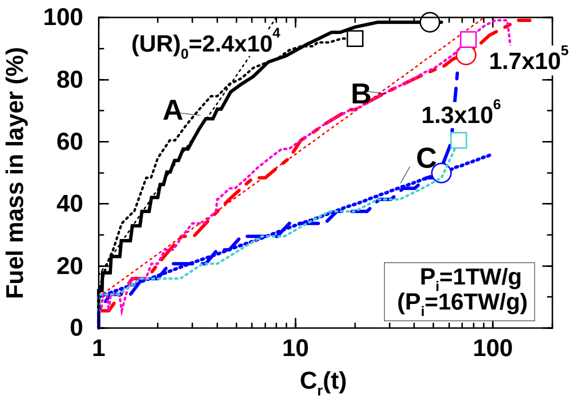

Figure 4.12 Evolution of the boundary layer mass in several magnetized implosions. (Parameters of cases $\mathcal{A}$ and $\mathcal{B}$ are described in Table 4.2.) An additional case $\mathcal{C}$ is characterized by $R_b = 20\,mm$, and fuel parameters equal to those of target $\mathcal{B}$. Plotted is the ratio of the fuel mass in the boundary layer to the total fuel mass vs. radial convergence $C_r(t) \equiv R_f(0)/R_f(t)$. Also given is the $(UR)_0$ parameter of each implosion in units of cm^2/s. Maximum compression is marked by circles. Scaling relations of the form $x_m = g_c \ln C_r(t) + x_{m0}$ for the mass accumulation in the layer are shown as dotted lines. Additionally, results are shown for a second set $(\mathcal{A}^*, \mathcal{B}^*, \mathcal{C}^*)$ of magnetized implosions explained in Sec. 4.4. The $(UR)_0$ values of each target in the second set are the same as those of their counterparts in the first set; but P_i and R_f are scaled simultaneously, keeping the the product $P_i R_f^4$ constant; cf. Sec.4.4 below. Maximum fuel compression in the second set is marked by boxes.

m is part of the boundary layer if its density $\rho(m)$ is twice as large as the minimum density in the fuel volume. Figure 4.12 plots the ratio $x_m = M_{bl}/M_f$ of the amount of fuel mass in the boundary layer M_{bl} to the total fuel mass M_f versus the time-dependent radial convergence ratio $C_r(t) = R_f(0)/R_f(t)$. Results are shown for targets $\mathcal{A}$ and $\mathcal{B}$ (cf. Table 4.2), and an additional target $\mathcal{C}$ with $R_b = 20\,mm$; its parameters are equal to those of target $\mathcal{B}$, except from its initial radius, and a pulse duration t_p scaled according to Eq. (4.3). The main results from Fig. 4.12 can be given in the following two statements

(i) The amount of fuel $x_m(t)$ in the boundary layer evolves with the convergence ratio $C_r(t)$ of an implosion as

$$x_m(t) = g_c \ln C_r(t) + x_{m0} \; , \tag{4.29}$$

where g_c and x_{m0} are constants in each implosion. An important result of the numerical simulations is that the value of g_c depends essentially on the $(UR)_0$ product, and only weakly on the initial fuel density ρ_0 and temperature T_0. This holds as long as the SSMI initial conditions (4.26) for T_0 and $(UR)_0$ are satisfied.

(ii) The slope g_c in Eq. (4.29) scales with $(UR)_0$ as

$$g_c \propto (UR)_0^{-0.35} \; . \tag{4.30}$$

Comparing the amount of cold fuel mass accumulated in the boundary layer in cases $\mathcal{A}$ and $\mathcal{B}$ (see Fig. 4.12) reveals the origin of the difference in the neutron yields, cf. Table 4.2. While the boundary layer in implosion $\mathcal{A}$ has accumulated more than 95 % of the fuel mass up to maximum compression, it is only half of this value in implosion $\mathcal{B}$.

The formation of the boundary layer in magnetized implosions is caused by the radial diffusion of the magnetic field. The ratio

$$\beta = p_{\mathrm{th}}/p_{\mathrm{m}} \tag{4.31}$$

of thermal pressure p_{th} to magnetic pressure $p_{\mathrm{m}} = B^2/8\pi$ in the magnetized fuel drops below unity at large compression. As a consequence, the magnetic field pressure contribution starts to dominate the pusher equation of motion. At the same time, the magnetic field loss enhances the thermal heat conduction losses out of the fuel volume. The reduced fuel temperature, and the enhanced pusher temperature then act back on the diffusion of the magnetic field via the temperature dependence of the electrical conductivity. The full mechanism behind the formation of the boundary layer has, to the author's best knowledge, not been described in the literature yet; the only related article [43] refers to implosions with infinitely thin non-conducting shells, which is not an adequate description of the present situation. The formation of the boundary layer discussed here is also principally different from the so-called 'snowplow' effect in Z-pinch implosions [44]. The main difference lies in the fact that Z-pinch implosions are supersonic, while the ion beam-driven implosions are subsonic in general.

II. Energy Scaling of Magnetized Cold Pusher Implosions

In order to underline the special importance of the $(UR)_0$ parameter for magnetized implosions, an alternative set of implosions $(\mathcal{A}^*, \mathcal{B}^*, \mathcal{C}^*)$ is presented in Fig. 4.12. In the alternative set, each case is characterized by the same values of $(UR)_0$ and initial conditions (ρ_0, T_0, B_0) as the corresponding case in the first set, while specific deposition power P_{i} and beam radius R_{b} differ. They are modified simultaneously according to

$$R_{\mathrm{b}}(\mathcal{A}^*){=}2\,R_{\mathrm{b}}(\mathcal{A}), \quad P_{\mathrm{i}}(\mathcal{A}^*){=}P_{\mathrm{i}}(\mathcal{A})/16\ ,$$

such that the product $P_{\mathrm{i}}\,R_{\mathrm{b}}^4$ remains constant for each pair of sets like $\mathcal{A}$ and $\mathcal{A}^*$. The cases $\mathcal{B}$ and $\mathcal{C}$ are scaled accordingly. As one can see, evolution of the boundary layers in the scaled targets and their counterparts, as seen in Fig. 4.12, is quite similar.

It will now be shown how the scaling parameter $(UR)_0$ is related to the total driver pulse energy E_{b}. First of all, note that equal target proportions are assumed for all targets, given in Table 4.1 above. Therefore, the deposition layer dimensions $R_{\mathrm{p}} < r < R_{\mathrm{b}}$ are fixed by the choice of the ion beam focus R_{b}. Further, the total pulse duration t_{p} of the ion beam is assumed to be consistent with the effective irradiation time $t_{\mathrm{H}} \simeq R_{\mathrm{b}}^{2/3}/P_{\mathrm{i}}^{1/3}$. This is the optimum irradiation time for an ion beam to reach maximum pressure in the deposition layer, cf. Fig. 4.4 and Eq. (4.3). Since the mass of the deposition layer per unit cylinder length scales with R_{b}^2 for fixed target proportions, the total irradiated beam energy E_{b} is given by

$$E_{\mathrm{b}} \propto t_{\mathrm{H}}\,P_{\mathrm{i}}\,R_{\mathrm{b}}^2\ = (P_{\mathrm{i}}\,R_{\mathrm{b}}^4)^{2/3}\ . \tag{4.32}$$

The $(UR)_0$ parameter, on the other hand, can be expressed in terms of beam intensity P_i and beam radius R_b, as well. This is possible since the fraction of beam energy, converted to kinetic energy of the pusher, is approximately independent of the absolute target size (see the remark in Sec. 4.1). One can thus write the implosion velocity as $U \propto \epsilon = \sqrt{P_\mathrm{i} t_\mathrm{H}}$, giving

$$\begin{aligned} (UR)_0 &\propto \sqrt{P_\mathrm{i} t_\mathrm{H}}\, R_\mathrm{b} \\ &\propto (P_\mathrm{i}\, R_\mathrm{b}^{2/3} P_\mathrm{i}^{-1/3})^{1/2}\, R_\mathrm{b} \\ &= (P_\mathrm{i}\, R_\mathrm{b}^4)^{1/3} \ , \end{aligned} \tag{4.33}$$

In combination with Eq. (4.32), Eq. (4.33) leads to

$$E_\mathrm{b} \propto (UR)_0^2 \ . \tag{4.34}$$

Together with the minimum $(UR)_0$ value for the SSMI regime given in Eq. (4.26), this gives a lower bound on the driver pulse energy E_b required for well-magnetized implosions. Using the value given in Eq. (4.26), this energy is

$$E_{\mathrm{b\,min}} = 20 - 40\,\mathrm{kJ/cm} \ , \tag{4.35}$$

depending on the exact fuel parameters. Assuming, for example, that the specific driver power P_i is fixed at a value $P_\mathrm{i} = 1\,\mathrm{TW/g}$ chosen here, the SSMI conditions yield a lower limit on the focal spot radius $R_{\mathrm{b\,min}} \gtrsim 1\,\mathrm{cm}$ of the ion beam, as expected from Fig. 4.8.

The results from these scaling relations are the following statements

- The parameter $(UR)_0$ controlling magnetization is directly related to the external parameter E_b. The quality of the magnetic insulation improves with increasing driver pulse energy E_b, i.e. the more energetic the driver pulse of a magnetized implosion, the less fuel mass ends up in the boundary layer.
- The SSMI conditions set a lower limit on the driver pulse energy for well-magnetized implosions $E_\mathrm{b} \gtrsim 20 - 40\,\mathrm{kJ/cm}$. Below this limit, the magnetic field and the fuel heat diffuse away before the implosion is over.

4.5 Hydrodynamic Stability of the Pusher

Finally, some remarks about the hydrodynamic instability of the cold pusher layer [15]. The Rayleigh-Taylor (R-T) instability occurs in flow patterns where gradients of density and pressure are antiparallel. Two well-known examples are a heavy liquid initially resting on top of a light gas in a gravitation field, and the deceleration of a solid shell by gas of low density. The latter situation occurs in ICF capsule implosions, and also in the cylindrical implosions discussed here.

A central issue in the context of shell implosions is: over which distance can a potentially unstable pusher travel before it is disrupted by R-T instabilities ? – due to the complexity of this subject, only a qualitative answer can be given here on the basis of the one-dimensional simulation results presented above. In a simple linear mode analysis

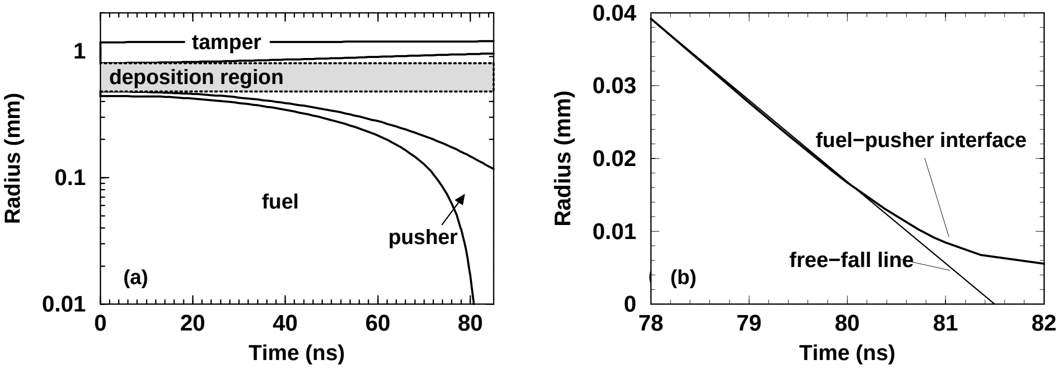

Figure 4.13 Part (a) shows trajectories of the layer boundaries $\mathbf{R_f(t)}$, $\mathbf{R_p(t)}$, $\mathbf{R_b(t)}$ and $\mathbf{R_{tot}(t)}$ vs. time in target $\mathcal{A}$, cf. Table 4.2. The beam deposition region $\mathbf{R_p(0) < r < R_b(0)}$ is marked by a shaded band. Part (b) presents the fuel-pusher boundary immediately before stagnation; the corresponding free-fall line, which assumes no deceleration of the pusher, is marked by a dashed line. Note that the free-fall line reaches the axis $\mathbf{r = 0}$ at a time $\mathbf{t > 81\,ns}$ after the peak temperature is achieved.

of the R-T instability [9, 45] at the interface of two adjacent fluid layers with densities $\rho_1 > \rho_2$, the amplitude η of the mode k grows with time according to

$$\eta \propto e^{\gamma(k)t} \; , \tag{4.36}$$

where the growth rate $\gamma(k)$ is given by

$$\gamma(k) = \sqrt{A_t\, g\, k} \; . \tag{4.37}$$

Here g is the acceleration, and $A_t = (\rho_1 - \rho_2)/(\rho_1 + \rho_2)$ is called Atwood number. During an implosion of a cylindrical shell, there are two regions of instability

(a) The deposition/pusher interface is potentially unstable during the acceleration stage of the pusher. This regime is not critical in the present context.

(b) The fuel/pusher interface becomes unstable during the deceleration stage. This regime of instability is essential for the cylindrical implosions.

The acceleration stage instability of the pusher/deposition interface is not critical here: following Kull [45], a heavy pusher of incompressible gas which accelerates a low-density gas (i.e. $A_t \simeq 1$) should travel $7 - 10$ times its own thickness before it breaks up. Since the pusher aspect ratio $A_r = (R_\mathrm{p}/R_\mathrm{f} - 1)^{-1}$ decreases with time, as seen in Fig. 4.13, and since its initial value has been chosen as 12, cf. Eq. (4.8), the pusher will not break up due to the acceleration instability.

During the deceleration stage, however, the fuel/pusher interface can become R-T unstable. In the worst case, the pusher breaks up and fragments reach the cylinder axis, deteriorating the peak pressure and neutron yield results of the implosion. However, the earliest time at which this can happen is determined by an analysis of the free-fall line shown in Fig. 4.13. The free-fall line is the trajectory of the fuel/pusher interface assuming a constant velocity, i.e. not taking account of the deceleration. The conclusion of this analysis is that the peak fuel temperature can be reached before pusher fragments have reached the axis, cf. Fig. 4.10. Thus, there is hope that the 1D results are not strongly affected by fuel-pusher 'mixing' during the deceleration stage. Additional constraints, which cannot be estimated in the framework of 1D studies, are due to non-uniformities of the ion beam irradiation, and from target fabrication errors. The effect of the magnetic field on instabilities has not been considered in this work.

Figure 4.13 gives only a rough estimate of the time it takes for the heavy shell to penetrate into the central gas during deceleration. More detailed analysis [45] shows that the actual mixing time between heavy pusher and central gas is about a factor 5 smaller than the free-fall time. One can conclude that there is at least a time interval of 5 ns in which the compressed gas in the center exists and can be observed. Moreover, the neutron yield should not be strongly affected by R-T instabilities, since most neutrons are generated long before peak compression, cf. Sec. 4.3.

Chapter 5

Magnetized Fusion Targets

The investigation of magnetized implosions is concluded by applying the results of the previous chapter to magnetized target fusion (MTF) with heavy ion beams. The intention is to present an igniting magnetized implosion, operating at the lowest driver pulse energy possible. A reference case is presented, and the scaling of the ignition threshold of magnetized fusion targets with key parameters is discussed. The reference case is then compared with results of the HIDIF design study [10, 46] for non-magnetized, spherical heavy-ion fusion (HIF) targets.

The central conclusion is that magnetized implosions can achieve ignition conditions at significantly reduced values of implosion velocity, peak driver intensity, as well as relaxed conditions on driver pulse duration and convergence ratios of the implosions. One has to bear in mind, however, that high-gain fusion targets require hot-spot ignition. This means that a burn wave has to propagate along the axis, starting from an ignition sector of the cylindrical target. This chapter describes such an ignition sector.

The present chapter is divided in three parts. Firstly, the ignition threshold of a reference case is determined with respect to the specific driver power, assuming the focal spot radius of the beam to be fixed. Ignition then still depends on a set of three parameters determining fuel temperature, density, and the initial magnetic field in the target prior to implosion. The dependence of ignition on these parameters is studied systematically. Secondly, the ignition and burn stage of magnetized fusion targets is discussed in more detail for a reference case. Thirdly, scaling properties of magnetized targets with the target radius are discussed.

The numerical results presented in this chapter have been obtained by means of the 1D-MHD code DEIRA, including diffusion equations for charged fusion products and nuclear burn equations for the relative abundances of the thermonuclear fuel among other features, cf. Appendix A.

High Gain and Hot-Spot Ignition in Cylindrical Targets

Uniform fuel compression in ICF implosions leads only to low energy gain in spherical *and* cylindrical geometry. For example, it takes about 1.15 MJ to heat 1 mg of DT fuel to the ignition temperature of 10 keV. If implosions had an overall efficiency of 5 %, determined by the driver-fuel coupling efficiency, about 20 MJ of driver energy would be required. Assuming a burn efficiency of 30 %, the thermonuclear energy yield were

100 MJ, corresponding to an overall energy gain of 5. This is not sufficient for fusion energy applications. On the other hand, if the targets could be ignited from a hot spot at one end of a cylindrical target, the energy gain could be enhanced significantly.

Sustained burn in cylindrical fusion targets could be achieved by igniting a short section of the cylinder, which ignites the cold fuel by a burn wave running down the cylinder axis. Note that an axial burn wave is guided by the magnetic field lines along the cylinder axis. In radial direction, on the other hand, it is suppressed due to magnetic insulation. Results of corresponding 2D simulations without axial magnetic field have been published by Avrorin *et al.* [13] and are reproduced in Fig. 1.2 in Chapter 1. With 1D simulations, on which the present work is based, axial burn waves cannot be treated. Here, only the formation of the hot spot is described; the hot spot is now viewed as an axially uniform sector of an extended cylindrical configuration.

5.1 Ignition Threshold

In magnetized implosions, ignition can be defined by comparing the peak fuel temperature reached in a given implosion with that of a corresponding case without thermonuclear reactions. If this ratio is greater than three, the configuration will be called ignited. Such a measure is a well-known ignition criterion, widely used in ICF research [47].

The discussion starts with a brief sketch of the initial configuration and assumptions about the beam-target interaction, which is essentially the same as explained in the previous chapter. Then, some estimates for the initial fuel density, temperature, and the magnetic field guide the design of an igniting reference case. Afterwards, these estimates are verified by systematically studying the dependence of the ignition threshold on initial parameters of fuel and magnetic field.

I. Sketch of Set-Up and Initial Conditions

The initial configuration for the magnetized fusion targets discussed here is essentially the cold pusher configuration introduced in Chapter 4; it is briefly summarized here for reasons of clarity. Figure 5.1 shows a schematic view of the set-up, consisting of a metallic tube filled with deuterium-tritium (DT) fuel gas at low density. The tube material is gold. Prior to implosion, an axial magnetic field B is introduced into the target. For the magnetic insulation to work, and in order to reach fusion temperatures at peak compression, the fuel also has to be heated to temperatures of at least 50 eV, as will be explained below. The heat could be brought into the fuel from outside, e.g. by axially incident laser beams. This is essentially the scheme of injected entropy, as proposed by Caruso *et al.* recently [14].

The beam heating, characterized by the specific deposition power P_i (TW/g), is assumed to be uniform throughout the deposition region, i.e. over an annular region

$$R_\mathrm{p} < r < R_\mathrm{b} \ , \tag{5.1}$$

where R_p and R_b are fixed values given in Table 5.1. The outer radius R_b of the focal spot is assumed to be $R_\mathrm{b} = 3.0\,\mathrm{mm}$ in this section, corresponding to the focal spot size of the HIDIF driver for the non-magnetized target discussed below. Relative proportions

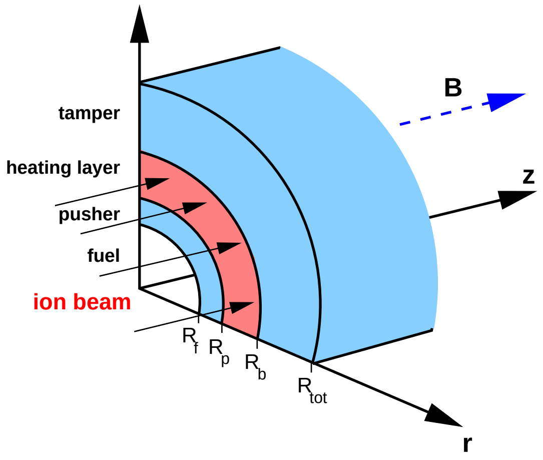

Figure 5.1 **Schematic view of a cylindrical fusion target. The ion beam driving the implosion is indicated by arrows from the left; it heats the liner in the annular region $R_p < r < R_b$, and drives the implosion in the radial direction. A magnetic field B, directed along the target axis, is introduced into the target before the implosion starts. The fuel gas is assumed to be a DT mixture. Note that the target proportions in the figure are not to scale. The values used in the simulations are given in Table 5.1.**

of the cylindrical fusion targets are equal to those of the targets discussed in the previous chapter, i.e. the ratios $R_\mathrm{p}/R_\mathrm{b}$ etc. are the same. This particular choice aims at optimum conversion efficiency between driver pulse and kinetic energy of the imploding pusher, cf. Chapter 4. Further, the pulse duration t_p is assumed to be consistent with the target radius, as explained in Chapter 4. The optimum pulse duration can be calculated from the focal spot radius R_b of the ion beam and the specific driver power P_i according to Eq. (4.3), i.e.

$$t_\mathrm{H} = \left(R_\mathrm{b}^2/P_\mathrm{i}\right)^{1/3} \; . \tag{5.2}$$

II. Ignition Threshold in Terms of Specific Driver Power

Once a value of R_b –denoting the focal spot radius of the ion beam– is chosen, the target geometry is determined and the remaining free beam/target parameters are initial fuel density ρ_0, temperature T_0, the initial magnetic field B_0, and the specific driver power P_i. These parameters are now determined on the basis of a simple estimate and checked later by simulations. The choice of the beam focus in a consistent target set-up immediately determines the heated mass $M_h \simeq \pi\,(R_\mathrm{b}^2 - R_\mathrm{p}^2)\rho_\mathrm{h}$ per unit cylinder length. Together with Eq. (5.2), the specific driver power P_i is related to the beam energy via

$$E_\mathrm{b} \simeq t_\mathrm{H}\, P_\mathrm{i}\, M_\mathrm{h} \; . \tag{5.3}$$

For 1 mg/cm of DT fuel in the target, one needs about 20 MJ/cm of driver energy, following the argument about the energy gain of uniform implosions given above. The

#	$\mathbf{R_f}$	$\mathbf{R_p}$	$\mathbf{R_b}$	$\mathbf{R_{tot}}$	$\mathbf{T_0}$	$\mathbf{B_0}$	ρ_0
Case A	**1.65**	**1.8**	**3.0**	**4.5**	**300 eV**	**50 T**	$\mathbf{1\times 10^{-2}\,g/cm^3}$
Case B	**2.75**	**3.0**	**5.0**	**7.5**	**300 eV**	**70 T**	$\mathbf{3\times 10^{-3}\,g/cm^3}$

Table 5.1 Initial parameters for magnetized fusion targets. Case A is discussed in Sec. 5.1, while case B is considered in Sec. 5.3. Given are the fuel radius $\mathbf{R_f}$ (in units of mm), the outer pusher boundary radius $\mathbf{R_p}$, the focal spot radius $\mathbf{R_b}$ of ion beam, and the total target radius $\mathbf{R_{tot}}$. The ion beam is irradiated in the annular region $\mathbf{R_p < r < R_b}$; see also Fig. 5.1. Also given are the initial fuel temperature $\mathbf{T_0}$ and the initial value of the magnetic field $\mathbf{B_0}$ in the target.

resulting specific driver power P_i is then given by

$$P_\mathrm{i} \simeq E_\mathrm{b}\, {t_\mathrm{H}}^{-1}\, M_h^{-1} \propto E_\mathrm{b}^{3/2}\, {R_\mathrm{b}}^{-4} \approx 100 - 200\,\mathrm{TW/g}\ . \tag{5.4}$$

Due to the low implosion velocities that correspond to such driver parameters ($U \lesssim 10^7$cm/s), no strong shock heating occurs during implosions [48]. Therefore, the fuel heating in magnetized implosions can be determined in the approximation of a quasi-adiabatic compression, in the best case. (In general, finite losses cannot be avoided). This approximation (see Sec. 4.2) assumes that fuel density ρ, temperature T and the magnetic field B scale with the radial convergence ratio $C_r(t) \equiv R_\mathrm{f}(0)/R_\mathrm{f}(t)$ as

$$\rho \propto {C_r}^2,\ \ T \propto {C_r}^{4/3},\ \ B \propto {C_r}^2\ . \tag{5.5}$$

In order to reach ignition temperatures of $5-10$ keV in such implosions, the fuel needs to have $T_0 = 100-200$ eV initially, assuming radial convergence ratios $C_r = 20-30$ at peak compression. Such values have been obtained experimentally, in cylindrical implosions driven by high explosives [49]. To reach the fuel magnetization $BR \gtrsim 6\times 10^5$ G cm= 60 T cm required for ignition,[a] see Chapter 2), the initial magnetic field B_0 needs to be about $B_0 \gtrsim 20-30$ T under the same assumptions about C_r as above.

Figure 5.2 demonstrates how the ignition threshold of magnetized implosions is determined numerically for fixed values of $T_0 = 300$ eV and $B_0 = 70$ T. For each combination of P_i and ρ_0, two simulations are carried out: one with fusion reactions, one without fusion reactions. The ratio of the resulting peak fuel temperatures is plotted versus the driver power P_i for three values of the initial fuel density ρ_0. Only if the peak temperature ratio is greater than three, the fuel is called ignited. The resulting curves connecting implosions with equal values of ρ_0 are called 'ignition curves'.

Similar to the magnetized implosions discussed in Chapter 4, the initial fuel density has to be optimized numerically for each set of parameters B_0, T_0. The reason for the existence of an optimum fuel density resembles that given in the previous chapter. However, there are differences, namely that (i) the present case includes also thermonuclear burn, so that the neutron yield depends even more sensitively on the fuel density (note that for smaller ρ_0, there is less fuel material per unit length in the cylinder), and (ii) the convergence ratios are now strongly affected by the choice of the fuel density,

---

[a] While Chapter 2 uses cgs units, here the more 'practical' unit Tesla is chosen.

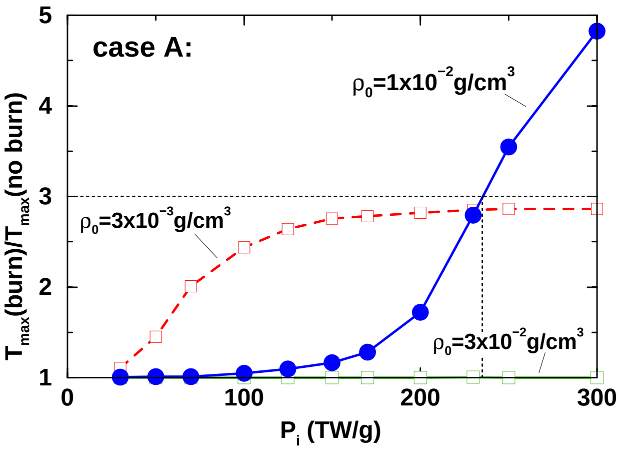

Figure 5.2 Ignition curves for Case A (cf. Table 5.1). Plotted is the ratio of peak fuel temperature results with fusion reactions to results without fusion reactions vs. specific driver power P$_\mathrm{i}$. Three ignition curves for different values of the initial fuel density ρ_0 are shown, while the fuel initial conditions T$_0 = 300\,$eV and B$_0 = 50\,$T are kept fixed. Ignition has occurred if the ignition ratio defined above exceeds a factor of three. This limit is marked by a horizontal dotted line.

since the fuel pressure is now significantly larger compared to the implosions discussed in Chapter 4.

III. Dependence of the Ignition Threshold on Initial Parameters

To verify the estimates used for the choice of initial parameters for case A in the previous section, the initial fuel density ρ_0, temperature T_0 and the magnetic field B_0 are now varied systematically. The corresponding numerical results are presented in Fig. 5.3. Each combination of T_0, B_0 and ρ_0 in the range

$$\begin{aligned} 30\,\mathrm{eV} \lesssim & \quad T_0 \quad \lesssim 1000\,\mathrm{eV} \\ 5\,\mathrm{T} \lesssim & \quad B_0 \quad \lesssim 200\,\mathrm{T} \\ 1\times10^{-4}\,\mathrm{g/cm^3} \lesssim & \quad \rho_0 \quad \lesssim 1\times10^{-2}\,\mathrm{g/cm^3} \end{aligned} \tag{5.6}$$

is checked for ignition and marked by a symbol in a T_0, B_0 plane. Full symbols represent ignition, while empty symbols correspond to cases ignition did not occur. For all implosions presented in Fig. 5.3, target size and driver power are kept constant at $R_\mathrm{b} = 3.0\,\mathrm{mm}$ and $P_\mathrm{i} = 230\,\mathrm{TW/g}$ respectively. The ion pulse is assumed to heat the target up to the moment of stagnation.

The first observation in Fig. 5.3 is that ignition occurs only in a narrow region of the T_0, B_0 parameter space. The limits of this 'ignition island' are mainly set by the conditions for well-magnetized implosions (SSMI), see Chapter 4, and by magnetic pressure. Initial configurations with $B_0 \lesssim 20\,\mathrm{T}$ or $T_0 \lesssim 20\,\mathrm{eV}$ will not meet the SSMI requirements, i.e. heat diffuses rapidly out of the fuel. For too large values of $B_0 > B_{0\mathrm{max}} \propto T^{0.75}$, on

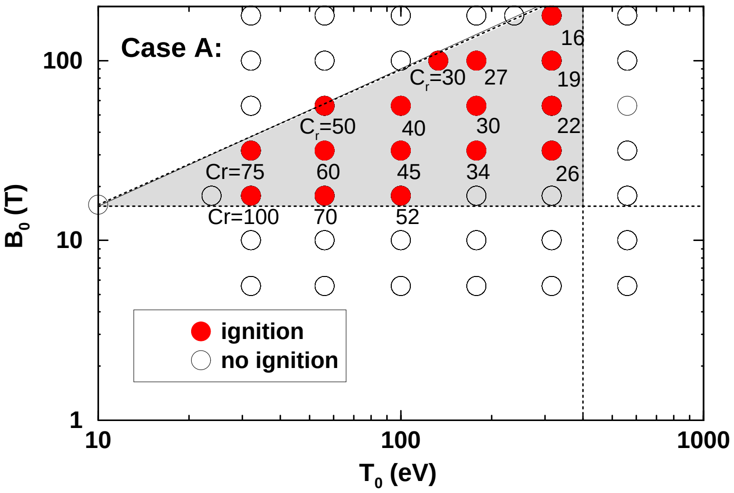

Figure 5.3 Igniting (full circles) and non-igniting (open circles) cases in the plane spanned by the initial fuel temperature T_0 and the magnetic field B_0 for fixed values of $R_b = 3.0\,\mathrm{mm}$ and $P_i = 230\,\mathrm{TW/g}$, and optimized values ρ_0. The maximum convergence ratios C_r of the implosions are given as numbers below the symbols.

the other hand, ignition will not occur as the implosion is stopped by magnetic pressure (see Sec. 4.3). Note that the ignition island is also bounded towards large initial temperatures, for the following reason: as T_0 is increased, the fuel compression, and therefore also the maximum fuel ρR decrease. As a consequence, final yield and peak temperature drop slightly. At the same time, the peak fuel temperatures in the reference implosions (without burn) increase with growing T_0, causing the ignition ratio to drop below three.

Figure 5.3 also presents the maximum convergence ratios C_r for each igniting configuration, taken at the largest density $\rho_{0\mathrm{m}}$ for which ignition still occurs. The C_r values decrease from extremely large values ($C_r = 100$), as found in implosions with $B_0 = 20\,\mathrm{T}$ and $T_0 = 30\,\mathrm{eV}$, down to $C_r \simeq 16$ for $B_0 = 200\,\mathrm{T}$ and $T_0 = 300\,\mathrm{eV}$. In addition to the limits of the ignition island as seen in Fig. 5.3, the radial convergence ratios C_r provide a means to select acceptable implosion parameter combinations B_0 and T_0. For example, in order to reduce the effect of R-T instabilities during an implosion (cf. Chapter 4), one might restrict oneself to convergence ratios $C_r \lesssim 30$; see Sec. 4.5.

It turns out that the largest density $\rho_{0\mathrm{m}}$ for which ignition still occurs at given values of T_0, B_0, grows with T_0. At the same time, the convergence ratios C_r decrease, as seen in Fig. 5.3. This is connected with the ignition conditions for thermonuclear fusion, i.e. the minimum fuel temperature and ρR that have to be achieved at peak compression. Going from an igniting case to a larger initial temperature, the compression drops and so does the final ρR. This has to be compensated by a larger initial fuel density. The sensitivity of ignition with respect to the initial fuel density ρ_0 it is also reflected by the ignition curves shown in Fig. 5.2. In order to make sure that the survey shown in Fig. 5.3 is complete, a wide range of initial value for ρ_0 needs to be covered. It is therefore essential that none of the cases in the survey is at the interval borders for ρ_0 as defined in Eq. (5.6).

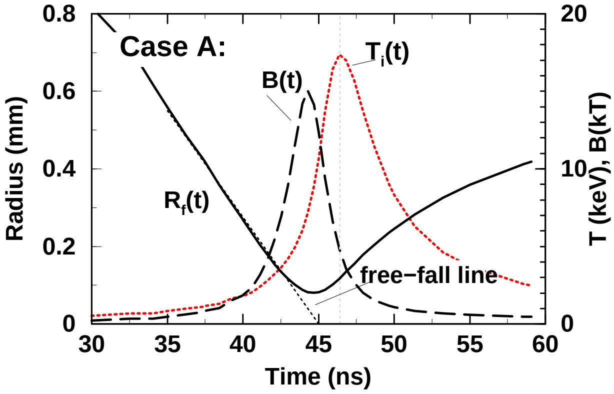

Figure 5.4 Evolution of fuel parameters in case A. Shown are the radial position of the fuel-pusher boundary $\mathbf{R_f(t)}$ (left scale), fuel ion temperature $\mathbf{T_i}$, and the magnetic field B on the axis (right scale) vs. time. Additionally, the free-fall line of the fuel-pusher interface is marked by a dotted line.

5.2 Ignition and Burn

The igniting magnetized implosion case A introduced in the previous section will now be discussed in more detail and compared with a non-magnetized, spherical ICF capsule. A reference case has been defined in the HIDIF (Heavy Ion Driven Inertial Fusion) study [10, 46], a comprehensive design study of indirectly driven, non-magnetized ICF capsules in spherical geometry. The underlying indirect-drive approach to ICF [9] assumes that small DT pellets ($R \approx 1\,\mathrm{mm}$) are placed in metal cavities which are heated by external drivers. The capsule implosions are then driven by thermal x-rays from the hohlraum walls. Due to the stronger compression in spherical implosions, as compared to the cylindrical ones, the peak fuel densities in such capsules exceed those in cylindrical implosions significantly; therefore, burn is much faster. Additionally, hot-spot ignition with radial burn waves propagating into cold fuel brings the energy gain up to large values $G \simeq 100$ [10].

I. Reference Case A in Detail

In order to present characteristic features of an igniting magnetized implosion, Fig. 5.4 shows the evolution of the average fuel temperature and magnetic field on the target axis. In addition, it presents the free-fall line for this implosion, which characterizes the time ($t \simeq 45\,\mathrm{ns}$) when instabilities can reach the cylinder axis, in the worst case. This plot is, in principle, similar to Fig. 4.13 that describes the implosion of a magnetized target at $P_\mathrm{i} = 1\,\mathrm{TW/g}$. The distinct feature of the present implosion, however, is that the fuel temperature is raised –due to DT fusion reactions– by a factor of three, in comparison to an implosion without burn (cf. Fig. 5.2). As a consequence, the fuel temperature in implosion A is still growing when the free-fall line reaches the axis; this is not the case in the magnetized implosion $\mathcal{A}$ of the previous chapter. However, the stability of the pusher during the formation of the hot spot in magnetized implosions is not discussed here.

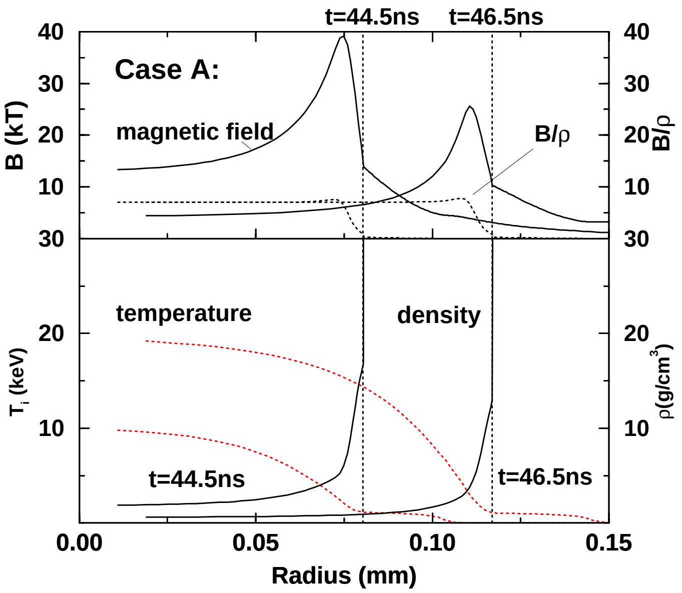

Figure 5.5 Profiles of ion temperature, density and magnetic field in implosion A for two times, corresponding to peak compression (t = 44.5 ns) and peak fuel temperature (t = 46.5 ns). The position of the fuel-pusher interface at these times is indicated by dotted vertical lines. Additionally, the ratio B/ρ is plotted in the upper diagram.

Figure 5.5 shows radial profiles of temperature and density in implosion A at the time of peak compression ($t = 44.5\,\text{ns}$) and at peak fuel temperature ($t = 46.5\,\text{ns}$). Notice the gradients in fuel density, temperature and magnetic field, as discussed in Sec. 4.4, which are characteristic for the magnetic boundary layer (cf. Fig. 4.11). At ignition, about $40-50\,\%$ of the fuel are contained in the boundary layer and, therefore, cannot contribute to the burn. Figure 5.5 also presents the radial dependence of the quantity B/ρ. In a quasi-adiabatic implosion with a fully frozen-in magnetic field, this quantity is uniform in space and time. Here, it remains constant throughout the main part of the fuel volume and drops only in the magnetic boundary layer.

II. Comparison with a Spherical Fusion Capsule

Table 5.2 compares the reference case A of a magnetized fusion target with results of the HIDIF study [10,46], corresponding to an indirectly-driven fusion capsule in a hohlraum cavity heated by ion beams. The value for the specific driver power P_i in this case corresponds to a peak value and the pulse duration given here is the time scale of one sub-pulse (see Fig. 3 of Ref. [10]). The strong time-dependence of the ion pulses necessary in indirect-drive ICF makes great demands on the performance of accelerators. It is, however, needed in order to obtain optimum implosion results in terms of the fuel density, temperature distributions required for hot-spot ignition. For the directly driven cylindrical targets discussed here, on the other hand, the beam pulses of the heavy ions are assumed to be uniform in space and time. From the target physics point of view, the

Case	R_b	E_b	t_p	P_i(max)	U	$(\rho R)_m$	C_r	ϕ_b	G
HIDIF	**3 mm**	**5 MJ**	**10 ns**	10^4 **TW/g**	3×10^7	**2.75**	**30**	**35 %**	**90**
MTF	**3 mm**	**1 MJ/mm**	**30 ns**	**230 TW/g**	5×10^6	**0.01**	**20**	**2.8 %**	**1**

Table 5.2 Comparison between the magnetized cylindrical target A and HIDIF results [10]. Given are the following quantities: pulse energy E_b, driver focal spot radius R_b, pulse duration t_p, peak specific driver power P_i, implosion velocity U (in cm/s), peak fuel ρR value $(\rho R)_m$ (in g/cm^2), maximum radial convergence ratio C_r, burn fraction ϕ_b and the gain G. Note that the gain of the cylindrical target A refers only to the ignition section discussed here.

distinct feature of the magnetized implosion lies in (i) the lower implosion velocity and (ii) lower fuel ρR at maximum compression. Regarding the implosion results in terms of gain G and burn fraction ϕ_b, one has to be aware of the fact that the magnetized target represents only an ignition section of a longer cylindrical target. High gain can be reached only with hot-spot ignition, as discussed above.

5.3 Scaling Properties

Having found the ignition threshold for one particular value of the target size $R_b = 3.0\,\mathrm{mm}$ in the previous section, it revealing to study the dependence of ignition on this parameter. Here, an alternative case B is presented with $R_b = 5.0\,\mathrm{mm}$. Similar to the previous section, some initial estimates about the target parameters are made and then verified by means of simulations. Regarding the driver power required for ignition, one can now take the ignition threshold $P_i = 230\,\mathrm{TW/g}$ found for case A, and scale it such that the resulting driver pulse energy E_b is approximately the same in both cases. The appropriate scaling procedure has been discussed in the previous chapter, cf. Eqs (4.32)–(4.34). The main result of that analysis has been that the energy E_b is related to the driver power P_i and the focal spot radius R_b via

$$E_b \propto (P_i\, R_b^4)^{2/3} \; . \tag{5.7}$$

For the present case, this means that the driver power in case B has to be

$$P_i(\text{case B}) = \left(\frac{3}{5}\right)^4 P_i(\text{case A}) \simeq 30\,\mathrm{TW/g} \; . \tag{5.8}$$

Using similar initial fuel parameters (T_0, B_0) to those chosen in the previous case A, Fig. 5.6 now shows simulation results that check the ignition threshold of case B. The main conclusions of Fig. 5.6 are that (i) the ignition threshold of case B is approximately $P_i \simeq 30\,\mathrm{TW/g}$, as predicted on the basis of the scaling (5.8), and (ii) that the corresponding value of the initial fuel density ρ_0 is smaller than that for case A.

The dependence of ignition on the choice of initial parameters T_0 and B_0 is characterized in Fig. 5.6. Analogously to Fig. 5.3, it gives the initial parameters for which case B ignites. One can see that the ignition island for the case B is significantly smaller in the

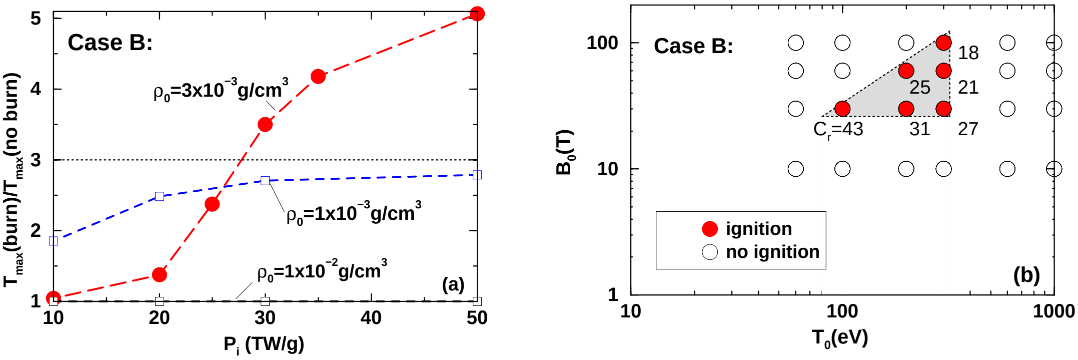

Figure 5.6 (a) Ignition curves for target B, cf. Table 5.3 and the caption of Fig. 5.2. (b) 'Ignition island' for case B. Shown are igniting and non-igniting implosions in a plane of initial implosion parameters, cf. the caption of Fig. 5.3.

MTF	R_b	E_b	t_p	P_i^{max}	U	$(\rho R)_m$	T_m	ϕ_b
Case A	3 mm	1 MJ/mm	30 ns	230 TW/g	5×10^6	0.01	18 keV	2.8 %
Case B	5 mm	1.8 MJ/mm	75 ns	30 TW/g	3×10^6	0.012	19 keV	2.5 %

Table 5.3 Comparison of the two scaled magnetized fusion targets A and B. Given are pulse energy E_b, driver focal spot radius R_b, pulse duration t_p, peak specific driver power P_i, implosion velocity U (in cm/s), peak fuel ρR (in g/cm^2), the peak fuel temperature T_m and the burn fraction ϕ_b. The corresponding convergence ratios can be taken from Figs 5.3 and 5.6.

parametric T_0, B_0 plane, and that the fuel density values for which ignition occurs are generally smaller than in case A, as mentioned earlier.

The scaling that leads from case A to case B has also another important consequence, namely that the $(UR)_0$ parameter is the same in both implosions. This follows from the relation

$$(UR)_0 \propto (P_i R_b^4)^{1/3} \propto E_b^{1/2} \; , \tag{5.9}$$

compare Eq. (4.34). The value of the $(UR)_0$ product of the implosions discussed here is given in Fig. 5.7. The figure discusses the growth of the magnetic boundary layer in the respective implosions. It presents the mass fraction of fuel in the cold boundary layer in implosions A and B. In order to compare their evolution with the self-sustained magnetized implosions presented in Sec. 4.4, this figure includes the the magnetized targets $\mathcal{A}$ and $\mathcal{B}$, cf. also Fig. 4.12. Similar to the magnetized implosions discussed earlier, the boundary layer evolution of cases A and B agrees well.

Following the scaling relation (5.9) for the $(UR)_0$ product, one could –in principle– design targets for fixed driver energy, but with extremely large pulse durations and correspondingly low driver intensities. These targets would become very large, see Eq. (5.7). However, the results presented here indicate that the ignition island in the B_0, T_0 parametric plane shrinks for decreasing driver intensity, and finally vanishes. This sets a lower limit for the possible driver intensity. In addition to that, the range of fuel densities ρ_0

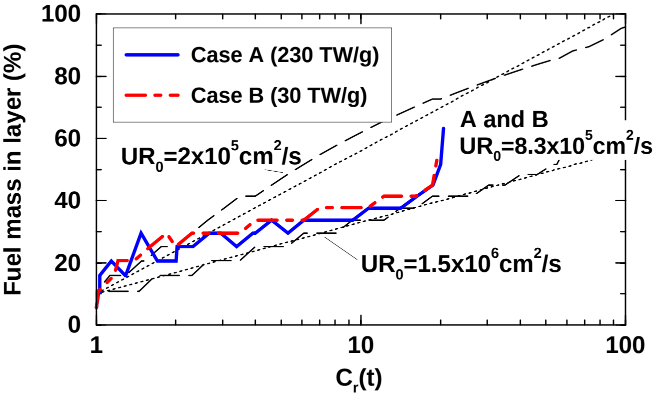

Figure 5.7 **Evolution of the boundary layer in the magnetized fusion targets A and B, cf. Table 5.3. Plotted is the ratio of the fuel mass in the boundary layer to the total fuel mass vs. radial convergence $C_r(t) \equiv R_f(0)/R_f(t)$. For comparison, two additional plots for the implosions $\mathcal{B}$ and $\mathcal{C}$, from Chapter 4, are included. The corresponding $(UR)_0$ values are given next to the plots.**

for which ignition occurs shifts to smaller values with decreasing driver intensities P_i. As a consequence, the fusion yield would become decrease. This will affect the propagation of the burn wave in axial direction, which is required for hot-spot ignition.

Chapter 6

Self-Similar Description of Imploding Hollow Shells

This chapter deviates from the main line of the the present work in that it deals with a fundamental aspect of implosions on the basis of a highly idealized model. It analyzes the stagnation pressure of converging flows, given general material properties such as the implosion velocity v_{imp}, pressure p_0 and entropy measured by the parameter $\alpha_{\mathrm{if}} \propto p_0/\rho_0^{\gamma}$. The analysis is based on pure gas dynamics of a polytropic gas with adiabatic exponent γ and so-called similarity solutions of the gas dynamic equations discussed below.

Of course, the stagnation pressure or, equivalently, maximum energy density of the imploding material directly relates to the basic topic of this thesis, and the analytic results of this chapter help to understand general features of magnetized target fusion. However, the particular interest in this topic came up during the course of this work triggered by recent work of Herrmann *et al.* [17], investigating ignition energy E_{ign} scaling of spherical implosions of fusion capsules. These authors have extracted the scaling relation

$$E_{\mathrm{ign}} \propto \alpha_{\mathrm{if}}^{1.88\pm0.05}\, p_0^{-0.77\pm0.03}\, v_{\mathrm{imp}}^{-5.89\pm0.12} \qquad (6.1)$$

from a large number of implosion simulations.[a] A striking observation made by Atzeni *et al.* [18] was that this important relation can be determined directly from simple model considerations, invoking the isobaric ignition model [30] and the self-similar stagnation pressure discussed in this chapter.

The isobaric ignition model postulates the pressure-radius product of the stagnating fuel

$$p_{\mathrm{s}} R_{\mathrm{s}} \propto \rho_{\mathrm{s}} R_{\mathrm{s}} T_{\mathrm{s}} = \mathrm{const} \qquad (6.2)$$

to be an ignition constant set by DT fusion physics, which requires certain values for the ignition temperature $T_{\mathrm{s}} \gtrsim 10\,\mathrm{keV}$ and $\rho_{\mathrm{s}} R_{\mathrm{s}} \gtrsim 0.2\,\mathrm{g/cm^2}$ (to stop 3.51 MeV alpha particles inside the hot spot) [9]. This leads to

$$E_{\mathrm{ign}} \propto p_{\mathrm{s}} R_{\mathrm{s}}^3 \propto (p_{\mathrm{s}} R_{\mathrm{s}})^3/p_{\mathrm{s}}^2 \propto p_{\mathrm{s}}^{-2}\ . \qquad (6.3)$$

---

[a] A similar scaling, also based on simulations, has been proposed recently by Saillard [50].

The second ingredient is provided by self-similar imploding shells [16] which give

$$p_\mathrm{s}/p_0 \propto M_0^3 \tag{6.4}$$

for the stagnation pressure of spherically imploding hollow shells; here $M_0 = v_\mathrm{imp}/c_0$ is the Mach number and c_0 the sound velocity of the shell material. Using in addition $\alpha_\mathrm{if} \propto p_0/\rho_0^{5/3}$ for a $\gamma = 5/3$ gas, one easily converts Eqs (6.2)–(6.4) into

$$E_\mathrm{ign} \propto p_0^{-2}\, M_0^{-6} \propto \alpha_\mathrm{if}^{1.8}\, p_0^{-0.8}\, v_\mathrm{imp}^{-6}\ . \tag{6.5}$$

The intriguing coincidence of Eqs (6.1) and (6.5) calls for a deeper analysis of the stagnation pressure scaling, Eq. (6.4), which had been found numerically in Ref. [16]. In the present work it is derived analytically in a general form, i.e. for plane, cylindrical and spherical implosions and arbitrary adiabatic exponents [19].

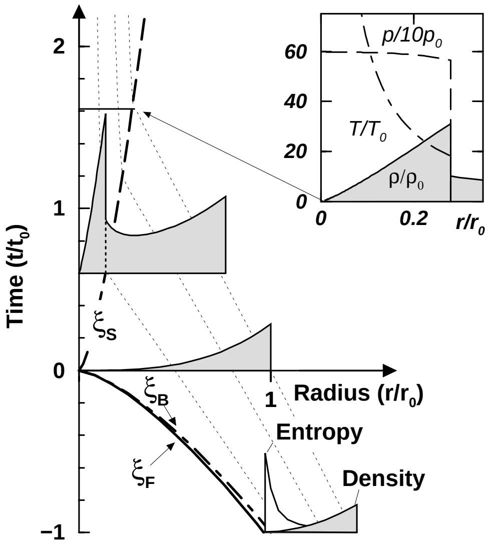

Figure 6.1 Self-similar solution of spherically imploding shell in $\mathbf{r, t}$ diagram for $\alpha = 0.7$, $\kappa = 3$, $\gamma = 5/3$. Inner surface of shell ($\xi_\mathrm{F} = 0.96$) and trajectory of reflected shock ($\xi_\mathrm{S} = 0.198$) are represented by thick $\xi = \mathrm{r}/\mathrm{t}^\alpha$ lines. The $\mathrm{t} = 0$ axis corresponds to $\xi = \infty$. Fluid elements move on dotted trajectories with almost constant velocity. Inserts show density profiles at different times; also shown are entropy at $\mathrm{t}/\mathrm{t}_0 = -1$ as well as pressure and temperature distributions at $\mathrm{t}/\mathrm{t}_0 = 1.6$. Normalization is such that sonic point B is at $\xi_\mathrm{B} = \mathrm{r}_0/\mathrm{t}_0^\alpha = 1$ and ρ_0, T_0, p_0 refer to the fluid element at $\mathrm{r} = \mathrm{r}_0$ and $\mathrm{t} = \mathrm{t}_0$; it is considered as an outer boundary.

The self-similar description of converging flows is based on the assumption that interfaces, like shock waves or material boundaries, move along trajectories

$$R(t) = \xi\, |t|^\alpha\ . \tag{6.6}$$

This concept leads to the so-called similarity coordinate $\xi = r/|t|^\alpha$, where r and t are now interpreted as spatial coordinate and time. The basic assumption here is that flow functions like pressure and density depend mainly on ξ. Figure 6.1 shows a particular example for such a self-similar flow pattern. It describes the implosion of a hollow spherical shell in a radius-time diagram. Inserts illustrate self-similar density profiles close to the time of void closure at $t = 0$ (the latter means that the hollow region inside the shell disappears). This figure is presented here to give a first flavor of the hollow shell implosions; it will be explained below.

The discussion of the stagnation pressure scaling in self-similar implosions of hollow shells, which is the main issue of the present chapter, is organized in two steps. Section 6.1 introduces the basic equations and mathematical tools used for the similarity analysis. Sec. 6.2 presents the central approximation, which is then applied to derive the stagnation pressure scaling (6.4) in a general form analytically.

6.1 Self-Similar Solution of the Equations of Gas Dynamics

I. Self-Similar Ansatz

The basic equations of gas dynamics for one spatial coordinate r can be written in the form [51]

$$\begin{aligned} \partial_t\rho + \partial_r(\rho u) + (n-1)\rho u/r &= 0 \quad \text{(mass conservation)} \\ \partial_t u + u\,\partial_r u + (1/\rho)\,\partial_r p &= 0 \quad \text{(momentum balance)} \\ \partial_t(p/\rho^\gamma) + u\,\partial_r(p/\rho^\gamma) &= 0 \quad \text{(entropy equation)}\ . \end{aligned} \tag{6.7}$$

Here the parameter n refers to plane ($n = 1$), cylindrical ($n = 2$) or spherical ($n = 3$) geometry, while γ is the adiabatic exponent. An ideal gas equation of state is used with $p = \rho c^2/\gamma$, where c denotes the local sound velocity; the entropy p/ρ^γ of each fluid element is conserved, except across shock boundaries.

The similarity ansatz for the fields of flow velocity $u(r,t)$, sound velocity $c(r,t)$, and density $\rho(r,t)$ is chosen in the form [16]

$$\begin{aligned} u(r,t) &= (\alpha\, r/t)\, U(\xi) \\ c(r,t) &= (\alpha\, r/t)\, C(\xi) \\ \rho(r,t) &= r^\kappa\, G(\xi)\ , \end{aligned} \tag{6.8}$$

where the similarity coordinate ξ is defined by

$$\xi = r/\mid t\mid^\alpha\ . \tag{6.9}$$

Note that radial coordinates r and times t are given in units r_0, t_0 and velocities are given in r_0/t_0. As a result of the above construction, the similarity coordinate ξ and the reduced functions $U(\xi)$, $C(\xi)$, $G(\xi)$ are invariants with respect to scale transformations of time, radius, and mass [52]. The corresponding scaling group [53] contains the two exponents α and κ as free parameters.

Ansatz (6.8) has some immediate consequences. It implies that, at the time of void closure $t = 0$, corresponding to $\xi = \infty$, all flow functions can be represented by power laws

$$\begin{aligned} &u(r,t=0) = u_0 r^{-\lambda},\ c(r,t=0) = c_0 r^{-\lambda}, \\ &\rho(r,t=0) = \rho_0 r^{\kappa},\ A(r,t=0) = A_0 r^{-\epsilon}\ , \end{aligned} \tag{6.10}$$

provided that the limits for $t \to 0$ exist. The constants u_0, c_0, ρ_0, A_0 are obtained from Eq. (6.8) with $|t| = (r/\xi)^{1/\alpha}$ in the limit $\xi \to \infty$. Often-used combinations of the basic parameters (n, γ, α, κ) are given here for reference

$$\begin{aligned} &\lambda = 1/\alpha - 1,\ \epsilon = \kappa(\gamma - 1) + 2\lambda,\ \mu = 2/(\gamma - 1)\ , \\ &\beta = n - \mu\lambda,\ \nu = n\gamma + \kappa - 2\lambda,\ \Gamma = (\gamma + 1)/(\gamma - 1)\ . \end{aligned} \tag{6.11}$$

The entropy distribution at void closure is determined by an exponent ϵ. For values $\epsilon > 0$, it diverges in the centre. This behavior resembles that of ICF fuel close to stagnation; see Ref. [16] for a discussion of this point. However, in approaches including e.g. heat transport among other loss mechanisms, the entropy divergence in the centre is prevented by corresponding diffusive heat losses out of the shell.

Another important consequence of ansatz (6.8) is that the value of the Mach number $M_0 \equiv u_0/c_0$ at void closure does not depend on the mass coordinate.

II. Particle Trajectories and Characteristics

Figure 6.2 discusses the radius-time phase plane of self-similar converging flows, showing a particle trajectory, several ξ-lines, and a characteristic line (=characteristic) for a self-similar flow in the r, t diagram.

- Trajectories of gas elements a can be represented by curves $R(a, t)$ in a space-time plot, where the Lagrangean coordinate $a \equiv R(a, t_0)$ labels each gas particle by its position $R(a, t_0)$ at a fixed time t_0.
- Lines of constant ξ, or ξ-lines, emerge from $r = t = 0$. In some important cases, they coincide with material interfaces, like the inner surface of a hollow shell or a shock fronts.
- Particle trajectories $R(a, t)$ can be expressed in terms of the similarity coordinate ξ. The corresponding derivative $dR(a, \xi)/d\xi$ along ξ-lines can be evaluated as follows. On the one hand, the derivative of $\xi = R/|t|^\alpha$ with respect to R yields the expression

  $$\frac{d \ln \xi}{d \ln R} = 1 - \frac{d \ln |t|^\alpha}{d \ln R}\ . \tag{6.12}$$

  On the other hand, the second expression on the right-hand side of Eq. (6.12) is equal to the reduced particle velocity $U(\xi)$, since, by definition, one has $dR(t)/dt = \alpha R\, |t|^\alpha\, U(\xi)$. This yields

  $$\frac{d \ln R}{d \ln \xi} = \frac{U(\xi)}{U(\xi) - 1}\ . \tag{6.13}$$

  Expression (6.13) is important for understanding why the particle trajectories shown in Fig. 6.1 are almost straight lines; this will be explained below.

  Note that $R(a, \xi)$ is interpreted now as a function of ξ, and time t is obtained from $|t| = (R(a, \xi)/\xi)^{1/\alpha}$. It follows immediately from Eq. (6.13) that

  $$U = 1 \tag{6.14}$$

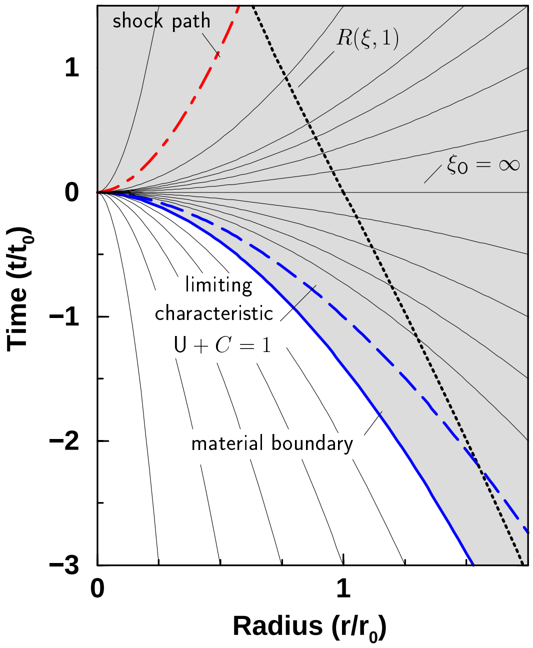

Figure 6.2 The r, t plane schematically displaying various important curves. The thin solid curves are lines of constant ξ. In some important cases, ξ-lines coincide with material boundaries, shock paths, or characteristics. Also shown is an example for a particle trajectory $\mathbf{R}(\xi, \mathbf{a} = \mathbf{1})$.

is the condition for a particle trajectory to coincide with a ξ-line. Self-similar motion of a free surface is therefore described by $U = 1$.

Integrating Eq. (6.13) between any two ξ_1 and ξ_2 for a given particle a, one finds that the ratios $R(a, \xi_2)/R(a, \xi_1)$ of particle positions do not depend on which particle is considered; such ratios are the same for all mass elements a. This important observation holds also for the ratios of density, pressure, and other physical quantities.

- Characteristics, denoted as $R^{\pm}(a, t)$, can be used to describe the propagation of small perturbations, i.e. sound waves. Their trajectories are defined by

$$dR^{\pm}/dt = u(R^{\pm}, t) \pm c(R^{\pm}, t) \ . \tag{6.15}$$

In terms of the self-similar coordinates, this relation writes

$$\frac{d \ln R^{\pm}}{d \ln \xi} = \frac{U \pm C}{U \pm C - 1} \ , \tag{6.16}$$

after applying the same transformation as to Eq. (6.13). For this reason, characteristics $R^{\pm}(a, t)$ coincide with ξ-lines exactly if the condition

$$U \pm C = 1 \tag{6.17}$$

is fulfilled. These so-called limiting characteristics play an important role with respect to causality in the flow. They divide regions which are in causal contact with the gas at $r = t = 0$ from those which are not. Figure 6.2 shows an example of a limiting characteristic in a convergent flow.

III. Reduced Differential Equation

With a self-similar ansatz (6.8), the three basic equations of gas dynamics (6.7) reduce to two ordinary differential equations [16]

$$\begin{aligned} a_1 dU + b_1 dC + d_1 d\ln\xi &= 0 \\ a_2 dU + b_2 dC + d_2 d\ln\xi &= 0 \end{aligned} \tag{6.18}$$

with coefficients

$$\begin{aligned} &a_1 = C/\mu \ , \quad a_2 = U - 1 \ , \\ &b_1 = U - 1 \ , \quad b_2 = \mu C \ , \\ &d_1 = C[U(1 + n/\mu) - 1/\alpha] \ , \\ &d_2 = U(U - 1/\alpha) + C^2[\mu + (\kappa + \mu\lambda)/(\gamma(1 - U))] \ . \end{aligned} \tag{6.19}$$

The remarkable feature of this reduction, first noticed by Guderley [54], is that the coefficients (6.19) are independent of the space-time variables r, t and ξ; instead, they depend solely on the reduced velocities U, C and on the free parameters n, γ, α, κ. The problem therefore reduces to one ordinary differential equation

$$\frac{dU}{dC} = \frac{\Delta_1(U(C), C)}{\Delta_2(U(C), C)} \ . \tag{6.20}$$

Integration of Eq. (6.20) gives solutions of the form $U(C)$. Then, U and C can be expressed in terms of ξ by quadrature of

$$\frac{d\ln\xi}{dC} = \frac{\Delta_0(U(C), C)}{\Delta_2(U(C), C)} \ . \tag{6.21}$$

Here, the determinants Δ_i of system (6.18) are defined by

$$\Delta_0 = a_1 b_2 - b_1 a_2 \ , \ \Delta_1 = b_1 d_2 - d_1 b_2 \ , \ \Delta_2 = d_1 a_2 - a_1 d_2 \ . \tag{6.22}$$

Figure 6.3 shows a numerical solution of Eq. (6.20) in the U, C plane. The positions of the singular points (given below), but not the structure of the solution curve, depend exclusively on the particular values of the free parameters n, γ, α, κ [16]. A unique feature of the present class of solutions is that the description covers times before and after void closure; the solution curves (see Fig. 6.3) consist of two distinct branches in different domains of the U, C plane, separated by the point O at $U = C = 0$. While the upper branch in the $U > 0$ half-plane corresponds to times $t < 0$ before void closure, the lower branch refers to times $t > 0$.

Each point in Fig. 6.3 refers to a distinct singularity in Eq. (6.20); in these singular points, both determinants vanish simultaneously

$$\Delta_1(U, C) = 0 \ , \ \Delta_2(U, C) = 0 \ . \tag{6.23}$$

There are many different ways to satisfy Eq. (6.23). Some important choices are listed for example in Ref. [16]. For the description of hollow shell implosions, one needs only four of these singular points, characterized in the following.

- Point O is located at $U_0 = C_0 = 0$; it connects both branches of the solution curve for $t < 0$ and for $t > 0$, and refers to void closure at time $t = 0$, corresponding to $\xi \to \infty$. Additionally, point O describes the flow for $r \to \infty$ at times $t \neq 0$. The absolute values of the slope $|dU/dC|$ for $U > 0$ and for $U < 0$ are equal, and correspond to the Mach number $M_0 = |U/C|$ at void closure.

- Points B and D are both located on the sonic line $U + C = 1$, where $\Delta_0(U, C) = 0$. They correspond to the two limiting characteristics before and after void closure, respectively. The physical solution curves in the U, C plane which connect flow regions $U + C > 1$ with $U + C < 1$, have to cross the sonic line through B or D. The position of these points is given by the quadratic equation

  $$(n-1)\gamma\, U_{\mathrm{B,\,D}}^2 + [\kappa - 2\lambda - \gamma(n-1-\lambda)]\, U_{\mathrm{B,\,D}} - (\kappa - 2\lambda) = 0 \ . \qquad (6.24)$$

  The solution of Eq. (6.24) yields $U_{\mathrm{B,\,D}}$ and $C_{\mathrm{B,\,D}} \equiv 1 - U_{\mathrm{B,\,D}}$. Crossing the sonic line at other points than B or D would lead to double valued, non-physical solutions. Since the shock, that travels through the shell after void closure, is faster than sound waves, only singular point B is relevant for the present solution. It guarantees the existence of solutions for a continuous set of α and κ values. Point B is of great significance in the present context, because it determines the Mach number M_0 of the imploding shell as a function of the free parameters. This relationship is fixed by Eq. (6.24). The position of point B also provides the initial values for integrating differential equation (6.20).

- Point E is located at $U_{\mathrm{E}} < 0$, and $C_{\mathrm{E}} = \infty$. It refers to a central explosion with diverging temperature at the origin. In the present context, it describes the stagnated gas after the reflected shock has passed. Remarkably, this state can be derived analytically from Eqs (6.20) and (6.21). The state of the gas behind the reflected shock is described by the separatrix running toward point E at

  $$U_{\mathrm{E}} = -(\kappa - 2\lambda)/n\gamma, \quad C_E \to \infty \ , \qquad (6.25)$$

  where $\xi_{\mathrm{E}} = 0$. The explicit solution for the flow functions after stagnation, valid asymptotically for $r \to 0$ and $t > 0$, is given by

  $$\begin{array}{rcl} u(r,t) & = & -\alpha(\kappa - 2\lambda)/(n\gamma)\, r\, t^{-1} \\ \rho(r,t) & \propto & r^{n\epsilon/\nu}\, t^{\alpha(\kappa - n\epsilon/\nu)} \\ p(r,t) & \propto & r^0\, t^{\alpha(\kappa - 2\lambda)} \ , \end{array} \qquad (6.26)$$

  with $\nu = n\gamma + \kappa - 2\lambda$. For $\epsilon > 0$, the density vanishes in the centre, while the temperature $T \propto c^2$ diverges such that the pressure $p \propto \rho T$ is uniform. In the special case $\kappa = 2\lambda$, these asymptotic results hold even globally; then they describe an isobaric gas at rest. In this case, the solution branch $\mathrm{S_2E}$ coincides with the $U = 0$ axis in Fig. 6.3.

- Point F is located at $U_{\mathrm{F}} = +1$ and $C_{\mathrm{F}} = \infty$. In this point, the condition (6.14) for a trajectory to coincide with a ξ-line is fulfilled. This means that there are neighboring particle trajectories only on one side of the trajectory $R_{\mathrm{F}}(t)$. Since this is possible only for entropy parameters $\epsilon > 0$ [16], point F refers to the inner material boundary of non-isentropic imploding hollow shells.

It is important to note that the imploding shell solution presented here is almost identical with the imploding shock wave solution first discussed by Guderley [54]. In both cases, the $t < 0$ branch has to cross the sonic line $C = 1 - U$ at singular point B. For Guderley's converging shock in a uniform gas, where $\kappa = 0$, the solution has to satisfy strong shock conditions at the inner boundary. This means that it has to hit the strong shock point A at

$$U_{\mathrm{A}} = 2/(\gamma+1), \quad C_{\mathrm{A}} = \sqrt{2\gamma(\gamma-1)}/(\gamma+1) \ , \tag{6.27}$$

as shown in Fig. 6.3. This singles out a unique value of α. On the other hand, the imploding shell solutions considered here have to reach the inner surface point F at $U_{\mathrm{F}} = 1$ and $C_{\mathrm{F}} = \infty$, which is possible for a continuous set of α and κ values. Figure 6.3 also shows the shock points S_1 and S_2. They correspond to one characteristic $R_{\mathrm{s}} = \xi_{\mathrm{s}}\, t^{\alpha}$, describing the reflected shock after void closure.

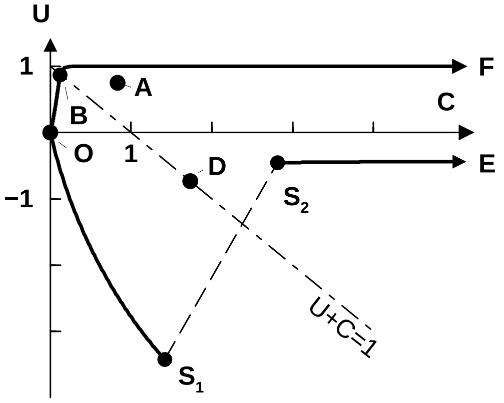

Figure 6.3 Self-similar solution of Fig. 6.1 in U, C plane. The points O, B, D, and also E, F located at C → ∞ represent singular points, where dU/dC → 0/0. The solid curve OBF corresponds to the imploding shell, and curve $\mathbf{OS_1S_2E}$ to the gas after void closure (t > 0); they match at point O where $\xi = r/|t|^{\alpha} = \infty$, which describes the solution at t = 0 and also outer gas layers at r → ∞ for $|t| \neq 0$. The jump $\mathbf{S_1S_2}$ describes the reflected shock at ξ_s and $\mathbf{S_2E}$ refers to the stagnating gas at $0 \le \xi \le \xi_s$. Physical solutions have to cross the dash-dotted line U + C = 1 at the sonic point B.

IV. Shock Jump Conditions

After void closure, the imploding shell material stagnates behind the reflected shock. In the U, C plane, this corresponds to a jump between the points S_1 and S_2; the value of

ξ does not vary across the shock. The locations of the shock points S_1 and S_2 in the U, C plane are related by the Hugoniot relations, expressing the conservation of mass, momentum and energy across shock discontinuities. In the frame of reference of the moving discontinuity, they can be written [51]

$$\begin{aligned} [\rho_1 u_1]_{1,2} &= 0 \\ [p_1 + \rho_1 u_1^2]_{1,2} &= 0 \\ [w_1 + u_1^2/2]_{1,2} &= 0 \;. \end{aligned} \tag{6.28}$$

Here $[q]_{1,2}$ denotes the jump of the quantity q between the undisturbed region 1 in front of the shock and region 2 behind the shock wave. The heat function of the gas is given by $w \equiv c^2/(\gamma - 1)$.

In order to write the Eqs (6.28) in terms of U and C, one has to transform velocities from shock- to the laboratory system according to

$$u_{\mathrm{s}} = u_{\mathrm{l}} - d \;, \tag{6.29}$$

where d is the shock front velocity. Since the shock propagates on a ξ-line, its trajectory can be written as $d(r,t) = (\alpha r/t) D(\xi_{\mathrm{s}})$, with a reduced velocity $D = 1$. Mass conservation across the shock then assumes the form

$$\rho_{\mathrm{s}}/\rho_1 = G_2/G_1 = (1 - U_1)/(1 - U_2) \tag{6.30}$$

with the reduced density G, while momentum and energy conservation lead to the expressions

$$\begin{aligned} (1 - U_2) &= (1 - U_1) \left[\frac{\gamma - 1}{\gamma + 1} + \frac{2}{\gamma + 1} \left(\frac{C_1}{1 - U_1} \right)^2 \right] \;, \\ C_2^2 &= \frac{2\gamma(\gamma - 1)}{(\gamma + 1)^2} (1 - U_1)^2 \\ &\quad + \left[1 - 2 \left(\frac{\gamma - 1}{\gamma + 1} \right)^2 - 2 \frac{\gamma - 1}{(\gamma + 1)^2} \left(\frac{C_1}{1 - U_1} \right)^2 \right] C_1^2 \;. \end{aligned} \tag{6.31}$$

These equations can be found as the solutions of quadratic equations, emerging from the conservation relations (6.28). Noting that large Mach numbers $M_1 = U_1/C_1$ in front of the shock imply also large values of $(1 - U_1)/C_1$, the jump conditions for density reduces to

$$\rho_{\mathrm{s}}/\rho_1 \simeq \Gamma, \tag{6.32}$$

where $\Gamma = (\gamma + 1)/(\gamma - 1)$. Furthermore, the pressure jump over the shock $S_R = p_{\mathrm{s}}/p_1$

can be approximated by

$$\begin{aligned}
S_R &= \frac{\rho_\mathrm{s}}{\rho_1}\frac{C_2^2}{C_1^2} \\
&= \left\{ \frac{2\gamma(\gamma-1)}{(\gamma+1)^2}\frac{(1-U_1)^2}{C_1^2} + \right. \\
&\quad \left. + \left[1 - 2\left(\frac{\gamma-1}{\gamma+1}\right)^2 - 2\frac{\gamma-1}{(\gamma+1)^2}\left(\frac{C_1}{1-U_1}\right)^2 \right] \right\} \frac{1-U_1}{1-U_2} \\
&\simeq \frac{2\gamma}{\gamma+1}\left(\frac{1-U_1}{C_1}\right)^2 .
\end{aligned} \tag{6.33}$$

6.2 Analytical Calculation of the Shell Compression

Figure 6.4 shows results from the numerical integration of the reduced differential equation (6.20). Presented are the stagnation pressure ratio p_s/p_0 and the final compression ρ_s/ρ_0 versus Mach number M_0 at void closure. It makes sense to consider these ratios because, as shown above, they are unique throughout the shell, i.e. their value is independent of the mass coordinate. The dots correspond to a set of α and κ values chosen to cover the range $2 < M_0 < 25$ and $0.3 < \epsilon < 6$. For spherical shells ($n = 3$) of an ideal $\gamma = 5/3$ gas, the results are well represented by the scaling relations $p_\mathrm{s}/p_0 \simeq 3.6\, M_0^3$ and $\rho_\mathrm{s}/\rho_0 \simeq 2.4\, M_0^{3/2}$ for pressure and density, while $p_\mathrm{s}/p_0 \propto M_0^{9/4}$ and $\rho_\mathrm{s}/\rho_0 \propto M_0^{3/4}$ in cylindrical geometry ($n = 2$). Numerically [16], it turns out that results for different values of the entropy parameter ϵ, at fixed values of the Mach number M_0, are almost identical. In other words, the final compression ratios depend strongly on the Mach number of the imploding shell, but they are rather independent of the entropy distribution. This remarkable result will be derived analytically below.

The line of the argument goes as follows. Determinants Δ_i of the reduced differential equation are decomposed into terms L_i and R_i. Whenever it is necessary for the present approximation, one has $R_i \ll L_i$, as will be shown. This has two consequences. Firstly, adiabatic compression of the shell material between void closure and the time when the reflected shock passes can be expressed analytically. This is closely related to the fact that particle trajectories, plotted in Fig. 6.1, are almost straight lines. Secondly, it is possible to give an analytic expression for the Mach number M_0 at void closure. The combination of both steps leads to an analytic expression for the shell compression.

I. Reduction of the Determinants

The determinants Δ_i for the reduced differential equation (6.20) and (6.21) can be written as a sum of two expressions L_i and R_i, so that the differential equations (6.20) take on the form

$$\frac{dU}{dC} = \frac{\Delta_1}{\Delta_2} \equiv \frac{L_1 + R_1}{L_2 + R_2} , \tag{6.34}$$

$$\frac{d\ln\xi}{dC} = \frac{\Delta_0}{\Delta_2} \equiv \frac{L_0 + R_0}{L_2 + R_2} . \tag{6.35}$$

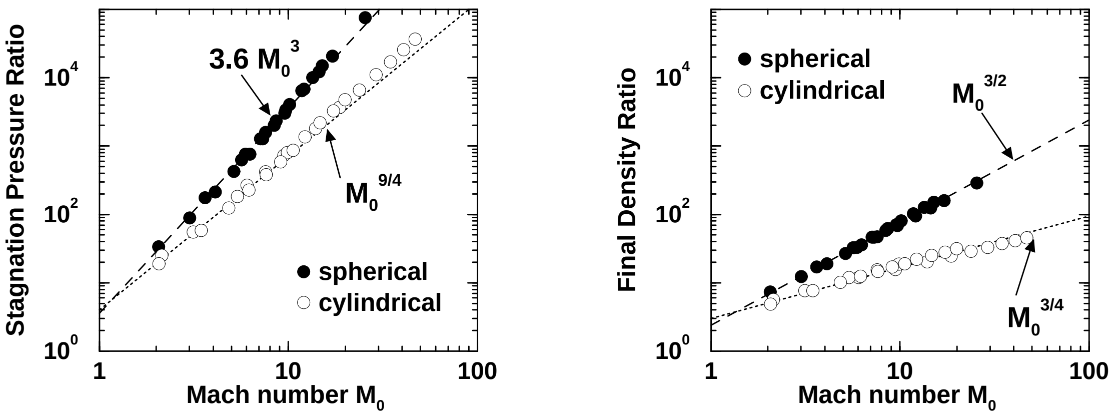

Figure 6.4 Compression ratios p_s/p_0 and ρ_s/ρ_0 of fluid elements between times of void closure (index 0) and passage of reflected shock (index s) plotted vs. Mach number M_0. Dots represent numerical solutions of the similarity model and lines refer to analytical scaling formulas (open dots correspond to cylindrical, full dots to spherical geometry). The small scatter of the results around the power laws reflects different values of the entropy parameter ϵ.

The expressions L_i and the rest terms R_i are given by

$$\begin{aligned}
&L_0 = -(1-U)^2 \ , \quad R_0 = C^2 \ , \\
&L_1 = U(1-U)\,(1/\alpha - U) \ , \quad R_1 = -C^2\left[nU + (\kappa - 2\lambda)/\gamma\right] \ , \\
&L_2 = C\left\{(1-U)\,(1/\alpha - U) + U\left[1/\alpha - U - n(1-U)\right]/\mu\right\} \ , \\
&R_2 = C^3\left[(2\gamma/\epsilon)^{-1}(U-1)^{-1} - 1\right] \ .
\end{aligned} \tag{6.36}$$

The approximation, which is the main result of this chapter, assumes that the Mach number at void closure is large

$$\lim_{\xi\to\infty}\left|\frac{U}{C}\right| \gg 1 \ , \tag{6.37}$$

and that the shell material is almost at rest behind the reflected shock,

$$|U_{\rm E}| \equiv |(\kappa - 2\lambda)/(n\gamma)| \ll 1 \ , \tag{6.38}$$

and that $\lambda \ll 1$. Here, $U_{\rm E}$ has been defined in Eq. (6.26). This choice of parameters corresponds to an almost isobaric steady gas behind the reflected shock, which is a typical situation for ICF capsule implosions [30]. The last two conditions further yield $\epsilon/2\gamma \simeq \lambda \ll 1$.

With the assumptions (6.37) and (6.38) in mind, one finds that

$$R_1 \ll L_1 \ , \ R_2 \ll L_2 \tag{6.39}$$

along the branch BOS of the solution curve, and

$$R_0 \ll L_0 \ , \ R_2 \ll L_2 \tag{6.40}$$

along branch BO, as will be shown below. Neglecting the small terms R_i, one can integrate Eqs (6.34) and (6.35) analytically along the respective branches. This yields the desired results for (i) the adiabatic compression of the shell after void closure, and for (ii) the relation between the Mach numbers at void closure and in the sonic point B.

Ignoring the terms R_i in Eq. (6.34) leads to

$$\frac{dU}{dC} \simeq \frac{L_1}{L_2} = \frac{U(1-U)(1/\alpha - U)}{C\left\{(1-U)(1/\alpha - U) + U\left[(1/\alpha - U) - n(1-U)\right]/\mu\right\}} \ , \tag{6.41}$$

where $\lambda = 1/\alpha - 1$ is used. Then Eq. (6.34) can be written as

$$\frac{d\ln C}{dU} \simeq \frac{1}{U} + \frac{1/\mu}{1-U} - \frac{n/\mu}{1/\alpha - U} \ . \tag{6.42}$$

For the last equation to hold one needs $|dU/dC| \neq 0$; this condition is fulfilled in the solution branch BOS_1, as long as $\alpha < 1$ and $U < 1$. Equation (6.42) can be integrated directly, leading to the following expression for the Mach number

$$M \cong M_0 \left[\frac{1-U}{(1-\alpha U)^n}\right]^{1/\mu} \ . \tag{6.43}$$

Eq. (6.43) can be used, firstly, to relate the analytic expression for the Mach number M_{B} in the sonic point, cf. Eq. (6.24), with the Mach number M_0 at void closure. Secondly, Eq. (6.43) allows to determine adiabatic compression of the shell material between void closure and passage of the reflected shock.

II. Analysis of the Reduction

This section checks the approximations (6.39) and (6.40) at three characteristic points of the relevant solution branch BOS_1. First the shock point S_1 in the lower half plane $U < 0$ of the solution space with $|U| \gg 1$ is considered. Here one can write

$$\begin{aligned} \frac{|L_0|}{|R_0|} &\simeq \left(\frac{U}{C}\right)^2 \gg 1 \ , \\ \frac{|L_1|}{|R_1|} &\simeq \frac{|U|^3}{nUC^2} = \frac{1}{n}\left(\frac{U}{C}\right)^2 \gg 1 \ , \\ \frac{|L_2|}{|R_2|} &\simeq \frac{CU^2[1-(n-1)/\mu]}{C^3} = [1-(n-1)/\mu]\left(\frac{U}{C}\right)^2 \gg 1 \ , \end{aligned} \tag{6.44}$$

demonstrating that approximation (6.39) is valid in the close to point S_1. Near void closure, one has $0 < C \ll |U| \ll 1$. Therefore

$$\begin{aligned} |L_0|/|R_0| &\simeq \frac{1}{C^2} \gg 1 \ , \\ |L_1|/|R_1| &\simeq \frac{U/\alpha}{nC^2(U-U_{\mathrm{E}})} \gg 1 \ , \\ |L_2|/|R_2| &\simeq \frac{C/\alpha}{C^3(-\epsilon/(2\gamma)-1)} \gg 1 \ , \end{aligned} \tag{6.45}$$

showing that the approximation works close to point O, as well.

The position of singular point B is characterized as the solution of the quadratic equation (6.24) in the $U > 0$ half plane. Using $\lambda \equiv 1/\alpha - 1$, one obtains

$$\begin{aligned} U_{\mathrm{B}} &\simeq 1 \; , \\ 1 - U_{\mathrm{B}} &\simeq \frac{\lambda/n}{1 - U_{\mathrm{E}}} \; , \\ 1 - \alpha U_{\mathrm{B}} &\simeq \lambda/(\lambda + 1) \; , \end{aligned} \tag{6.46}$$

where $U_{\mathrm{E}} = -(\kappa - 2\lambda)/(n\gamma)$ denotes the position of singular point E, and $C_{\mathrm{B}} \equiv 1 - U_{\mathrm{B}}$. At point B, the expressions L_i, R_i can be approximated by

$$\begin{aligned} \frac{|L_0|}{|R_0|} &= 1 \; , \\ \frac{|L_1|}{|R_1|} &\simeq \frac{(\lambda/n)(1 - U_{\mathrm{E}})^{-1}\lambda/(\lambda+1)}{[(1 - U_{\mathrm{E}})n/\lambda]^{-2} n (1 - U_{\mathrm{E}})} \simeq \frac{1}{\lambda + 1} \simeq 1 \; , \\ \frac{|L_2|}{|R_2|} &\simeq \frac{(1 - U_{\mathrm{B}})\{(1 - U_{\mathrm{B}})(1/\alpha - U_{\mathrm{B}}) + U_{\mathrm{B}}\,[1/\alpha - U_{\mathrm{B}} - n(1 - U_{\mathrm{B}})]/\mu\}}{(1 - U_{\mathrm{B}})^3[\lambda(1 - U_{\mathrm{B}})^{-1} - 1]} \\ &\simeq \frac{(\lambda^2/n)(1 - U_{\mathrm{E}})^{-1}\,\{(\lambda/n) - U_{\mathrm{E}}/(1 - U_{\mathrm{E}})\,\mu^{-1}\}}{(\lambda/n)^3(1 - U_{\mathrm{E}})^{-3}[n(1 - U_{\mathrm{E}}) - 1]} \\ &\approx n/(n-1) \; . \end{aligned} \tag{6.47}$$

In the sonic point B, the approximation $L_i \gg R_i$ is obviously invalid. Nevertheless, approximation (6.43) for the Mach number M_0 in point B gives reliable results, for the following reason: examining the relative change of the Mach number between the points O and B, it turns out that the derivative $|M^{-1}dM/dU|$, calculated from the approximate solution (6.43), drops to small values in the vicinity of point B. Under the assumptions (6.39) and (6.40) given above, one has

$$\begin{aligned} \left(\frac{1}{M}\frac{dM}{dU}\right)_{U \simeq U_{\mathrm{B}}} &= \frac{1}{\mu}\left[\frac{-1}{1 - U_{\mathrm{B}}} + \frac{\alpha n}{1 - \alpha U_{\mathrm{B}}}\right] \\ &\simeq \frac{n}{\lambda\mu}\,[(U_{\mathrm{E}} - 1) + 1] \\ &= \frac{n}{\lambda\mu} U_{\mathrm{E}} \approx \frac{1}{\mu\lambda} \ll 1 \; , \end{aligned} \tag{6.48}$$

for appropriate combinations of κ and λ. Note that the solution works even when $U_{\mathrm{E}} \neq 0$.

While the above argument is carried out for the approximate solution (6.43), it applies also to the full expressions for the Mach number

$$\frac{1}{M}\frac{dM}{dU} = \frac{1}{U}\left[1 - M\frac{dC}{dU}\right] \; . \tag{6.49}$$

Since the expressions L_1 and R_1 in the denominator of the term dC/dU have equal signs, the full expression for dM/dU is of the same order of magnitude as its approximated counterpart (6.48). Finally, note that, after shock passage, i.e. at S_2 and the branch $\mathrm{S}_2\mathrm{E}$, one has $U/C \ll 1$.

III. Shell Compression after Void Closure

The compression of shell material between void closure and the passage of the reflected shock can be divided into two steps. In the first step, the converging shell material is compressed adiabatically between void closure and the reflected shock. This compression occurs even in the plane geometry ($n = 1$), where it is caused by the homologous flow pattern for $\alpha < 1$, cf. Eq. (6.54) below. In the second step, the gas is further compressed as it passes through the reflected shock. The combination of both steps yields the final compression of the shell material.

(1) Adiabatic Compression. The compression of fluid elements between void closure and the time before the reflected shock passes is given by $\rho \propto c^{\mu}$; this results from Poisson´s adiabatic relation $\rho \propto p^{1/\gamma} \propto (c^2\rho)^{1/\gamma}$, with $\gamma \equiv 1 + 2/\mu$. It is important to note that fluid elements move at almost constant velocity between void closure and the passage of the reflected shock, i.e.

$$du/d\ln\xi \simeq 0 \ . \tag{6.50}$$

This can be seen from the following argument. Consider the particle trajectory $R(a, \xi)$ of the mass element a, written in terms of ξ. The particle velocity $u = dR/dt$ can be expressed as

$$u(a, \xi) = \alpha\, R(a, \xi)^{1-1/\alpha}\, \xi^{1/\alpha}\, U(\xi) \ . \tag{6.51}$$

Using Eq. (6.13) derived above, one arrives at

$$\begin{aligned} \frac{du}{d\xi} &\propto \left[(1 - 1/\alpha)\,\frac{d\ln R}{d\ln\xi} + \frac{1}{\alpha} + \frac{d\ln U}{d\ln\xi}\right] \\ &= \left[\frac{1/\alpha - U}{1 - U} + \frac{d\ln U}{d\ln\xi}\right] \ . \end{aligned} \tag{6.52}$$

Invoking the main assumption $U/C \gg 1$ and using the definitions of expressions L_i given in Eq. (6.36), one can write the last term in the square bracket as

$$\frac{d\ln U}{d\ln\xi} = \frac{1}{U}\,\frac{\Delta_1(U, C)}{\Delta_0(U, C)} \simeq \frac{L_1}{L_0} = \frac{U - 1/\alpha}{1 - U} \ . \tag{6.53}$$

This yields the desired result (6.50), and it explains why the particle trajectories in Fig. 6.1 are almost straight lines. As a consequence, the sound velocity c is proportional to M^{-1} along each particle trajectory between void closure and passage of the reflected shock. Together with the approximate integral (6.43) for the Mach number, this yields an expression for the adiabatic compression,

$$\frac{\rho_1}{\rho_0} \cong \frac{(1 - \alpha U_1)^n}{1 - U_1} \cong \alpha^n (1 - U_1)^{n-1} \ . \tag{6.54}$$

The last approximation in Eq. (6.54) holds for values of $\lambda \ll 1$, and $|U| \gg 1$. Under these conditions one can approximate $1 - \alpha U$ by $\alpha(1 - U)$.

(2) Shock Compression. In the reflected shock, the shell material is further compressed by a factor $\rho_s/\rho_1 \simeq \Gamma$. Using jump condition (6.32) across the shock to write $1 - U_1$, the total compression between void closure and passage of the reflected shock takes on the form

$$\frac{\rho_\mathrm{s}}{\rho_0} = \frac{\rho_\mathrm{s}}{\rho_1}\frac{\rho_1}{\rho_0} \cong (\alpha\Gamma)^n (1-U_2)^{n-1} \ . \tag{6.55}$$

Similarly, the pressure ratio between void closure and passage of the reflected shock can be split up into an adiabatic contribution $p_1/p_0 = (\rho_1/\rho_0)^\gamma$, and the strong shock contribution (6.33). Combining these relations with Eq. (6.32) for the density ratio, and expressing $C_1 = U_1/M_1$ via Eq. (6.43), one obtains

$$\frac{p_\mathrm{s}}{p_0} \cong \frac{2\gamma}{\gamma-1}\frac{(1-U_2)^{n+1}}{[1-\Gamma(1-U_2)]^2}\,(\alpha\Gamma)^n\,M_0^2. \tag{6.56}$$

This expression holds for $n = 1, 2, 3$, corresponding to plane, cylindrical and spherical geometry, as will be shown below.

IV. Mach Number at Void Closure

The next step is to eliminate the expressions $1-U_2$ from Eqs (6.55)–(6.56), and to replace them by expressions in the Mach number M_0. This is done as follows: the solution curve $U(C)$ has to cross the sonic line $U + C = 1$ through singular point B in the $U > 0$ half-plane, as shown in Fig. 6.3. The Mach number M_B in point B is found by solving quadratic equation (6.24). Substituting expressions (6.46) for U_B in the approximate integral (6.43) for the Mach number, one obtains the desired expression for the Mach number in terms of the reduced velocity $1 - U_2$

$$M_0 \cong (\alpha\lambda)^{n/\mu}\,(n/\lambda)^{1+1/\mu}\,(1-U_2)^{1+1/\mu} \ . \tag{6.57}$$

V. Analytic Expressions for the Final Compression

Now, expression (6.57) for the reduced velocity $1 - U_2$ is inserted into relations (6.55)–(6.56) for the shell compression. The density ratio (6.55) then assumes the final form

$$\rho_\mathrm{s}/\rho_0 \cong f(\alpha)\,M_0^{2(n-1)/(\gamma+1)} \ , \tag{6.58}$$

with a pre-factor $f(\alpha) = \Gamma^n n^{1-n}\alpha(1-\alpha)^{(1-n/\Gamma)(n-1)}$. For typical cases with $n < \Gamma$, the factor $f(\alpha)$ depends only weakly on α and can be replaced by a constant in the relevant range of $0.6 < \alpha < 0.9$, see Fig. 6.5. This corresponds to M_0 and ϵ values covered in Fig. 6.4. For spherical geometry, $n = 3$, and an adiabatic exponent $\gamma = 5/3$ one obtains $f_\mathrm{max} \cong 2.7$, while $2(n-1)/(\gamma+1) = 3/2$. This is in good agreement with the numerical results shown in Fig. 6.4.

The pressure ratio (6.56) is not immediately of power law structure in $x \equiv 1 - U_2$, but approximating the function $F(x) \equiv x^{n+1}/(1-\Gamma x)^2$ by the power law $F(x) \approx F_1 x^\sigma$ at $x = 1$, one finds $\sigma = n - \gamma$ and $F_1 = (\gamma-1)^2/4$. This leads to

$$p_\mathrm{s}/p_0 \cong g(\alpha) M_0^{2(n+1)/(\gamma+1)}. \tag{6.59}$$

For $n = 3$ and $\gamma = 5/3$, Eq. (6.59) reproduces the central scaling relation $p_\mathrm{s}/p_0 \propto M_0^3$. Again, the front factor $g(\alpha) = \gamma(\gamma-1)\Gamma^n n^{\gamma-n}\alpha^\gamma(1-\alpha)^{(1-n/\Gamma)(n-\gamma)}/2$ is a weak function

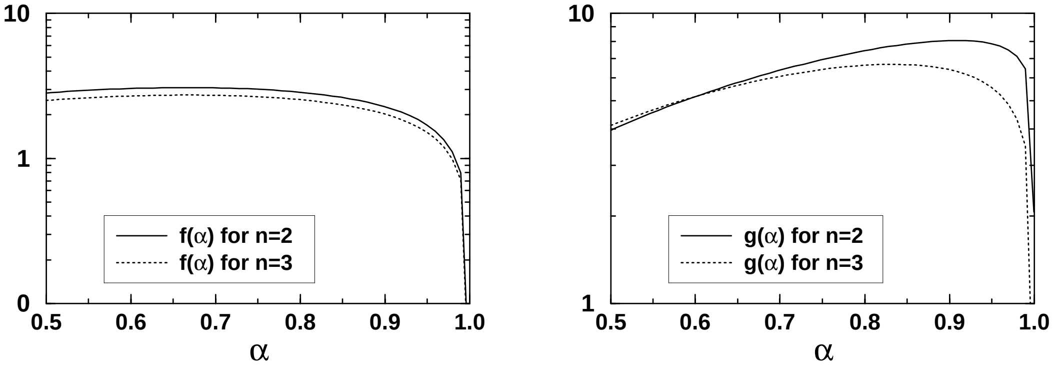

Figure 6.5 Pre-factors $\mathbf{f}(\alpha)$ and $\mathbf{g}(\alpha)$ of the compression in cylindrical ($\mathbf{n}=\mathbf{2}$) and spherical ($\mathbf{n}=\mathbf{3}$) geometry vs. the self-similarity parameter α, for $\gamma=\mathbf{5/3}$. Note that the values of α are restricted by the condition $\beta\equiv\mathbf{1}-\mu\,\lambda>\mathbf{0}$ to $0.6<\alpha<\mathbf{1}$ in cylindrical geometry, and to $0.5<\alpha<\mathbf{1}$ for spherical geometry, assuming $\gamma=\mathbf{5/3}$.

of α and can be replaced by its maximum. For $n=3$ and $\gamma=5/3$, we find $g_{\max}\simeq 3.4$ in reasonable agreement with the numerical result, cf. Fig. 6.5.

From the above derivation, it should be clear that the power formula (6.59) is only of approximate validity in an intermediate range of Mach numbers M_0. This is also visible in Fig. 6.4, where the straight-line power law (6.59) touches tangentially the somewhat curved numerical results. The curvature in the scaling of p_{s}/p_0 with M_0 reflects the transition from the scaling (6.59) valid at $x\ll 1$, to another scaling for $x\gg 1$. In this limit, the function $F(x)$ approaches the scaling $F(x)\propto x^{n-1}$, and therefore $p_{\mathrm{s}}/p_0\propto M_0^{2(\gamma+n)/(\gamma+1)}$. For $n=3$, $\gamma=5/3$, this yields an exponent of 3.5, which is slightly larger than the exponent for the limit $x=1$. Notice, however, that the fitting point $x\equiv 1-U_2=1$ chosen above is the most natural one, because it corresponds to $U_2\simeq(\kappa-2\lambda)/n\gamma=0$, and therefore to the distinguished special case in which the stagnated gas is uniform and at rest, see Eq. (6.26).

The scaling laws (6.58) and (6.59) also describe the numerical solutions in Fig. 6.4 for cylindrical ($n=2$) geometry, giving $p_{\mathrm{s}}/p_0\propto M_0^{9/4}$ and $\rho_{\mathrm{s}}/\rho_0\propto M_0^{3/4}$ for $\gamma=5/3$.

VI. Converging Flows in Plane Geometry

The case of a plane converging flow ($n=1$) is different from the cylindrical and the spherical shell implosions in that there are no effects of geometric convergence. Nevertheless, the 'shell' material is compressed between void closure and passage of the reflected shock, i.e. along the branch BOS_1, because of the self-similar flow pattern for $\alpha<1$. Like in the cylindrical or spherical geometry, one can apply the formulas (6.58) and (6.56) using the approximation $\Gamma(1-U_2)\gg 1$. This approximation is more appropriate than assumption (6.38) in the case of $n=1$, since the values of α and κ are restricted to larger values, compared to the spherical or cylindrical case; that comes from the requirement $\beta>0$. In physical terms, the latter approximation means that the shell material is assumed to be not at rest behind the reflected shock.

Under these assumptions, the compression of the shell material between void closure and passage of the reflected shock in the plane geometry is given by

$$\rho_\mathrm{s}/\rho_0 \simeq \Gamma \;, \tag{6.60}$$

while the pressure ratio is

$$\frac{p_\mathrm{s}}{p_0} \simeq \frac{2\gamma}{\gamma-1}\Gamma^{-1}M_0^2 \;. \tag{6.61}$$

Equations (6.60)–(6.61) are in good agreement with the numerical results, even including the pre-factors as one can check in Fig. 6.6.

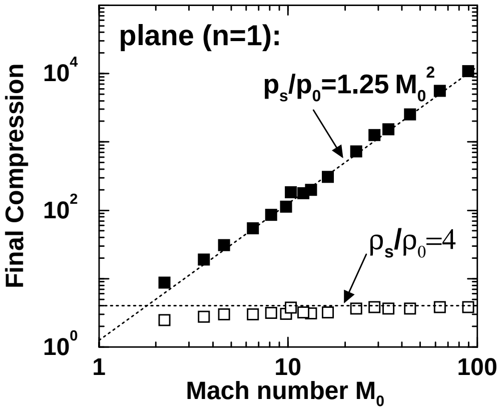

Figure 6.6 Compression ratios $\mathrm{p_s/p_0}$ and ρ_s/ρ_0 vs. Mach number $\mathrm{M_0}$ at void closure for the plane case with $\mathrm{n} = 1$. Dots represent numerical solutions of Eq. (6.20) with similarity parameters in the range $0.77 \le \alpha \le 0.95$ and $1 \le \kappa \le 5$. Lines refer to the analytical scalings (6.60) and (6.61). The scatter of the results around the power laws reflect different values of ϵ.

It seems appropriate to compare the self-similar convergent flow for $n = 1$ with the standard textbook example [51] of a shock wave which is reflected by a rigid wall in a uniform gas. This comparison, however, does not match here: the gas behind the traveling shock wave in this example case has a Mach number number

$$\hat{M}_1 = \sqrt{\frac{2}{\gamma(\gamma-1)}} \;, \tag{6.62}$$

which is determined by the adiabatic exponent γ only. Further, the ratio of the pressures behind the ingoing and the reflected shock is

$$\frac{p_3}{p_2} = \frac{3\gamma-1}{\gamma-1} \;, \tag{6.63}$$

in the limit of a strong ingoing shock wave. Mach number (6.62) and compression (6.63) do not satisfy the relation (6.61) for the self-similar flows.

Appendix A

Description of the Magneto-Hydrodynamics Code DEIRA

DEIRA is a one-dimensional (1D) magneto-hydrodynamics (MHD) code for simulating ICF targets driven by beams of fast ions, written by M. Basko [15, 55, 56]. The structure and main properties of the underlying physical model are briefly characterized in the following. For reasons of brevity, however, details about the calculation of kinetic coefficients, radiation transport, equations of state and about the numerical algorithm are omitted here; instead, the corresponding references are given. Note that cylindrical symmetry will be assumed below, although the code can also treat plane-parallel and spherical geometries.

As an overview, the main features of the DEIRA model are listed here. It includes

- Equations of 1D single-fluid two-temperature dissipative MHD with electron and ion heat conduction and physical viscosity.
- A diffusion equation for the axial component of the magnetic field.
- A diffusion equation for the energy density of radiation in single-group approximation, i.e. radiation is described by a separate radiation temperature.
- Diffusion equations for the energy densities of the various species of charged fusion products; these are alpha particles and protons for deuterium (D_2), or deuterium-tritium (DT) mixtures.
- Nuclear burn equations for the relative abundances of D, T and ^{3}He isotopes.
- A stopping equation for the propagation of fast ions from an external driver in the approximation of straight-line trajectories. The latter is used only in one case, namely in Fig. 4.3 describing the deposition characteristics of heavy ion beams in matter.

The equation of state (EOS) is given in the form of functions $P_e(V, T_e)$, $P_i(V, T_i)$, $\epsilon_e(V, T_e)$, and $\epsilon_i(V, T_i)$, where P_e, P_i and ϵ_e, ϵ_i are, respectively, the electron and the ion components of the pressure, the internal energy per unit mass, and $V \equiv 1/\rho$ is the specific volume. Additionally, it gives the ionization degree $y(V, T_e)$, where $0 < y \leq Z$

for materials with nuclear charge Z. Usually, tabulated EOS are used. The underlying physical model [57] approximates realistic properties of matter in the region of strong coupling, treats multiple ionization of atoms (both pressure and thermal), and accounts for the Fermi degeneracy of electron gases at high densities.

To solve the magneto-hydrodynamic equations numerically, an explicit finite-difference scheme with artificial viscosity is used on a Lagrangean mesh. For the solution of all diffusion equations and heat conduction terms in the MHD energy equations, a linearized implicit differencing scheme is used, in which the values of heat capacities and transport coefficients are taken from the previous time step.

A.1 Basic Equations

I. Nuclear Reactions

In target shells containing thermonuclear fuel, the following nuclear reactions are accounted for

$$\mathrm{D} + \mathrm{T} \rightarrow {}^4\mathrm{He}\ (3.52\ \mathrm{MeV}) + \mathrm{n}\ (14.07\ \mathrm{MeV})\ , \tag{A.1}$$

$$\mathrm{D} + \mathrm{D} \rightarrow {}^3\mathrm{He}\ (0.82\ \mathrm{MeV}) + \mathrm{n}\ (2.45\ \mathrm{MeV})\ , \tag{A.2}$$

$$\mathrm{D} + \mathrm{D} \rightarrow \mathrm{T}\ (1.01\ \mathrm{MeV}) + \mathrm{p}\ (3.02\ \mathrm{MeV})\ , \tag{A.3}$$

$$\mathrm{D} + {}^3\mathrm{He} \rightarrow {}^4\mathrm{He}\ (3.67\ \mathrm{MeV}) + \mathrm{p}\ (14.68\ \mathrm{MeV})\ . \tag{A.4}$$

When describing matter undergoing nuclear transformations, it is convenient to assume that it consists of identical 'molecules', with each 'molecule' containing X_k atoms (nuclei) of species k. The total number of such imaginary 'molecules' in each target shell is arbitrary: it is defined by the initial normalization of concentrations X_k. Later on, in the course of nuclear transformations of one species into another, the number of 'molecules' in each Lagrangean mass interval remains constant: only concentrations X_k change. It is convenient to introduce a 'molecular' mass A_{mol} defined as

$$A_{\mathrm{mol}} = \sum_k X_k A_k\ . \tag{A.5}$$

This quantity changes only little in the course of nuclear transformations (A.1)–(A.4), and it is assumed that

$$A_{\mathrm{mol}} = \sum_k X_{k0} A_k = \text{constant}\ , \tag{A.6}$$

where X_{k0} are the initial values of the element concentrations and A_k is the atomic mass of species k.

II. Notation

The variables used in the following equations are listed here for reference.

t	(time)	$\mathcal{E}_r, \mathcal{E}_\alpha, \ldots$	(energy density)
r	(length)	ν_{ee}, ν_{ei}	(collision frequency)
u	(velocity)	$\kappa_e, \kappa_i, \kappa_r$	(heat conduction coefficients)

$\rho = V^{-1}$	(density)	χ_{ei}, χ_{er}	(temperature relaxation coeff's)
B	(magn. induction)	$\eta_\perp$	(specific resistivity)
M, m	(mass)	$\eta_{i,sc}$, $\eta_{i,tn}$	(ion viscosity coeff's)
E	(energy)	$\chi_\alpha, \chi_{p3}, \chi_{p14}$	(fusion energy relaxation coeff's)
P_e, P_i	(pressure)	$d_\alpha, d_{p3}, d_{p14}$	(fusion energy diffusion coeff's)
ϵ_e, ϵ_i	(specific internal energy)	W_b	(beam power)
T_e, T_i, T_r	(temperature)	E_b	(fast ion energy)
q_{ik}	(nuclear reaction rate)	S_b	(stopping power)
$Q_e, Q_i, \ldots$	(specific heating rate)		

III. Differential Equations

The DEIRA code solves the basic differential equations of magneto-hydrodynamics, given here in the Lagrangean form that is used for the numerical scheme. As independent variables, time t and the reduced mass

$$m = \int_0^r \rho\, r\, dr \tag{A.7}$$

are used. The latter is related to the mass coordinate by a factor of 2π. The principal dependent variables are

$$r, \quad u, \quad T_e, \quad T_i, \quad T_r, \quad B, \quad \mathcal{E}_\alpha, \quad \mathcal{E}_{p3}, \quad \mathcal{E}_{p14}, \quad X_D, \quad X_T, \quad X_{He}, \quad X_B \ . \tag{A.8}$$

The transformation of differential operators from Eulerian to Lagrangean form is accomplished as

$$\frac{\partial}{\partial t} + u\frac{\partial}{\partial r} \rightarrow \frac{\partial}{\partial t}, \qquad \frac{\partial}{\partial r} \rightarrow \rho\, r\frac{\partial}{\partial m} \ . \tag{A.9}$$

In Lagrangean coordinates, the MHD equations take on the form

$$\frac{\partial r}{\partial t} = u \ , \tag{A.10}$$

$$\begin{aligned} \frac{\partial u}{\partial t} + r\frac{\partial}{\partial m}\Bigg[& P_{av} + P_e + P_i - \eta_{i,sc}\rho\frac{\partial}{\partial m}(ur) + \frac{B^2}{8\pi} + \frac{a_{\mathrm{SB}}T_r^4}{3} + \\ & + \frac{2}{3}\left(\mathcal{E}_\alpha + \mathcal{E}_{p3} + \mathcal{E}_{p14}\right)\Bigg] = \frac{1}{r}\frac{\partial}{\partial m}\left[\left(\eta_{av,tn} + \eta_{i,tn}\rho r^4\right)\frac{\partial}{\partial m}\left(\frac{u}{r}\right)\right] \ , \end{aligned} \tag{A.11}$$

$$\begin{aligned} & \left(\frac{\partial \epsilon_e}{\partial T_e}\right)_V \frac{\partial T_e}{\partial t} + \left[P_e + \left(\frac{\partial \epsilon_e}{\partial V}\right)_{T_e}\right]\frac{\partial\,(ur)}{\partial m} = \\ & \quad = \frac{\partial}{\partial m}\left(r\hat{\kappa}_e\frac{\partial T_e}{\partial r}\right) + \left(\frac{c}{4\pi}\right)^2 \eta_\perp V\left(\frac{\partial B}{\partial r}\right)^2 - \\ & \quad -\chi_{ei}(T_e - T_i) - \chi_{er}(T_e - T_r) + \\ & \quad +\chi_{e\alpha}\mathcal{E}_\alpha + \chi_{ep3}\mathcal{E}_{p3} + \chi_{ep14}\mathcal{E}_{p14} + Q_{\mathrm{ecl}} + Q_{\mathrm{en}} + Q_{\mathrm{dr}} \ , \end{aligned} \tag{A.12}$$

$$\left(\frac{\partial\epsilon_i}{\partial T_i}\right)_V\frac{\partial T_i}{\partial t}+\left[P_{av}+P_i+\left(\frac{\partial\epsilon_i}{\partial V}\right)_{T_i}-\eta_{i,sc}\rho\frac{\partial\,(ur)}{\partial m}\right]\frac{\partial\,(ur)}{\partial m}= \tag{A.13}$$

$$=\frac{\partial}{\partial m}\left(r\hat{\kappa}_i\frac{\partial T_i}{\partial r}\right)+\chi_{ei}(T_e-T_i)+$$

$$+\left(\eta_{av,tn}+\eta_{i,tn}\rho r^4\right)\left[\frac{\partial}{\partial m}\left(\frac{u}{r}\right)\right]^2+$$

$$+\chi_{i\alpha}\mathcal{E}_\alpha+\chi_{ip3}\mathcal{E}_{p3}+\chi_{ip14}\mathcal{E}_{p14}+Q_{icl}+Q_{in}\ ,$$

$$4a_{\mathrm{SB}}T_r^3V\frac{\partial T_r}{\partial t}+\frac{4}{3}a_{\mathrm{SB}}T_r^4\frac{\partial\,(ur)}{\partial m}=\frac{\partial}{\partial m}\left(r\hat{\kappa}_r\frac{\partial T_r}{\partial r}\right)+\chi_{er}(T_e-T_r)\ , \tag{A.14}$$

$$\frac{\partial(BV)}{\partial t}=\frac{c^2}{4\pi}\frac{\partial}{\partial m}\left(r\eta_\perp\frac{\partial B}{\partial r}\right)\ . \tag{A.15}$$

Here $\eta_{i,sc}$ and $\eta_{i,tn}$ are the coefficients of the ion (physical) viscosity, defined as

$$\eta_{i,sc}=\frac{1}{3}\eta_0^i\ ,\quad \eta_{i,tn}=\eta_1^i\ , \tag{A.16}$$

where η_0^i and η_1^i are the coefficients of the ion viscosity of the magnetized plasmas as defined by Braginskii [20]. Without magnetic field, one has simply $\eta_0^i=\eta_1^i$. Then $\hat{\kappa}_e$, $\hat{\kappa}_i$, and $\hat{\kappa}_r$ are the electron, κ_e, the ion, κ_i (both transverse with respect to the magnetic field), and radiative, κ_r, heat conduction coefficients corrected for the corresponding flux limits [56]. Transverse electrical resistivity is given by $\eta_\perp$. The quantities Q_{ecl} and Q_{icl} are the specific heating rates for plasma electrons and ions by slow charged fusion products, which deposit their energy locally. Q_{en} and Q_{in} are the corresponding heating rates by thermonuclear neutrons. The specific energy deposition by an external power source (driver) is described by Q_{dr}. The energy density of radiation is given by

$$\mathcal{E}_r=a_{\mathrm{SB}}T_r^4\ , \tag{A.17}$$

where $a_{\mathrm{SB}}=4\sigma_{\mathrm{SB}}/c=1.372\times10^{14}\,\mathrm{erg\,cm^{-3}}$ is the radiation density constant related to the Stefan-Boltzmann constant σ_{SB} [42]. Equation (A.15) for the axial magnetic field B is derived from the system of two-fluid 2-T Braginskii equations [20] with the Nernst effect being neglected.

Diffusion of the energy density $\mathcal{E}$ of fast fusion products is described by

$$V\frac{\partial\mathcal{E}_\alpha}{\partial t}+\frac{5}{3}\mathcal{E}_\alpha\frac{\partial\,(ur)}{\partial m}+\chi_\alpha\mathcal{E}_\alpha=\frac{\partial}{\partial m}\left(rd_\alpha\frac{\partial\mathcal{E}_\alpha}{\partial r}\right)+Q_\alpha\ , \tag{A.18}$$

$$V\frac{\partial\mathcal{E}_{p3}}{\partial t}+\frac{5}{3}\mathcal{E}_{p3}\frac{\partial\,(ur)}{\partial m}+\chi_{p3}\mathcal{E}_{p3}=\frac{\partial}{\partial m}\left(rd_{p3}\frac{\partial\mathcal{E}_{p3}}{\partial r}\right)+Q_{p3}\ , \tag{A.19}$$

$$V\frac{\partial\mathcal{E}_{p14}}{\partial t}+\frac{5}{3}\mathcal{E}_{p14}\frac{\partial\,(ur)}{\partial m}+\chi_{p14}\mathcal{E}_{p14}=\frac{\partial}{\partial m}\left(rd_{p14}\frac{\partial\mathcal{E}_{p14}}{\partial r}\right)+Q_{p14}\ . \tag{A.20}$$

For the calculation of the diffusion coefficients, no flux limits are imposed [56]. The depletion of thermonuclear fuel is described by the equations

$$\frac{\partial X_D}{\partial t} = \frac{1}{VA_{\mathrm{mol}}} \left(-X_D X_T\, q_{DT} - 2X_D^2\, q_{DD} - X_D X_{He}\, q_{DHe}\right) \ , \tag{A.21}$$

$$\frac{\partial X_T}{\partial t} = \frac{1}{VA_{\mathrm{mol}}} \left(-X_D X_T\, q_{DT} + \frac{1}{2} X_D^2\, q_{DD}\right) \ , \tag{A.22}$$

$$\frac{\partial X_{He}}{\partial t} = \frac{1}{VA_{\mathrm{mol}}} \left(-X_D X_{He}\, q_{DHe} + \frac{1}{2} X_D^2\, q_{DD}\right) \ . \tag{A.23}$$

Here

$$q_{ik} = \frac{\langle \sigma v \rangle_{ik}}{m_A} \tag{A.24}$$

is the rate of nuclear reaction between species i and k. The two reactions (A.2) and (A.3) are assumed to have the same rate q_{DD}.

The specific volume $V \equiv 1/\rho$ is given by

$$V = \frac{1}{2} \frac{\partial (r^2)}{\partial m}. \tag{A.25}$$

In particular, from Eqs (A.10) and (A.25) one has

$$\frac{\partial V}{\partial t} = \frac{\partial\,(ur)}{\partial m} \equiv \dot{V}. \tag{A.26}$$

The additive pressure component due to the scalar artificial viscosity is given by

$$P_{av} = -\eta_{av,sc} \frac{\partial\,(ur)}{\partial m} \equiv -\eta_{av,sc} \dot{V}. \tag{A.27}$$

Here $\eta_{av,sc} \geq 0$ and $\eta_{av,tn} \geq 0$ are, respectively, the coefficients of scalar and tensor components of the artificial viscosity [58]. In equations (A.12)–(A.20), the derivative $\dfrac{\partial}{\partial r}$ is understood as the operator $\rho r \dfrac{\partial}{\partial m}$.

IV. Energy Deposition by the Driver

The driver is defined as an external source of energy. There are two important cases relevant for the present context

(a) First the case of a uniformly heated target, as it is considered for the magnetized cylindrical implosions in Chapters 4–5. Here one takes

$$Q_{\mathrm{dr}} \equiv P_{\mathrm{i}}(r,t) = \begin{cases} \mathrm{const}\ , & R_{\mathrm{p}} < r < R_{\mathrm{b}}\ , \\ 0\ , & \text{otherwise.} \end{cases} \tag{A.28}$$

Here R_{p} and R_{b} are fixed values, given e.g. in Fig. 4.1.

(b) The second case refers to a situation where the beam of fast ions propagates normally with respect to a planar surface. This situation is considered in Fig. 4.3 checking the characteristics of energy deposition of an ion beam in matter. In Eulerian coordinates, the energy of individual ions $E_b(t, r)$ is determined by solving the equation of beam propagation

$$\frac{\partial E_b}{\partial r} = \rho S_b(E_b, \rho, T_e, T_i) \tag{A.29}$$

with the boundary condition $E_b(t, R) = E_{b0}$; here R is the outer target radius, $S_b = S_b(E_b, \rho, T_e, T_i)$ is the stopping power of matter, which is a known function of its arguments [59]. In the present model, the driver energy is assumed to be transferred exclusively to the electron component of the plasma. The specific heating rate in Eq. (A.12) is

$$Q_{\mathrm{dr}}(t, r) = W_b(t)\, \frac{S_b(E_b, \rho, T_e, T_i)}{E_{b0}} \ , \tag{A.30}$$

where $W_b(t)$ is the total beam power.

V. Thermonuclear Burn Rates

The Maxwell-averaged fusion reaction rates $\langle \sigma v \rangle_{ik}$ depend only on the fuel ion temperature T_i. They are related to the corresponding q_{ik} via

$$\langle \sigma v \rangle_{ik}\ (\mathrm{cm}^3\ \mathrm{s}^{-1})\ = 1.66 \times 10^{-16}\, q_{ik}\ , \tag{A.31}$$

where the q_{ik} are given in units of $10^8 \mathrm{cm}^3\, \mathrm{g}^{-1}\ \mathrm{sec}^{-1}$. For the burn rate of DT reactions, the following approximate formula [60] is used

$$\begin{aligned} q_{DT} = 1.58 \times 10^4\, T_i^{-2/3} \Bigg\{ (1 + 0.16\, T_i)\ \exp\left[-\frac{19.98}{T_i^{1/3}} - \left(\frac{T_i}{10.34} \right)^2 \right] + \\ +0.0108\ \exp\left(-\frac{45.07}{T_i} \right) \Bigg\} \ . \end{aligned} \tag{A.32}$$

Burn rates of other nuclear reactions can be found in Ref. [56]. Temperatures T_i are given in units of keV. The formula (A.32) is used for the thermal power balance in Chapter 2. The specific heating rate of thermonuclear energy sources is then given by

$$\begin{aligned} Q_{\mathrm{fus}} = \frac{\rho}{A_{\mathrm{mol}}^2} \Big(1.70 \times 10^5\, X_D\, X_T\, q_{DT} + 7.04 \times 10^4\, \frac{1}{2}\, X_D^2\, q_{DD} + \\ +1.77 \times 10^5\, X_D\, X_{He}\, q_{DHe} \Big)\ \left(10^{22}\, \mathrm{erg}\, \mathrm{g}^{-1}\ \mathrm{sec}^{-1}\right) \ . \end{aligned} \tag{A.33}$$

A.2 Boundary Conditions

At $r = 0$, the boundary conditions for a fixed center of symmetry are used; as a consequence, all diffusion fluxes are zero

$$u(t,0) = 0 \ , \tag{A.34}$$

$$\frac{\partial T_e}{\partial r} = \frac{\partial T_i}{\partial r} = \frac{\partial T_r}{\partial r} = \frac{\partial B}{\partial r} = 0 \ , \tag{A.35}$$

$$\frac{\partial \mathcal{E}_\alpha}{\partial r} = \frac{\partial \mathcal{E}_{p3}}{\partial r} = \frac{\partial \mathcal{E}_{p14}}{\partial r} = 0 \ . \tag{A.36}$$

The conditions at the outer boundary, $r = R$, are

$$\frac{\partial T_e}{\partial r} = 0 \ , \quad \kappa_r \frac{\partial T_r}{\partial r} = \frac{1}{4} c \, a_{\mathrm{SB}} \left(T_{r\mathrm{ex}}^4 - T_r^4 \right) \ , \tag{A.37}$$

$$P(t,R) = P_{\mathrm{b}}(t) + \frac{1}{3} a_{\mathrm{SB}} T_{r\mathrm{ex}}^4 + \frac{B_{\mathrm{b}}^2}{8\pi} \ , \tag{A.38}$$

$$B(t,R) = B_{\mathrm{b}}(t) \ , \tag{A.39}$$

$$\mathcal{E}_\alpha(t,R+0) = \mathcal{E}_{p3}(t,R+0) = \mathcal{E}_{p14}(t,R+0) = 0 \ . \tag{A.40}$$

Here, boundary pressure $P_{\mathrm{b}}(t)$, boundary magnetic field $B_{\mathrm{b}}(t)$, and boundary radiation temperature $T_{r\mathrm{ex}}(t)$ are assumed to be given. The values used throughout the present work are $P_b = 0$, $T_{r\mathrm{ex}} = 0$, $B_b = B_0 \equiv B(0,r)$.

A.3 Kinetic Coefficients and Radiation Energy Transport

The following kinetic coefficients are contained in Eqs (A.10)–(A.20) of magnetohydrodynamics, radiation diffusion, and energy diffusion of fast fusion products. The coefficients of transverse (with respect to the magnetic field) heat conduction and temperature relaxation κ_e, κ_i, κ_r, χ_{ei}, χ_{er}; ion (physical) viscosity coefficients η_0^i and η_1^i; the transverse electrical conductivity coefficient $\eta_\perp$; the coefficients of diffusion and relaxation of the energy of fast fusion products d_α, d_{p3}, d_{p14}, $\chi_\alpha = \chi_{e\alpha} + \chi_{i\alpha}$, $\chi_{p3} = \chi_{ep3} + \chi_{ip3}$, $\chi_{p14} = \chi_{ep14} + \chi_{ip14}$. The formulae for these coefficients are based on the expressions published earlier in Refs [20,32,61–64].

The present radiation transport model is based on the approximation of a single-frequency group or, in other words, a separate radiation temperature. It describes radiation-matter interaction by taking into account the processes of Compton scattering, free-free absorption, free-bound / bound-bound absorption. The free-free absorption (inverse bremsstrahlung) coefficient is calculated for a partially degenerate Fermi gas of free electrons. The contribution of the bound-bound and bound-free transitions is evaluated on the basis of the model proposed in Ref. [63].

Bibliography

[1] N. Angert, *High intensity developments at GSI*, Nucl. Instrum. Methods Phys. Res. **A 415**, 236 (1998).

[2] I. Hofmann, *Heavy ion inertial fusion in Europe; paper presented at the 13th Int. Symp. on Heavy Ion Inertial Fusion, March 2000, San Diego, USA*, Nucl. Instrum. Methods Phys. Res. (2001).

[3] B. Sharkov, G. Koshkarev, M. Churazov, N. Alexeev, M. Basko, A. Golubev and P. Zenkevich, *Heavy-ion fusion activities at ITEP*, Nucl. Instrum. Methods Phys. Res. **A 415**, 20 (1998).

[4] I. Lindemuth et al., *Target plasma formation for magnetic compression/ magnetized target fusion*, Physical Review Letters **75**(10), 1953 (1995).

[5] J. Linhart and L. Bilbao, *Z pinch spark of an axial detonation in DT*, Nucl. Fusion **40**(5), 941 (2000).

[6] N. Tahir, D. Hoffmann, J. Maruhn, K.-J. Lutz and R. Bock, *Numerical simulations and theoretical analysis of proposed heavy-ion-matter experiments at the GSI accelerator facility*, Physics of Plasmas **5**(12), 4426 (1998).

[7] N. Tahir et al., Physical Review E **61**, 1975 (2000).

[8] M. Basko, A. Kemp and J. Meyer-ter-Vehn, *Ignition Conditions for Magnetized Target Fusion in Cylindrical Geometry*, Nucl. Fusion **40**, 59 (2000).

[9] J. Lindl, *Inertial Confinement Fusion: The Quest for Ignition and Energy Gain Using Indirect Drive*, Springer Verlag, New York (1998).

[10] R. Ramis, J. Honrubia, J.Ramirez and J. Meyer-ter-Vehn, *Hohlraum targets for HIDIF*, in: C. Labaune, W. Hogan and K. Tanaka (Eds), *Inertial Fusion Sciences and Applications - State of the Art 1999*, p. 509, Elsevier, Paris (2000).

[11] A. Kemp, M. Basko and J. Meyer-ter-Vehn, *Ignition conditions for magnetically insulated tamped ICF targets in cylindrical geometry*, Nucl. Fusion **41**(2), 235 (2001).

[12] K. Miyamoto, *Plasma Physics for Nuclear Fusion*, MIT Press (1980).

[13] E. Avrorin et al., *Numerical calculations on fusion detonation in a dense plasma*, Sov. J. Plasma Phys. **10**(3), 298 (1984).

[14] A. Caruso and C. Strangio, *The injected entropy approach for the ignition and high gain targets by heavy ion beams or incoherent x-ray pulses*, in: C. Labaune, W. Hogan and K. Tanaka (Eds), *Inertial Fusion Sciences and Applications*, p. 88, Elsevier, Paris (1999).

[15] M. Basko, *Magnetized implosions driven by intense ion beams*, Physics of Plasmas **7**, 4579 (2000).

[16] J. Meyer-ter-Vehn and C. Schalk, *Selfsimilar spherical compression waves in gas dynamics*, Z. Naturforsch. **37a**, 955 (1982).

[17] M. Herrmann, M. Tabak and J. Lindl, *A generalized scaling law for the ignition energy of inertial confinement fusion capsules*, Nucl. Fusion **41**(1) (2001).

[18] S. Atzeni and J. Meyer-ter-Vehn, *Comments on the article 'A generalized scaling law for the ignition energy of inertial confinement fusion capsules by M.C. Herrmann, M. Tabak, J.D. Lindl, Nucl. Fusion* **41** *(2001) 99*, Nucl. Fusion **41**(4), 465 (2001).

[19] A. Kemp, J. Meyer-ter-Vehn and S. Atzeni, *Stagnation pressure of imploding shells and ignition energy scaling of ICF targets*, Physical Review Letters **86**(15), 3336 (2001).

[20] S. Braginskii, *Transport Processes in a Plasma*, Reviews of Plasma Physics **1** (1965).

[21] S. Gus'kov, V. Rozanov and L. Trebuleva, *Energy Transfer by Alpha Particles in a Laser Plasma subjected to a Magnetic Field*, Sov.J.Quantum Electronics **14**(8), 1062 (1984).

[22] O. Krokhin and V. Rozanov, Sov.J.Quantum Electronics **2**, 393 (1973).

[23] R. Jones and W. Mead, *The physics of burn in magnetized deuterium-tritium plasmas*, Nucl. Fusion **26**(2), 127 (1986).

[24] J. Lindl, *Physics of Ignition for ICF Capsules*, in: A. Caruso and E. Sindoni (Eds), *Int. School of Plasma Physics Piero Caldirola: Inertial Confinement Fusion*, p. 617 (1988).

[25] R. Kirkpatrick, I. Lindemuth and M. Ward, *Magnetized Target Fusion: An Overview*, Fusion Technology **27**, 201 (1995).

[26] D. Kilcrease and R. Kirkpatrick, *Magnetized Fuel Inertial Confinement Fusion*, Nucl. Fusion **28**(8), 1465 (1988).

[27] M. Sweeney and A. Farnsworth Jr., Nucl. Fusion **21**, 41 (1981).

[28] I. Lindemuth and R. Kirkpatrick, *Parameter Space for Magnetized Fuel Targets in Inertial Confinement Fusion*, Nucl. Fusion **23**(3), 263 (1983).

[29] S. Atzeni, Jpn. J. Appl. Phys. **34**, 1980 (1995).

[30] J. Meyer-ter-Vehn, *On Energy Gain of Fusion Targets: The Model of Kidder and Bodner Improved*, Nucl. Fusion **22**(4), 561 (1982).

[31] M. Basko, Sov. J. Plasma Phys. **13**, 558 (1987).

[32] M. Liberman and A. Velikovich, *Distribution Function and Diffusion of α-particles in DT Fusion Plasma*, J. Plasma Physics **31**, 369 (1984).

[33] A. Oparin, S. Anisimov and J. Meyer-ter-Vehn, *Kinetic Simulations of DT Ignition and Burn in ICF Targets*, Nucl. Fusion **36**(4), 443 (1996).

[34] M. Basko, Nucl. Fusion **30**, 2443 (1990).

[35] R. Arnold and J. Meyer-ter-Vehn, *Heating matter with heavy ion beams*, Z. Phys. D **9**, 65 (1988).

[36] T. Mehlhorn, J. Appl. Phy. **52**, 1856 (1981).

[37] C. Scheidenberger et al., Physical Review Letters **77**(19), 3987 (1996).

[38] J. Jacoby et al., Physical Review Letters **74**(9), 1550 (1995).

[39] M. Roth et al., Europhysics Letters **50**, 28 (2000).

[40] U. Neuner et al., *Shaping of intense ion beams into hollow cylindrical form*, Physical Review Letters **85**(21), 4518 (2000).

[41] L. Landau and E.M.Lifschitz, *Electrodynamics of Continuous Media (Vol. 8 of course of theoretical physics) 2nd revised edition*, Pergamon Press, New York (1987).

[42] D. Book, *NRL Plasma Formulary*, Washington, DC (1990).

[43] V. Velikovich, S. Gol'berg, M. Liberman and F. Felber, *Hydrodynamics of compression of a plasma with frozen-in magnetic field by a thin cylindrical wall*, Sov. Phys. JETP **61**(2), 261 (1985).

[44] M. Rosenbluth, *Infinite conductivity theory of the pinch*, Los Alamos Report LA-1850 (1955).

[45] H. Kull, *Theory of the Rayleigh-Taylor instability*, Physics Reports **206**, 199 (1991).

[46] `www-aix.gsi.de/~hidif`.

[47] Y. Bakhrameev, V. Mokhov and N. Popov, *Criterion for ignition and reserve at ignition for thermonuclear targets*, Atomnaya Energiya **49**(2), 121 (1979).

[48] M. Basko, *Inertial Confinement Fusion with Magnetized Fuel in Cylindrical Targets*, CEA Report EUR-CEA-FC-1645 (1998).

[49] M. Basko, *private communication* (Feb. 2001).

[50] Y. Saillard, *private communication* (Feb. 2001).

[51] L. Landau and E.M.Lifschitz, *Fluid Mechanics (Vol. 6 of course of theoretical physics) 2nd revised edition*, Pergamon Press, New York (1987).

[52] Y. Zel'dovich and Y. Raizer, *Physics of Shock Waves and High-Temperature Hydrodynamic Phenomena*, Academic Press, New York (1966).

[53] S. Coggeshall and J. Meyer-ter-Vehn, *Group-invariant solutions and optimal systems for multidimensional hydrodynamics*, Journal of Mathematical Physics **33**(10), 3585 (1992).

[54] G. Guderley, Luftfahrtforschung **19**, 302 (1942).

[55] M. Basko, *Spark and volume ignition of DT and D_2 microspheres*, Nucl. Fusion **30**(12), 2443 (1990).

[56] M. Basko, *DEIRA – A 1-D 3-T Hydrodynamic code for simulating icf targets driven by fast ion beams*, tech. rep., Institute for Theoretical and Experimental Physics, Moscow (2001).

[57] M. Basko, *Metallic Equation of State in the Mean Ion Approximation*, High Temperature **23**(3), 388 (1985).

[58] M. Basko, *Spark and volume ignition of DT and D_2 microspheres*, Nucl. Fusion **30**(12), 2443 (1990).

[59] M. Basko, Sov. J. Plasma Phys. **10**, 689 (1984).

[60] W. Fowler, G. Caughlam and B. Zimmerman, Ann. Rev. Astron. Ap. **13**, 69 (1975).

[61] M. Basko, *Equations of one-dimensional radiative hydrodynamics with heat conduction and kinetics of thermonuclear burn (in Russian)*, Preprint ITEP-145, Inst. of Theor. Exp. Physics, Moscow (1985).

[62] M. Basko, Sov. J. Plasma Phys. **13**, 558 (1987).

[63] V. Imshenik, I. Mikhailov, M. Basko and S. Molodtsov, Sov. Phys. — JETP **63**, 980 (1986).

[64] N. Bobrova and P.V.Sasorov, *MHD equations for a fully ionized plasma of complex composition*, Plasma Phys. Rep. **19**(6), 409 (1993).

[65] C. Cereceda, C. Deutsch, M. De Peretti, M. Sabatier, M. Basko, A. Kemp and J. Meyer-ter-Vehn, Physics of Plasmas **7**(11), 4515 (2000).

Conclusions

The aim of the present thesis has been to examine the concept of axially magnetized, cylindrical implosions driven by heavy ion beams. In particular, the intention has been to study the generation of high energy density in matter for fundamental research and to explore the potential for inertial confinement fusion. Results have been obtained by means of one-dimensional (1D) magneto-hydrodynamic (MHD) computer simulations [15], and by simple analytic modeling. In the following, the main conclusions are listed by the order of their appearance in the text.

(1) The thermal power balance of magnetized cylindrical DT fuel volumes at stagnation has been analyzed. The results help to understand the effect of magnetic insulation in fusion targets at stagnation. The results have appeared in *Nuclear Fusion* [8,65].

(2) Due to the slow fuel burn in magnetized cylindrical fusion targets, which is caused by the lower volume compression as compared to spherical implosions, the fuel has to be confined by a heavy tamper layer. An important result of this work is that the ignition threshold of tamped, magnetically insulated fuel volumes depends on the equation of state of the tamper material. Corresponding results have appeared in *Nuclear Fusion* [11].

(3) A problem of magnetized cylindrical implosions is the diffusive loss of magnetic flux out of the fuel volume, followed by an accumulation of fuel material next to the imploding pusher. The formation of this boundary layer has been investigated by means of 1D-MHD computer simulations.

(4) Ignition conditions for magnetized fusion targets, in terms of the driver pulse energy, have been discussed. The important new result is that magnetized targets ignite at significantly reduced implosion velocities and fuel ρR values, compared to spherical ICF targets. This leads to relaxed conditions on the power and the pulse duration of the driver. Hot-spot ignition, i.e. the propagation of a burn wave along the axis, is essential for high fusion energy gain in the cylindrical targets.

(5) The stagnation pressure in converging flows has been analyzed by means of a similarity solution for the equations of ideal gas-dynamics (for spherical, cylindrical or plane flow patterns). Analytical scaling relations, relevant for an ignition energy scaling of ICF targets and for a general understanding of the shell implosions discussed here, have been derived. These results have appeared in *Physical Review Letters* [19].

Acknowledgements

The present work has been worked out under the guidance of Prof. Dr. J.Meyer-ter-Vehn at the Max-Planck-Institut für Quantenoptik (Garching), in loose cooperation with M. Basko from the Institute for Theoretical and Experimental Physics (Moscow). The author is indebted to M. Basko for putting the simulation code DEIRA at his disposal, and for a number of instructive discussions about the code and the subject of this work.

Special thanks to the theory group at MPQ, Matthias Dreher, Dr. Sergej Gordienko, Angelika Hofmann, Dr. Mitsuro Honda, Malte Kaluza, Andreas Krug, Lukas Kurtz, Dr. Roland Lichters, Dr. Robert Pfund, Prof. Alexander Pukhov, Dr. Andreas Saemann, Dr. Theodor Schlegel, Dr. Jens Schneider, Dr. Christoph Skornia and Dr. Zheng-Ming Sheng. Thanks also to Manfred Grote and Dr. Reinhard Volk for their help with computer soft- and hardware problems and to the always cheerful Renate Weise-McKnight. Special thanks also to my family for their personal support during the last three years.

Curriculum Vitae

Name: Andreas Johannes Kemp

Date of birth: 19.04.1971

Place of birth: Bonn

Marital Status: Single

1981–1990	Aloisiuskolleg, Bonn-Bad Godesberg
1990–1991	Military service
1991–1994	Physics studies at the Rheinische Friedrich-Wilhelms-Universität Bonn
1993	Vordiplom
1994–1995	University of Edinburgh, GB
1995–1997	Technische Universität München
1996–1997	Diploma thesis ’eine Zustandsgleichung heißer, dichter Materie’ at Max-Planck-Institut für Quantenoptik
1998	Diplom (mit Auszeichnung)
since 1998	PhD. studies at the Max-Planck-Institut für Quantenoptik under the guidance of Prof. Dr. J. Meyer-ter-Vehn